AGRICULTURAL RESIDUES AND OTHER CARBON-BASED RESOURCES AS FEEDSTOCKS FOR SUPERCAPACITOR ELECTRODES

A Dissertation
Submitted to the Graduate Faculty
of the
North Dakota State University
of Agriculture and Applied Science

By

Yong Wang

In Partial Fulfillment of the Requirements
for the Degree of
DOCTOR OF PHILOSOPHY

Major Program:
Materials and Nanotechnology

June 2017

Fargo, North Dakota

North Dakota State University
Graduate School

Title

AGRICULTURAL RESIDUES AND OTHER CARBON-BASED RESOURCES AS FEEDSTOCKS FOR SUPERCAPACITOR ELECTRODES

By

Yong Wang

The Supervisory Committee certifies that this ***disquisition*** complies with North Dakota State University's regulations and meets the accepted standards for the degree of

DOCTOR OF PHILOSOPHY

SUPERVISORY COMMITTEE:

Long Jiang
Chair

Xiangfa Wu

Erik Hobbie

Dennis Wiesenborn

Approved:

1/30/2018	Erik Hobbie
Date	Department Chair

ABSTRACT

Agricultural residues are generally considered as renewable, economical and environmental-friendly sources to produce carbon-based nanomaterials with many advanced applications. Agricultural residues and by-products generated from the agricultural industry, such as distiller's dried grains with solubles (DDGS), are produced every year on a large scale but lack of proper utilization. As a result, seeking high-value applications based on agricultural residues is essential for the promotion of the economy in agricultural producing states like North Dakota, USA.

With the fast development of nanotechnology in recent years, carbon-based nanomaterials have attracted intense research interests in the fields of chemistry, materials science and condensed matter physics due to many unique properties (e.g., chemical and thermal stability, electrical conductivity, mechanical strength, etc.). The development of low-cost nanomaterials using agricultural residues as feedstocks can be a promising route for the sustainable development of the agricultural industry.

In this dissertation, the preparation of carbon-based materials from agricultural residues is explored. Many advanced applications are investigated, especially in the field of energy storage devices. The development of porous activate carbons were investigated in detail, and their application as electrode materials of supercapacitors was demonstrated. Hydrothermal carbonization of biomass to produce carbonaceous materials was also covered in this dissertation. In addition to traditional raw materials such as cellulose produced from wood industry, novel material sources such as bacterial cellulose were used to prepare nanocomposites that can be used for the electrodes of supercapacitors. This dissertation contributes to the sustainable development of the agricultural industry in North Dakota.

ACKNOWLEDGEMENTS

I would like to thank Dr. Long Jiang for offering me the precious opportunity to come to NDSU, participate in his research projects and pursue my PhD degree. His help all these years plays the most important role for the completion of my study. I also want to thank my committee members, Dr. Erik Hobbie, Dr. Xiangfa Wu and Dr. Dennis Wiesenborn, for their time and energy spent on reviewing my research projects and my dissertation. Additionally, I would like to acknowledge all members in Dr. Jiang's research group, the faculties and staffs in the department of Mechanical Engineering and the program of Materials and Nanotechnology of NDSU. Without their help, the completion of this work would be impossible.

I would also like to express my gratitude towards my family and friends who encouraged me along the way.

DEDICATION

This dissertation is dedicated to Link, Zelda, Mario, and my wife Donghui Wang.

TABLE OF CONTENTS

LIST OF TABLES

LIST OF FIGURES

LIST OF ABBREVIATIONS

AC(s)	Activated Carbon(s)
DDGS	Distiller's dried grains with solubles
SC(s)	Supercapacitor(s)
CNP	Carbon Nanoparticle
PANI	Polyaniline
MB	Methylene blue
EDLC	Electric double-layer capacitor
SEM	Scanning electron microscope
TEM	Transmission electron microscopy
CV	Cyclic Voltammetry
CCD	Cyclic Charge-Discharge
EIS	Electrochemical impedance spectroscopy
PPy	Polypyrrole
PVA	Poly (vinyl alcohol)
XRD	X-ray diffractometer
PEDOT	Poly(3,4-ethylenedioxythiophene)
ESR	Equivalent series resistance (Ω)
FTIR	Fourier transforms infrared spectroscopy
UV-Vis	Ultraviolet-visible

LIST OF SYMBOLS

H_2SO_4	Sulfuric acid
H_3PO_4	Phosphoric acid
Hz	Hertz
MnO_2	Manganese dioxide
C_s	Specific capacitance (F/g)
℃	Celsius degree

1. INTRODUCTION: THE HISTORY AND DEVELOPMENT OF RENEWABLE ENERGY AND ENERGY STORAGE DEVICES

1.1. Background

It is a truth universally acknowledged that energy is related to every respect of human activities. Energy powers the very operation of modern society. The power outage happened on August 14, 2003 in the Northeastern and Midwestern United States and the Canadian province of Ontario, which lasted for 31 hours, affected 31 million people and costed 4~6 billion US dollars in total, demonstrated how crucial the energy supply was to the modern society.[1] To secure the continuing demand for extensive and stable energy supply, reliable and economical energy sources are indispensable. With the fast progresses in science and technology, the modern society also calls for other requirements for its energy sources, e.g. environmental friendliness and sustainability. It can be observed in history that the innovation and development of most revolutionary technologies were associated with the discovery and application of reliable energy sources in nature. The First Industrial Revolution occurred in the 18th century was based on the application of coal as the energy source for steam engines,[2] while the Second Industrial Revolution was energized by the development of petroleum and electricity as the major energy source.[3] Since the two Industrial Revolutions, humankind has successfully exploited the fossil fuels, such as coal, petroleum and natural gas, to provide high-quality energy for large-scale industrial production which leads to prosperity.[4] These energy sources based on fossil fuels could provide energy orders of magnitude larger than human muscles, animal power, watermills and windmills that were typically used before the Industrial Revolution.

Energy sources can be divided into two categories, i.e. primary sources and secondary sources. Primary sources of energy are the sources that can be found in nature. They can exist in form of non-renewable and renewable. Primary sources of energy can be used directly. Coal, for example, is a non-renewable primary energy source that has been used for thousands of years for heating and cooking.[5] On the contrary, wind energy is a renewable primary energy source that also has a long history, but its application was reheated decades ago due to arising environmental concerns.[6] Primary energy source can also be used to generate secondary energy source (also known as energy carriers), i.e. the energy source that are transformed from primary energy sources. Electricity is an example of secondary energy source. It can be easily transported over the power grid and can be used to provide energy for electric cars, electronic devices, residences, as well as manufacturing plants.

At the beginning stage of the industrialization, the fossil fuels seemed to be ideal energy sources. They are large in quantity, cost-effective and high in energy density, which make them meet all the standards for reliable energy sources. The continuous development of combustion technologies increases the efficiency of internal combustion engines and reduces the cost of using fossil fuels as main energy source. As of today, the global market of crude oil has been established for centuries and has shaped the lifestyle of all peoples across the world. It is estimated that fossil fuels will remain the major energy source in the foreseeable future, and will still provide around 84% of the total energy supply by 2030.[7] Besides, technological improvements make other sources of fossil fuels such as oil shale and methane hydrates commercially viable, which makes fossil fuels to be even more competitive.[8] Overall, the path dependence effect makes it hard to shrink the large share in energy source market that crude oil and other fossil fuels have already occupied (Figure 1.1).

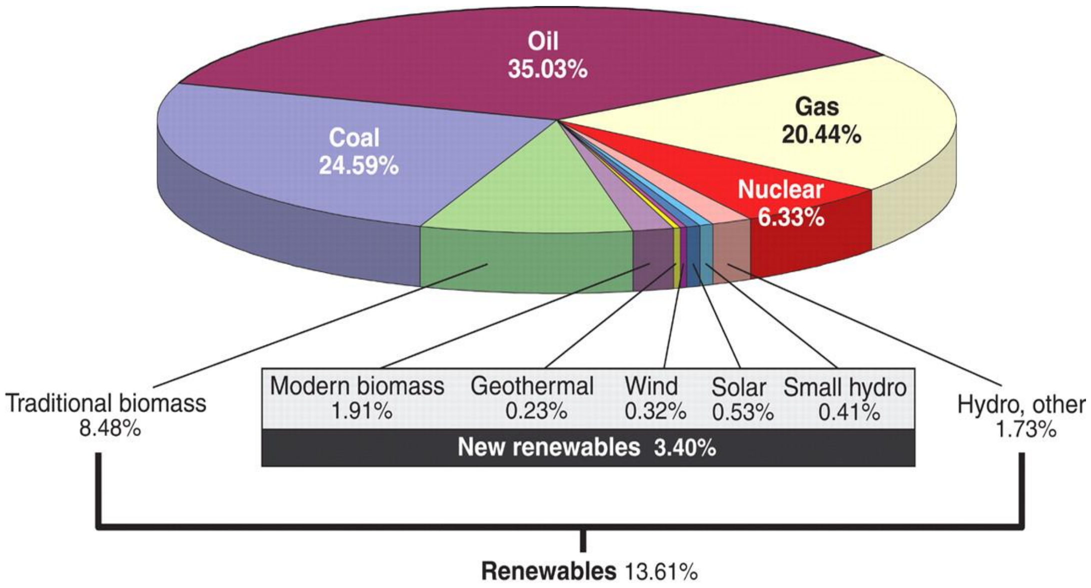

Figure 1.1. World total primary energy supply in 2004.[9]

However, despite the large share the fossil fuels currently hold, the traditional sources based on fossil fuels face condemnation for causing global warming, ocean acidification, and environment pollution.[10] The global average temperature, due to the increase of greenhouse gases, could be increased by 4 ℃ or more by the year 2100.[11] The wide use of fossil fuels is the main contributor to the emission of carbon dioxide, which is one of the gases that contributes to the greenhouse effect.[12] According to the data published by the international energy agency (IEA), nearly 62% of the carbon dioxide emission was contributed by the combustion of fossil fuels in 2010.[13] Although some other studies show different numbers, all studies agree that fossil fuel is the most significant source of carbon dioxide emission, and it is believed to be the main reason for global warming and climate change.[14, 15]

The finite supply of fossil fuels also restricts their application in the future. According to the calculations from the from the Klass model, the depletion for crude oil, coal and natural gas will happen in around 35, 107 and 37 years, respectively.[7] As the most important raw material for industry, crude oil will be depleted earlier than the other types of fossil fuels, which makes the searching for substitute energy sources even more urgent. To achieve sustainable development and to protect the environment, new energy sources are demanded to replace fossil fuels. A global transition to renewable energies is currently underway, and the policies enforced by the governments will be likely to change the trajectory of the development of the energy market.[16]

Considering many factors such as technology developments, population growth and political policies aiming at reducing the emission of greenhouse gases, it is estimated that the demand for energy will continue to increase until around 2025.[17] The continuing growth of population and economy demands larger energy supply; however, both the limited reserve of fossil fuels and environmental concerns restrict their application in the future. The renewable energy sources are alternative sources of energy that are promising to replace the current role of fossil fuels. Based on the fast development of many new technologies that can utilize many sustainable energy sources such as wind, biomass, solar, etc., the percentage of renewable energies has grown significantly in the past decades. It should be noted that although the share of renewable energy is rapidly growing, they have some drawbacks that restrict their applications on the energy supply market. Because of the intrinsic disadvantages of the renewable energies such as relatively high cost, intermittency, low conversion efficiency and low energy output, fossil fuels will still be the majority sources of energy until revolutionary technology development in this area happens.[18] To overcome the above issues and to facilitate the penetration of renewable energy sources, the adoption of energy storage systems and energy storage devices is essential and must be emphasized.[19, 20] In this chapter, the development of renewable energy sources will be reviewed, and the roles of energy storage devices such as supercapacitors for the application of renewable energy sources will be discussed.

1.2. Renewable energy sources and their application

As more and more devastating effects of global warming and the correlation between global warming and the use of fossil fuels unveiled, the transition towards sustainable and renewable energy sources is inevitable. The feasibility of using renewable energy sources to meet most of energy demand has been theoretically demonstrated decades ago, and many researchers are working on the scenario of 100% renewable energy supply by the year 2050.[21] Renewable energy sources such as solar, wind, geothermal energy and biomass, draw much attention in recent years and their percentage in overall energy supply are gradually increasing. Renewable energy sources barely generate neither air pollution nor emissions of carbon dioxide, so they are considered as clean sources of energy with low environmental impacts.[22] The renewable energy sources currently account for ~20% of the total world energy demand, and the percentage is expected to be increased to 47.7% by 2040 (Table 1.1).[22]

Table 1.1. Global renewable energy scenario by 2040[23]

	2001	**2010**	**2020**	**2030**	**2040**
Total consumption (million tons oil equivalent)	10038	10549	11425	12352	13310
Biomass	1080	1313	1791	2483	3271
Large hydro	22.7	266	309	341	358
Geothermal	43.2	86	186	333	493
Small hydro	9.5	19	49	106	189
Wind	4.7	44	266	542	688
Solar thermal	4.1	15	66	244	480
Photovoltaic	0.1	2	24	221	784
Solar thermal electricity	0.1	0.4	3	16	68
Marine (tidal/wave/ocean)	0.05	0.1	0.4	3	20
Total renewable energy source	1365.5	1745.5	2964.4	4289	6351
Renewable energy source contribution (%)	13.6	16.6	23.6	34.7	47.7

However, the renewable energy sources show different dynamic characteristics than the fossil fuel-based energy sources, and several obstacles of the renewables need to be addressed so that the renewable energy can be served as the major power source. For example, the power plants using the renewable energy sources usually provide less power than the power plants using the traditional energy sources. A typical biomass plant usually offers a 50 MW capacity, which is only one tenth of a middle-sized fossil-fuel power plant.[24] The largest wind turbine can only provide 2~5 MW of electricity, while a mid-size coal plant can produce hundreds of MW of electricity.[25] The low capacity indicates that to collect enough power, several power generators using renewable energy sources need to be connected to form a large energy farm. The large amount of connected power generators, however, introduces technical complexities such as power management, load balancing and phase synchronization, which are necessary to make the voltage phase, frequency, and amplitude of the electricity stable and usable. Besides, the renewable energy sources are usually intermittent. Photovoltaic cells can only produce energy when sunlight shines, and wind turbines can work only with strong wind present. The randomness and volatility of intermittent power supplies require complex grid optimization as well as backup power systems to function properly.

Energy storage device is the key to support the desired scenario of providing energy solely by the renewable energy sources.[26] To ensure the reliability, stability and quality of the output level, backup power supply is necessary. Energy storage systems can be used to supply power when the output level of the renewable energies is low, thus mitigate the intermittency of renewable energies.[27] Although the power plants using the renewable energy sources are relatively small in size and cannot provide sufficient energy for a vast geographical area, they are suitable for small size power grids that are isolated from the large power grid. By reducing the size of the power grid, the difficulties of control and management of a centralized large power grid can be partially resolved as well. Besides, energy storage systems also make off-grid energy supply for areas with limited infrastructure possible. Furthermore, the fast development of portable electronics and electric cars calls for the miniaturization of energy storage devices that are nonetheless capable of providing high energy density and power density. For those aforementioned reasons, energy storage systems based on energy storage devices with high energy and power density will facilitate the future integration of renewable energy sources into the existing power system. The concept of smart grid systems that consist of power generators using renewable energy sources, energy storage system with energy storage devices, and power management module with automatic control, are being developed and will be the core concept for next generation power system.[28, 29]

1.3. Energy storage devices

The importance of the energy storage devices has been justified in many respects of modern society. For example, the transportation industry contributes significantly to the increase of oil consumption and the carbon dioxide emissions, but according to a recent report published by the IEA, a dramatic change of energy source must be implemented in the transportation industry.[30] As a result, many automotive manufacturers are shifting their emphasis onto hybrid electric vehicles and pure electric vehicles with novel energy storage systems built in.[31] The bottleneck for the development of electric vehicles, however, is the energy storage device which powers the vehicles instead of gasoline. Similarly, the fast development of portable electronic devices such as laptops and smartphones with high-performance and large size displays also calls for high capacity energy storage devices. Unfortunately, the improvements of the energy storage devices have not been kept pace with the improvements of the other components of these electronics.[32] Last but not least, energy storage technologies are crucial for integration and deployment of renewable energy systems. Continuing innovation of reliable and low-cost energy storage devices are needed to facilitate the application of renewable and sustainable energies sources.

Many quantitative metrics are used to compare the performance of different kinds of energy storage devices. In scientific language, energy is defined as the ability to perform work, which is measured in joules (J) or calories (cal). Power is defined as the rate at which energy is produced, transported or consumed. It is measured in watt (W), which represents the amount of energy used, transported or produced in unit time (1 W =1 J/s). To describe the energy density of a device, the term “specific energy”, usually expressed in the unit watt-hours per kilogram, is used to characterize the amount of energy stored per unit mass. However, the weight of the active materials in an energy storage device in form of thin films or aerogels is in many cases negligible and hard to measure accurately. Thus, in addition to the gravimetric energy density that generally used, areal or volumetric energy density are also used to characterize the amount of energy stored per unit area or volume. This standard is suitable to characterize energy storage devices made from thin films and aerogels. Similarly, power density is used to quantitatively described the speed of charge and discharge of an energy storage device. It can be expressed on gravimetric (per unit weight) basis, areal basis (per unit area) and volumetric basis (per unit volume). Specific power is the power density based on unit weight. It is usually expressed in watt per kilogram. Areal or volumetric power density are used as well for the devices in form of thin film and aerogels which are typically hard to accurately measure the weight of active materials.

The performance of the energy storage devices can be concisely shown by the Ragone plot, which shows the energy density and the power density of different energy storage devices. From the Ragone plot shown in Figure 1.2, it can be seen that the performance of supercapacitors (SCs) is between traditional capacitors and batteries. SCs have higher specific power compared with batteries, and higher specific energy compared with traditional capacitors. They fill in the gap between capacitors and batteries, and are suitable for applications that require both high specific power and high specific energy. Fuel cells convert the chemical energy stored inside molecules to electricity. For example, the hydrogen-based fuel cells employ the chemical reaction between hydrogen and oxygen to produce water and electricity. Due to its high energy density and the characteristic of generating only water as the by-product, it is applied as the power source for space shuttle and space craft. The combustion engine and gas turbines are not energy storage devices. They are energy conversion systems that convert the chemical energy of fuels to kinetic or electric energy. They have high specific power and specific energy, but their applications are restricted due to environmental concerns. The choice of energy storage system should be based on the characteristics of their performance, and current research focuses a lot on the improvement on both specific power and specific energy.

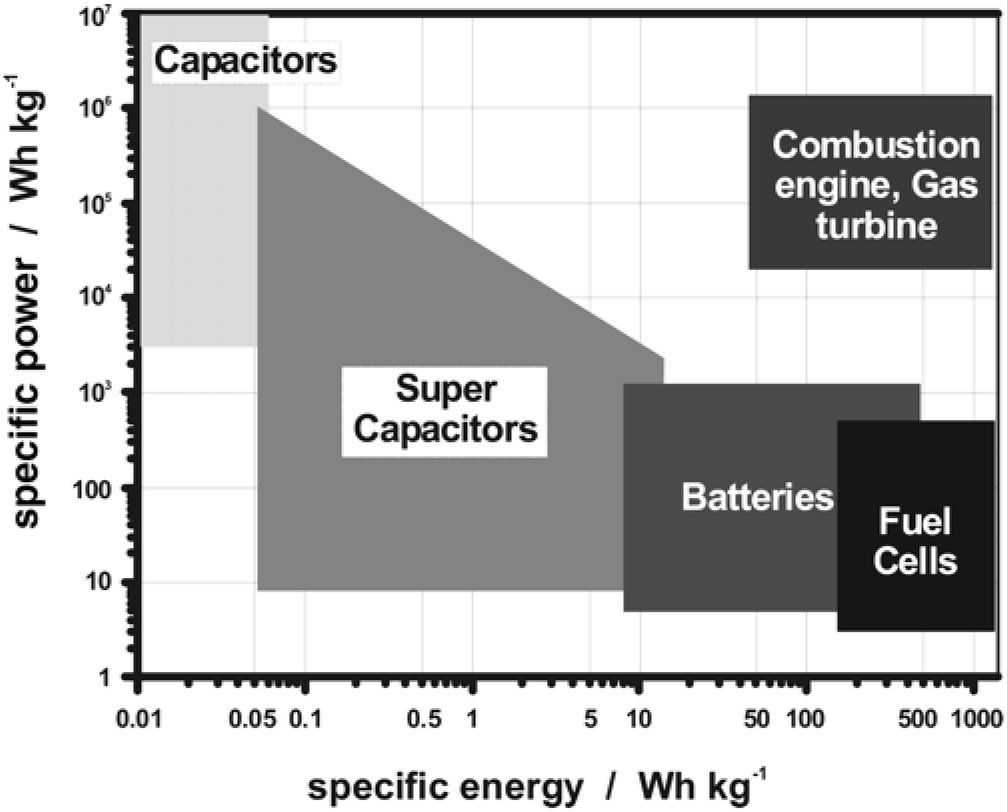

Figure 1.2. Ragone plot of various energy storage devices and energy conversion systems.[33]

1.3.1. Supercapacitors (SCs)

Supercapacitors (SCs), also known as electrochemical capacitors or ultracapacitors, are one of the most promising energy storage devices with many unique advantages. The formal name of such devices should be electrochemical capacitors, which accurately describes the fundamental mechanism for charge storage.[34, 35] In this dissertation, the commonly used word “supercapacitor” is adopted given that the term “supercapacitor” is the widespread trade name of the commercialized devices currently on the market, and it is widely accepted in academic fields as well. Compared with the traditional capacitors, they can deliver many orders of magnitude higher specific and volumetric capacitances. Other advantages include fast charge/discharge rate, high power density, low internal resistance and extremely long cycle life (~millions of charge/discharge cycles).[36] The typical power densities and energy densities of SCs are around 10^5 W/Kg and 10 Wh/Kg, respectively. As a result, the potential of SCs as energy storage devices has been recognized in many fields.

The concept of SCs was first raised by H.I. Becker of General Electric in 1957.[37] After further improvement made by Robert A. Rightmire, his fellow researcher at the Standard Oil Company of Ohio in the 1960s,[38, 39] SCs were commercialized by NEC/Tokin and were available for advanced applications. Other major players in this field include Panasonic, Maxwell Technologies, Nippon Chemi-Con, etc. Despite many different sizes and structures, all the devices store electric energy on the interface between the electrolyte and the electrodes. The most commonly used materials for the electrodes are activated carbons with high surface area and well-developed porous structure. This type of SCs are called electrochemical double-layer capacitors (EDLCs). In recent decades, a new type of SC, which utilizes redox materials capable of fast and reversible redox reaction to storage charges, has been successfully developed and further increased the performance of SCs. The redox reactions of the electroactive materials on the electrodes provide the devices with pseudo-capacitance, which usually offers much larger capacitance per gram than an EDLCs.[40]

Table 1.2. Major manufacturers of SCs and their performance.[41]

Company name	Device name	Voltage range (V)	Capacitance (F)
AVX	Bestcap	3.5–12	0.022–0.56
Cap XX	Super Capacitor	2.25–4.5	0.09–2.8
Copper	Power stor	2.5–5.0	0.47–50
ELNA	Dyna cap	2.5–6.8	0.033–100
ESMA	Capacitor modules	12–52	100–8000
EPCOS	Ultra-capacitor	2.3–2.5	5–5000
Kold Ban	Kapower	12	1000
Maxwell	Boostcap	2.5	1.6–2600
NEC	Super capacitor	3.5–12	0.01–6.5
Nesscap	EDLC	2.7	10–5000
Panasonic	Gold capacitor	2.3–5.5	0.1–2000

Figure 1.3. SCs fabricated by Batscap and Maxwell.[42]

1.3.2. Batteries

Batteries are the most commonly used energy storage devices for portable electronics and many other applications. The history of battery dates back to 1800 when Alessandro Volta invented voltaic cells that consisted of two different metals, usually copper and zinc, immersed in salt solution. Since then batteries have evolved significantly with the application of different materials, such as lead-acid batteries, Ni-Cd batteries and Lithium ion batteries, but the basic mechanism and the structure remain the same. Batteries utilize chemical reactions happen inside to store and deliver energy. They converse the chemical energy into electricity. Chemical reactions happen on the two electrodes of a battery, i.e. cathode and anode. The potential difference between these two electrodes are stable and drives electrons to move from one electrode to another. The cathode is the electrode where reduction occurs; it is the positive end when the battery is discharging. The anode is the electrode where oxidation occurs; it is the negative end when the battery is discharging. Depending on whether or not the battery can be recharged, batteries can be divided into primary batteries and secondary batteries. Because of the chemical reactions of primary batteries cannot be reversed, primary batteries are designed for single time use only. The lifetime of a primary battery comes to an end once the active materials are completely consumed by chemical reactions. Secondary batteries are also referred as rechargeable batteries. They utilize the reversible chemical reactions to provide energy. The chemical reaction will undergo an opposite process when the battery is charging. However, the chemical reactions happen at a relatively slow rate, which causes the power density of a battery to be lower compared with that of SCs.

Lithium ion batteries are famous for their high energy densities. They use graphite as the negative electrode material. The positive electrodes can be made from lithium iron phosphate, lithium cobalt oxide and other different derivatives.[43] The electrolyte is usually lithium salts, such as $LiPF_6$, $LiBF_4$ or $LiClO_4$ in organic solvents such as ethylene carbonate, dimethyl carbonate, and diethyl carbonate. Lithium ion batteries utilize insertion mechanism to store energy. The lithium ions leave the negative electrode and enter the electrolyte, and move towards the positive end when discharging. At the positive end, the lithium ions can be inserted into the electrode material when discharging, and this process can be reversed when charging the battery. Many modifications of lithium ion batteries are being developed, and they show the potential to provide the breakthroughs that are needed to fully utilize the renewable energy sources.[43]

The fundamental difference between the batteries and the SCs is the mechanism used for energy storage. Batteries employ chemical reactants which can release the chemical energy to generate electricity, so the power provided by batteries is limited by the kinetics of the chemical reaction. SCs use the charges stored on the surface of the electrodes to form electrical current, so the power density is higher than batteries. Because of their different characteristics, the choice should be made based on the requirements of the application and they are often combined to form a power system in many cases.

1.3.3. Fuel cells

Fuel cells convert the chemical energy directly into electricity efficiently without pollution. Unlike batteries which employ redox chemical reactions happened on the electrodes, fuel cells consume the fuel and transform the chemical energies of the fuel directly into electricity. The fuel cells serve as electrochemical energy conversion device which consume only fuels and can provide energy as long as fuels are sufficient.[44] The anode and cathode of the fuel cells are just charge-transfer media where the active chemicals undergo the redox reactions. The active chemicals are continuously delivered from outside the cells to compensate the consumption during the redox reactions.[33]

Under the ideal condition, the only by-products of fuel cells are heat and water. Many electric vehicles on the market use hydrogen as the fuel to generate electricity and provide energy. Currently there are several different types of fuel cells under development, such as the alkaline fuel cell (AFC), the polymeric-electrolyte-membrane fuel cell (PEMFC) and the phosphoric-acid fuel cell (PAFC).[45] However, the operation of these cells requires relatively pure hydrogen, which can be expensive and relatively dangerous to store and transport. Other choices of fuels include methanol, ethanol and other alcohols.[46] Fuel cells provide higher energy density than that of batteries, and the power of fuel cells scale well from the several watts range to the megawatts range.

Fuel cell technology represents a different direction for the development of energy storage devices. The high-efficiency, low environment impact, and excellent modularity make the future of fuel cells bright, so governments all over the world pay much attention to the development of fuel cells. However, many vital disadvantages such as high-cost and low durability still need to be solved.[47]

1.4. Fundamentals of supercapacitors

1.4.1. Structure and components of supercapacitors

Although the mechanisms of energy storage and energy conversion for batteries, fuel cells and supercapacitors are different, their structures are quite similar.[33] The structure of supercapacitors consists of two electrodes soaked in the electrolyte (Figure 1.4). The electrodes are connected to the current collectors that are made from highly conductive materials, and the current collectors are directly connected to the external circuit. A thin, porous, non-conductive and ion-permeable membrane, usually made of polypropylene films or cellulose papers, is placed between the two electrodes to prevent short circuit caused by faulty contact of these two electrodes. The requirements for separators include high electrical resistance, high ionic conductivity, strong mechanical strength and flexibility. It has been reported recently that the natural and hierarchically ordered microporous eggshell film can work as the separators for supercapacitors.[48] Poly(vinylidene fluoride)-based macroporous separators have been investigated and the results show that poly(vinylidene fluoride) separators exhibit highly porous structure, good mechanical properties and enhanced ionic conductivity that outperform the commercial cellulose-based separators and the Celgard™ separators.[49] In another research, poly(vinylidene fluoride) and polyethylene non-woven is developed, in which the polyethylene matrix contributes to the mechanical strength and thermal shut-down properties, while the poly(vinylidene fluoride) component provides a hydrophilic ionic conducting phase.[50] The ionic conductivity of the as-developed separator can reach 8.9×10^{-4} S/cm at 25 °C. In general, to reduce the mass and volume of the overall device, the separators are expected to be as thin and lightweight as possible, but still can provide sufficient tensile strength and offer good stability throughout the life cycle of the devices.

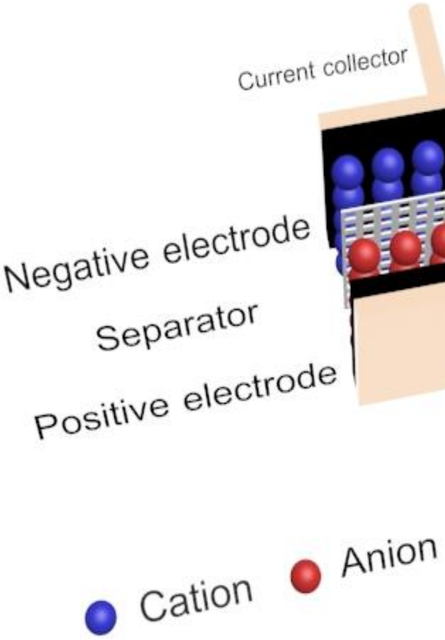

Figure 1.4. Structure of a supercapacitor.

The most important component of a supercapacitor is the electrode, which determines the overall electrochemical performance of the device. The two electrodes in a supercapacitor can be made with the same electrode materials to form a symmetric structure, or can be made with different electrode materials to form an asymmetric structure (Figure 1.5). In practice, the supercapacitors using the same materials for both electrodes are called symmetrical supercapacitors, while the supercapacitors using different electrode materials for the two electrodes are referred as asymmetrical supercapacitors. For a symmetric supercapacitor, either electrodes can be used as the positive electrode or the negative electrode because they are made from the same material. The symmetric structure is typically used in the electric double-layer capacitors (EDLCs), in which the electrodes are usually made from carbon-based materials, e.g. activated carbons, graphene-based materials, carbon nanotubes and carbon aerogels.[51] For an asymmetric supercapacitor, the electrode that works at a higher voltage range is the positive electrode, and the electrode that works at a lower voltage range is the negative electrode. The positive electrodes are made from the electrode materials that operates in a positive voltage region, usually conductive polymers or transition metal oxides.[52] The negative electrodes are made from the materials that operates in a negative voltage region, usually carbon-based materials and carbon/polymer composites. The asymmetric structure is typically used in the pseudocapacitors and the hybrid capacitors. Because the working voltage ranges of the positive electrodes and the negative electrodes are different in asymmetric supercapacitors, the overall voltage window can be larger than that of the symmetric supercapacitors, which can effectively increase the energy density of a supercapacitor.[53] It should be noted that since redox reactions are not involved in the electrochemical double layer capacitors, the terms "anode" and "cathode" should be avoided because these terms are defined by the types of reactions occur on the electrodes, not by the value of the electrical potentials of the electrodes. Although redox reactions are involved in pseudocapacitors, people usually use the terms "positive electrode" and "negative electrode" to avoid confusion.

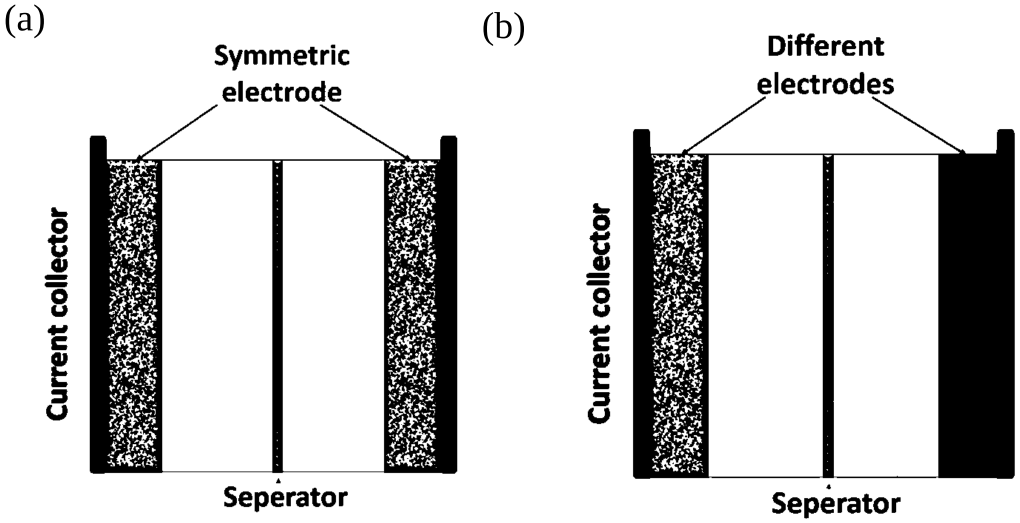

Figure 1.5. (a) Symmetric and (b) asymmetric supercapacitors.[54]

The space between the two electrodes of a supercapacitor is not filled with dielectric layers as the conventional capacitor usually does. For supercapacitors, the space between the two electrodes is occupied by electrolytes so that supercapacitors can use the electric double layers formed at the interfaces between the electrolyte and the electrodes to store energy. The electrolytes contain free-moving ions that can migrate when an external voltage is applied between the electrodes, which makes the electrolyte ions regularly distributed on the interface between the electrolyte and the electrodes to form the electric double layers. The electrolyte can be either in the form of a liquid solution or in solid state as long as the ionic conductivity is high enough.[55] Aqueous electrolytes are the most commonly used electrolytes. They can provide acidic, neutral, or alkaline environment depending on the best working environment of the electrode materials. The aqueous electrolytes are nonflammable, facile to prepare and can provide high ionic conductivity. However, the working voltage of aqueous electrolytes is usually limited below 1 V because the water molecules will start to decompose at voltages higher than 1 V. Besides, liquid electrolytes may also cause leakage, which has the potential of damaging the device. Organic electrolytes, such as tetraethylammonium tetrafluoroborate and triethylmethylammonium tetrafluoroborate in acetonitrile, can provide a wider voltage range between two electrodes because these organic electrolytes are less prone to decompose compared with aqueous electrolytes. However, several disadvantages such as high flammability, toxicity, and high cost restrict their applications. Ionic liquids such as N-butyl-N-methylpyrrolidinium bis(trifluoromethanesulfonyl)imide and triethylammonium nitrate, which basically are molten salts consist of organic ions at room temperature, have also been investigated as electrolytes.[56, 57] It has been reported that for the same electrode materials, ionic liquid electrolytes provide the highest specific energy while aqueous electrolytes provide the highest power density.[58] Finally, besides the liquid electrolytes, solid state electrolytes have been developed as well. Solid electrolytes allow the movement of ions without liquid components, which can be very useful for the fabrication of flexible and all-solid-state devices.[59] Ionic liquid and silica-based gel electrolytes have been reported to have a better performance than the commonly used H_2SO_4/poly(vinyl alcohol)-based solid electrolytes.[60] To sum up, the performance of electrolytes is evaluated based on the ability to provide free ions and the mobility of the free ions. Aqueous electrolytes have the advantages of high cost efficiency and environmentally friendliness. Organic electrolytes and ionic liquid electrolytes can provide higher voltage windows and higher energy densities. The choice of the electrolyte in a supercapacitor should be based on its electrode materials and the performance requirements for the device.

1.4.2. Theoretical models and calculations of supercapacitors

Capacitance is used to describe the ability of a device to store electric charges. It is defined as:

$$C = \frac{dQ}{dV}$$

where Q is the amount of charges in coulombs, V is the voltage in volts, and C is the capacitance in joules per coulomb. The simplest model of a capacitor consists of two parallel metal plates with a surface area of A at a distance of d separated by a dielectric with a permittivity of ε. Theoretical calculation shows that the capacitance can be calculated by:

$$C = \frac{\mathrm{\varepsilon A}}{d}$$

It should be noted that the permittivity and distance between the electrodes are determined by the electrolyte and the structure of the device, respectively. They have little room to modify.

Based on the above equation, it can be deduced that to increase the capacitance, the most effective method is to increase the surface area of the electrodes.

The energy stored by a capacitor (W) during a fully charging process can be calculated by the following equation:

$$W = \int_0^Q U(q)dq = \int_0^Q \frac{q}{C}dq = \frac{Q^2}{2C} = \frac{1}{2}CU^2$$

where Q is the amount of charge when the capacitor is fully charged, U is the voltage across the capacitor, and C is the capacitance.

When the capacitor starts to release the charges and supply energy to the external circuit, the voltage will decrease as the amount of charges decreases. The power of the device at a given time can be calculated as:

$$P = \frac{dW}{dt} = CU(t)\frac{dU(t)}{dt}$$

The average power during a discharging cycle can be calculated as:

$$P = \frac{W}{T} = \frac{CU^2}{2T}$$

where W is the energy stored by a capacitor in a full charge, which is equal to the amount of energy released through a complete discharge. T is the time of the discharging process.

1.4.2.1. Models of the electric double layers

The double layers are two parallel layers of opposite charges that are separated at an atomic distance on the electrode/electrolyte interface. Various models are proposed to illustrate the formation of the electric double layers, including the Helmholtz model, the Gouy-Chapman model, the Stern model and the BDM (Bockris, Devanathan, and Muller) model (Figure 1.6).[61] The Helmholtz model was first proposed by von Helmholtz in 1853 to explain the distribution of opposite charges at the interface of colloidal particles.[62] This model assumes that two layers with opposite charges are formed and distributed at the electrode-electrolyte interface, and these two layers are separated at a distance around 0.1 nm, i.e. the size of a single atom. However, this model failed to explain the continuous distribution of ions caused by the irregular thermal fluctuation. Gouy and Chapman further developed this model by introducing the diffuse layer, which is formed by the continuous distribution of the electrolyte ions in the electrolyte solution due to the thermal motion.[63] The Stern model combines the Helmholtz model and the Gouy-Chapman model by assuming two co-existing regions of ion distribution.[64] The inner region close to the electrode is called the compact layer or Helmholtz layer where ions are strongly adsorbed by the electrode. The diffuse layer is the same as defined by the Gouy-Chapman model. The inner Helmholtz plane (IHP) and outer Helmholtz plane (OHP) are the imaginary planes between the Stern layer and the diffuse layer. The IHP is formed by the monolayer of polarized solvent ions, and the OHT is formed by the charge ions in the electrolyte. They have different types of adsorbed ions and are electrostatically attracted together to form the double layer.

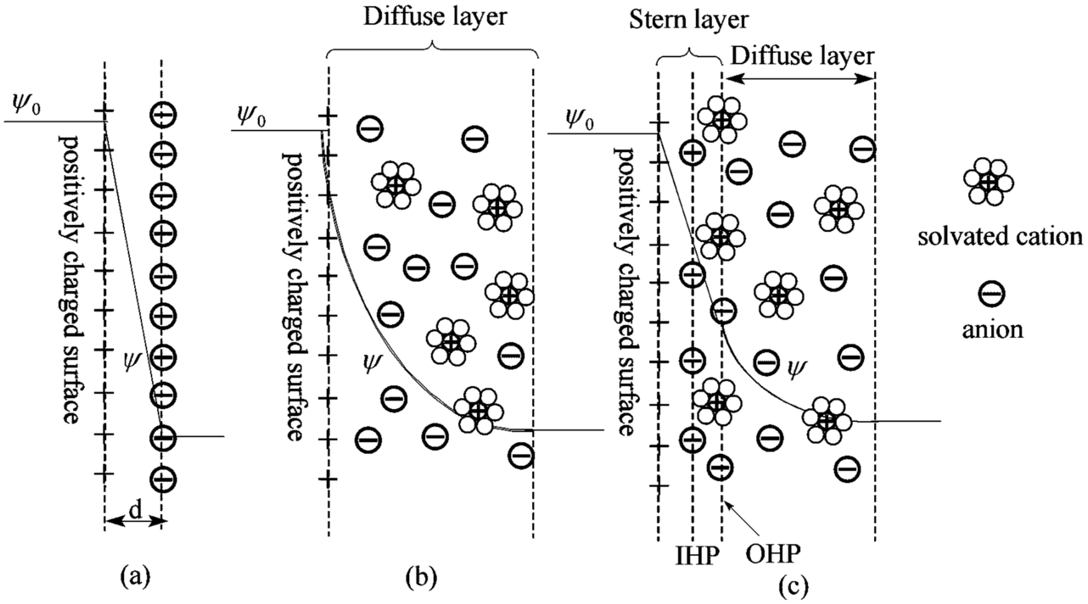

Figure 1.6. Models of electrical double layer at a positively charged surface: (a) the Helmholtz model, (b) the Gouy-Chapman model, and (c) the Stern model.[65]

The Helmholtz model assumes the capacitor is simply formed by two layers of opposite charges, which is similar to that of the two-plate conventional capacitors. The capacitance can be calculated similarly by:

$$C_H = \frac{\varepsilon}{d_H}$$

where d_H is the thickness of the Helmholtz layer and ε is the permittivity of the electrolyte solution.

However, the ions do not stay compact and static all the time due to the thermal fluctuation. There is a continuous change of charge density caused by the thermal motion of ions from the electrode to the electrolyte solution. In the Gouy-Chapman model, the thermal fluctuation factor was brought into consideration and a modified calculation of the double layer was proposed. The capacitance is expressed as:

$$C_{diff} = \frac{\varepsilon}{\lambda_D}$$

where C_{diff} is the diffusion capacitance and λ_D is a constant determined by temperature, the ionic concentration of the solution and other properties of the electrolyte. However, because the calculation assumes that the ions are point charges and there is no limitation on the distance between the ions and the surface, the Gouy-Chapman model tends to overestimate the capacitance.

The capacitance calculated by the Stern model is given by:

$$\frac{1}{C_{cl}} = \frac{1}{C_s} + \frac{1}{C_{diff}}$$

where C_{cl} is the overall capacitance, C_s is the Stern-type compact double layer capacitance and C_{diff} is the diffuse layer capacitance.

The most recent model was developed by Bockris, Devanathan and Muller in 1963.[66] In this model they considered the effect of the interaction between the electrode and the dipoles, and they proposed that a layer of water was present within the inner Helmholtz plane at the surface of the electrode (Figure 1.7).

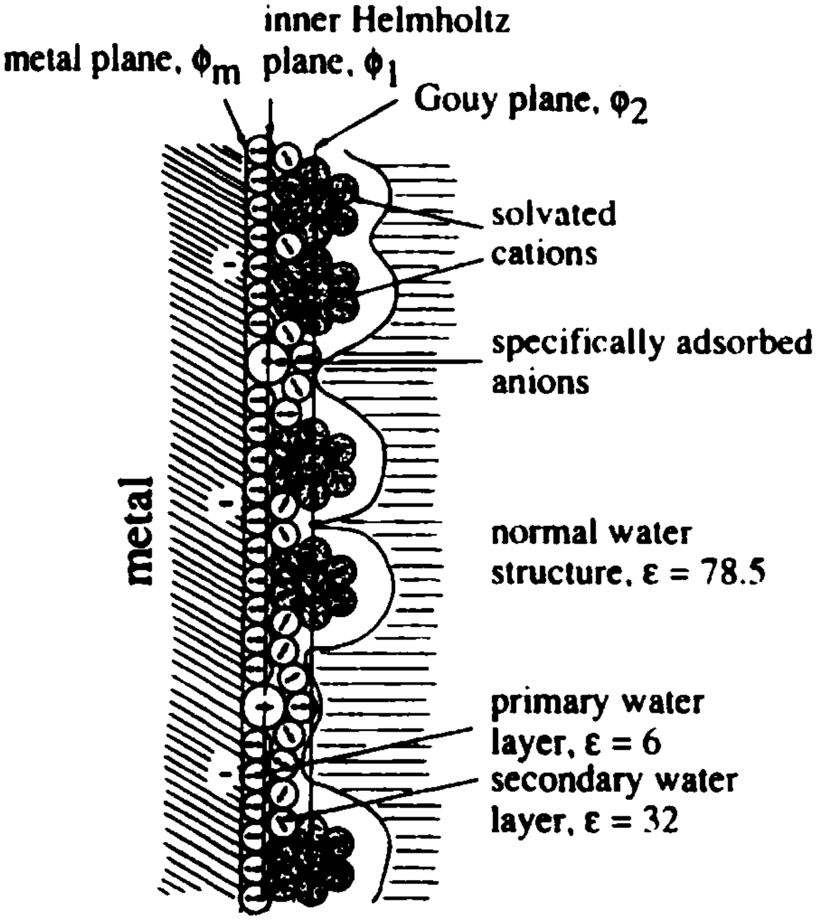

Figure 1.7. BDM (Bockris, Devanathan, and Muller) model.[67]

1.4.2.2. Theory of pseudocapacitors

Pseudocapacitors store energy electrochemically instead of electrostatically in the double layers. Pseudocapacitors use similar energy storage mechanism as the batteries, but the electrochemical processes in pseudocapacitors are much faster than in batteries. The fast charge/discharge ability makes pseudocapacitors behave like the electric double-layer capacitors (EDLCs) with high power densities, so people generally view them as a special type of supercapacitors.

In contrast to the EDLCs which use the double layers to store energy electrostatically, the electrodes of pseudocapacitors contain special electroactive materials such as metal-doped carbons, conducting polymers, or transition metal oxides. The electroactive materials can undergo quick and reversible adsorption/desorption of the electrolyte ions on the electrode surface, or can undergo oxidation and reduction reactions, which involves the charge transfer by means of redox reactions. These fast and reversible charge transfer process can be viewed as the device being rapidly charged and discharged, which results in a capacitive behavior. This type of capacitance caused by the reversible Faradaic reactions occurring on the electrodes is called "pseudocapacitance". The term "pseudocapacitance" is used to differentiate from capacitance provided by the electric double layers. The intercalation, electrosorption and insertion/adsorption of ions can also happen on the electrodes of pseudocapacitors, which is similar to the working process of the lithium-ion batteries and can further increase the capacitance of the device.

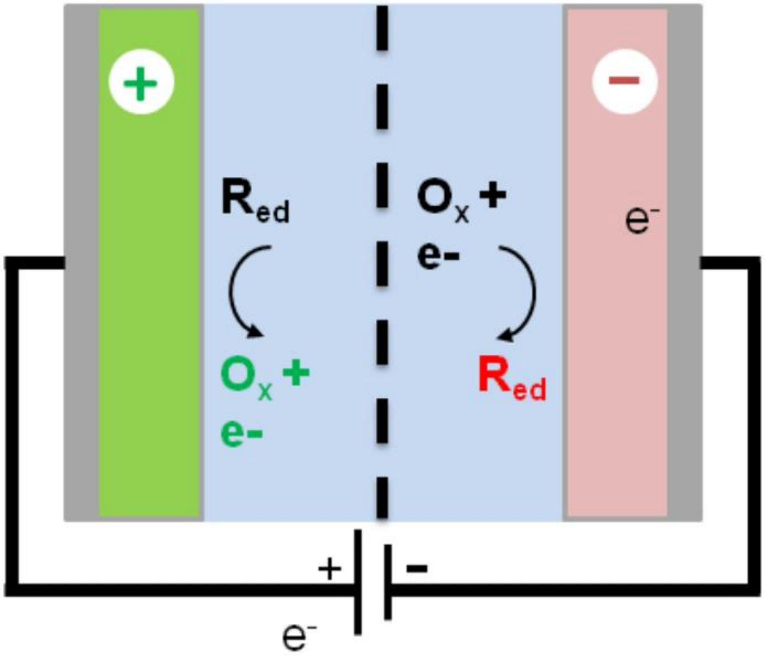

Figure 1.8. The oxidation/reduction process happened in a pseudocapacitor.[68]

It should be noted that the double layers are also present in pseudocapacitor electrodes, so the electrostatic double-layer capacitance always exhibits in pseudocapacitors. The combination of these two different energy storage mechanisms can provide a high capacitance. However, the performance of pseudocapacitors usually deteriorate at high current densities, and the life cycle is also smaller than that of EDLCs.

1.4.3. Test methods of supercapacitors

To characterize the performance of an energy storage device, several electrochemical test methods are widely used. These standard test methods can be carried out using the potentiostats/galvanostats (known and promoted by instrument manufacturers as electrochemical workstations) with build in preset test programs, which can detect and record the response signals of either potential or current of an electrochemical system when applied a known potential or current input. The electrochemical system usually consists of a working electrode (WE) made from the active materials that are being tested, a reference electrode (RE) to provide a stable potential for reference, and a counter electrode (CE, also known as auxiliary electrode) that often fabricated from the electrochemically inert materials such as gold, platinum, or carbon, to form a complete current circuit. A three-electrode system contains the WE, the RE and the CE (Figure 1.9). The electrical current between the working electrode and the counter electrode is either applied or measured, and the potential difference between the working electrode and the reference electrode is either applied or measured.

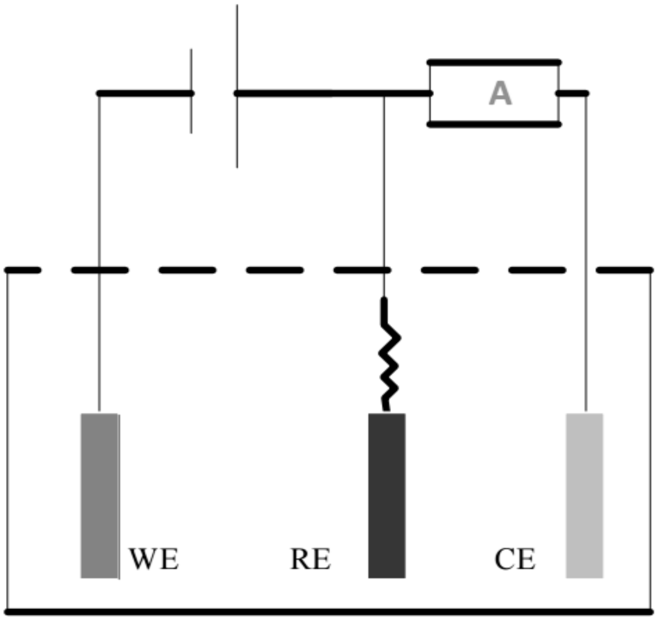

Figure 1.9. Equivalent circuit of the three-electrodes setup.[68]

A two-electrode system consists of a working electrode and a counter electrode. In fact, the counter electrode also serve as the reference electrode in a two-electrode system, but the potential of counter electrode changes during the measurement process, which makes the absolute voltage value differ from the measurement done by a three-electrode system. Both the current and the potential difference between the working electrode and the counter electrode are recorded in a two-electrode test. Based on the different measurement setups, it can be seen that a three-electrode system is good to accurately characterize the performance of a single working electrode, while the two-electrode system is more suitable for the measurement of the overall performance of a device. The commonly used test techniques are discussed in detail as follows.

1.4.3.1. Cyclic voltammetry (CV)

Cyclic voltammetry (CV) test is a widely-used technique to study the electrochemical properties of the electrode materials. A three-electrode setup is usually used in a CV test. In this test, a continuously sweeping voltage is applied between the working electrode and the reference electrode, and the response current between the working electrode and the counter electrode is recorded. The voltage range is fixed and the voltage is scanned from one end of the voltage range to the other end of the voltage range. When the voltage reaches the designated limit, the sweeping process is reversed towards the opposite direction.

The electrode potential sweeps in a specific voltage range with a constant sweep rate v:

$$v = \frac{dV}{dt}$$

where V is voltage of the working electrode. The current can be calculated as:

$$i = \frac{dQ}{dt} = \frac{CdV}{dt} = Cv$$

Therefore, the capacitance of the electrode can be calculated from the CV test using the following equation:

$$C = \frac{i}{v}$$

The above equation shows that for an ideal capacitor with a constant capacitance, the current i should remain constant during the CV test, thus the corresponding CV curve should be rectangular (Figure 1.10).

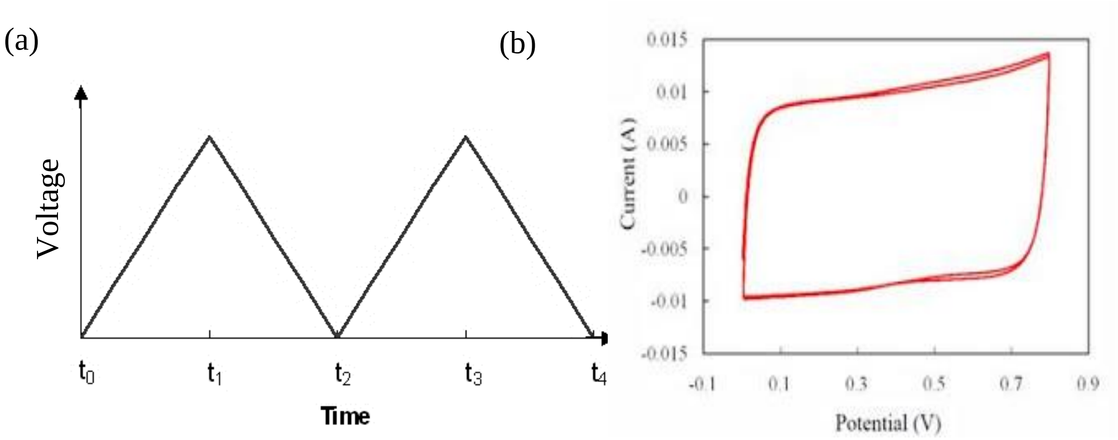

Figure 1.10. (a) The voltage input of the CV test. (b) A typical CV curve of a supercapacitor.

1.4.3.2. Cyclic charge/discharge test (CCD)

Cyclic charge/discharge test (CCD), also known as the chronoamperometry, is usually used to evaluate the capacity and life span of the supercapacitors and the batteries. In this test, the device being tested is charged using a constant current until the voltage reaches the designated value, and it is discharged at a fixed current (usually the same as the current for charging process) until the voltage reaches the lower designated value. The voltage range is determined by the electrode materials and the electrolyte used in the supercapacitor. A full charge and discharge procedure is called a complete cycle. The charge-discharge cycles are repeated for up to thousands of times to test the life span of the devices. The voltage response of the device over time is recorded.

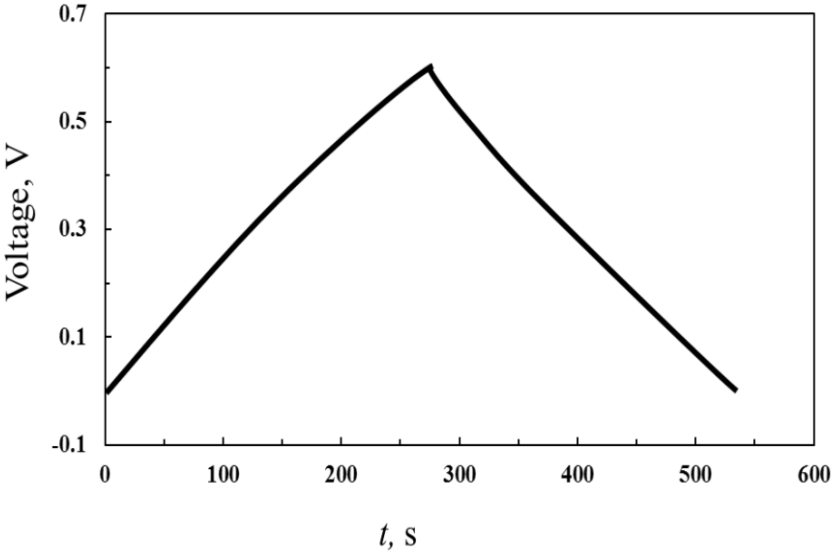

Figure 1.11. A typical CCD curve.

The capacitance can be calculated by the following equation:

$$C = \frac{I \times \Delta t}{\Delta V}$$

where I is the discharge current, Δt is the discharge time and ΔV is the voltage window from the starting point to the ending point of the discharge process. The capacitance can also be calculated using the charge time instead of the discharge time by the same equation, but the charge time is usually shorter than discharge time because of the leakage current, which yields a smaller capacitance. Coulombic efficiency is used to evaluate the efficiency of the device. It is defined as the ratio of the discharge time to the charge time. It should be noted that for an ideal supercapacitor with high Coulombic efficiency, the CCD curve of a complete charge/discharge cycle should be symmetrical triangular shaped. For a real device, the equivalent series resistance (ESR) of the device causes a sudden voltage drop (known as IR drop) at the beginning of discharging process, which reduces the efficiency of a device.

1.4.3.3. Electrochemical impedance spectrometry (EIS)

Electrochemical impedance spectrometry (EIS) is a complicated and powerful technique that provides more information on the frequency behavior of the system. It is usually used to investigate the electrochemical performance of a system in depth, such as the ohmic resistance, the charge transfer resistance and the mass transfer rate. In the EIS test, a small excitation signal (usually a sinusoidal voltage signal around 5~10 mV) is applied to the electrochemical system. This applied sinusoidal voltage results in an alternating current, and the magnitude and the phase of the response current are recorded over a wide frequency range. Under an ideal condition, the current response to the sinusoidal voltage input is also sinusoidal at the same frequency but with a phase shift. The frequency scanned in a complete EIS test usually ranges from ~1 MHz to ~0.01 Hz.

The Nyquist Plot can be derived by plotting the real part of the impedance on the X-axis and plotting the imaginary part on the Y-axis (Figure 1.12). Each point on the Nyquist Plot represents the impedance at that frequency. The points on the left side of the curve represent the impedance at high frequencies, and the points on the right side represent the impedance at low frequencies. The angle between the vector from the origin to the impedance points and the X-axis represents the phase angle at that frequency. The Bode plot is another type of plot that can show the frequency information of the EIS data. It is created by plotting the log frequency on the X-axis, and plotting both the absolute values of the impedance and the phase-shift on the Y-axis.

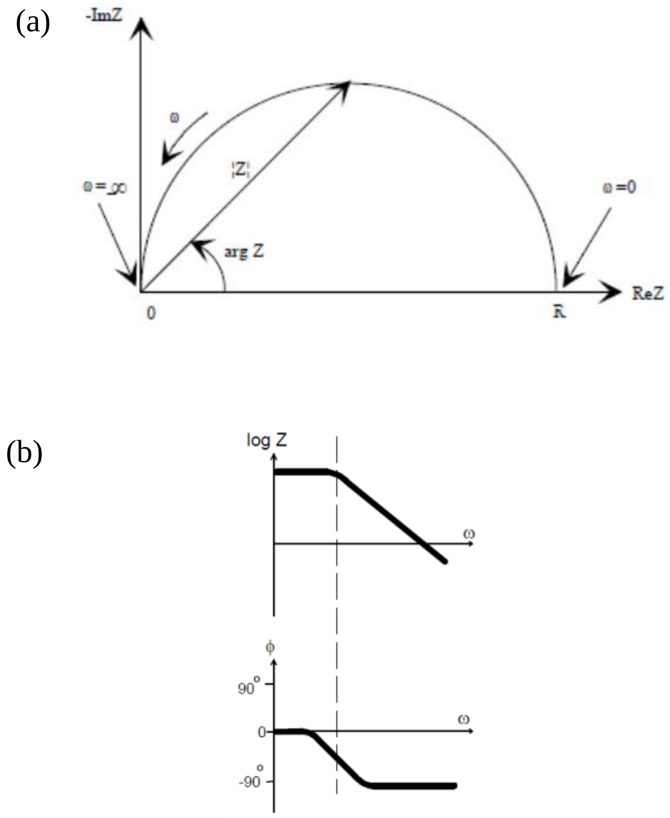

Figure 1.12. (a) A typical Nyquist plot. (b) A typical Bode plot.[68]

The capacitance can be calculated from the EIS data by the following equation:

$$C = -\frac{1}{\omega Z''} == -\frac{1}{2\pi f Z''}$$

where ω (s^{-1}) is the frequency of the excitation signal, f is the frequency in hertz (Hz), and Z'' (Ω) is the imaginary part of the impedance.

1.5. Materials for electrodes of supercapacitors

1.5.1. Carbon-based materials

Carbon-based nanomaterials show many unique properties (e.g., chemical and thermal stability, electrical conductivity, mechanical strength, etc.) and have attracted intense research interests in the fields of chemistry, materials science and condensed matter physics.[69, 70] Different allotropes of carbon (e.g., charcoal, graphite, diamond, fullerenes, carbon nanotubes and graphene) exhibit various microstructures, morphologies, crystallinities, and other physical and chemical properties.[71] Carbon-based materials can be produced in different physical forms (e.g., powders, fibers, foams, aerogels, fabrics, composites, etc.), which, together with their wide-ranging physical and chemical properties, render carbon an important material in many different industries and sectors, especially in the sector of energy storage devices (e.g., lithium ion batteries, supercapacitors, fuel cells, etc.). For this application, carbon materials' high electrical conductivity, large surface area and interconnected porous structure are highly suitable properties for the electrodes in the energy storage devices.[72, 73]

1.5.1.1. Activated carbons

Activated carbons (ACs), one of the most commonly used carbon materials in both the academia and the industry, are carbonaceous material with large surface area and well-developed porous structure. The history of ACs dates back to 1500 BC when Egyptians used activated charcoals as the adsorbent of the pollutants and the purifying agents.[74] Currently it is widely used for gas and water purification, sewage treatment, air filters in gas masks and respirators, filters in compressed air and many other applications.

ACs can be produced by pyrolysis of the raw materials followed by physical or chemical activation of the carbonaceous precursors.[75] After the initial pyrolysis step, a product with high carbon content is produced, so this step is also known as the carbonization of the raw materials. The activation step involves the primarily oxidation of the carbonaceous materials by activation agents. It is used to create porous structure and to increase the surface area. The activation can be carried out either by the reaction with oxidizing gases such as steam and carbon dioxide, or by reacting with chemical activating agents such as potassium hydroxide, zinc chloride and phosphoric acid. In some cases, the carbonization and activation can be combined and carried out at the same time. A two-step method is generally used to make ACs: the raw materials are pyrolyzed to remove most of the non-carbon materials, and then the resultant char is activated to create open pores.[76] Both the physical and the chemical methods can be used for the activation. In the physical method the activation occurs at elevated temperatures in the presence of oxidizing gases such as carbon dioxide or steam.[77] The chemical activation method combines the carbonization and the activation into one step, in which the raw materials are impregnated with the activation agents (e.g., zinc chloride, phosphoric acid, potassium hydroxide, etc.) and heated to a relatively low temperature for simultaneous carbonization and activation. Besides its simplicity and lower temperature requirement, the chemical activation often results in much higher yields and better-developed pore structures.[78]

The application of ACs is based on their unique properties derived from the high surface area and the well-developed porous structure. The pore population of ACs usually includes micropores (< 2 nm), mesopores (2-50 nm) and macropores (> 50 nm). The porous structure of ACs allows them to adsorb materials from the liquid and the gas phase, as such, they have been used for air pollution control, water treatment, catalyst supports, etc. Besides, they are currently the most widely used electrode materials in supercapacitors.[79, 80] The large surface area of ACs (up to thousands of square meters per gram) contributes to the high capacitance of supercapacitors because the electrochemical properties of the electrodes is proportional to their surface areas.[75] Among the three pore types, the micropores play an especially important role in determining the capacitance because they are the major contributors to the surface area and are accessible to most of the electrolyte ions. Carbon materials are generally inexpensive and chemically stable in different electrolyte solutions, even in the harsh electrolytes such as a KOH solution. As such, many researches have focused on the development of novel carbon materials for the high-performance energy storage devices in recent years.

1.5.1.2. Graphene

Graphene is a two-dimensional material with a unique crystal structure. It is formed by carbon atoms bonded together in a hexagonal honeycomb lattice (Figure 1.13). Graphene can be viewed as a single atomic layer of graphite, so by peeling off the graphite using simple tools such as the adhesive tapes, single-layer graphene can be eventually produced.[70] Although the graphite was discovered thousands of years ago and can be easily found in natural minerals, it was generally believed that a single layer of carbon atoms cannot exist before the discovery of graphene. Since it only has one layer of atoms, it is known as the thinnest material. Besides, it has high mechanical strength, high thermal and electrical conductivity, which makes graphene one of the most popular materials nowadays. Previous research show that the Young's modulus of graphene can be as large as 1 TPa.[81] The thermal conductivity of graphene is as large as 5000 W/(m•K), and the electrical conductivity can reach 6000 S/cm.[82, 83]

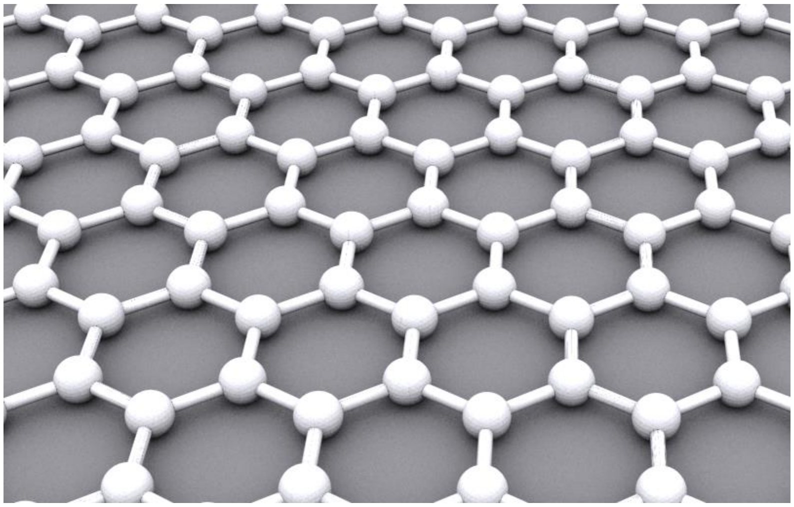

Figure 1.13. Structure of graphene.

High quality graphene can be produced in large scale using different methods. Although the mechanical exfoliation is possible to produce high-quality graphene, its efficiency is low and the quality of the graphene is hard to control, so it is only a proof of concept method rather than a practical method for large-scale production. Currently the most widely used method is the chemical reduction of graphene oxide (GO). The synthesis of GO was first developed by Hummers and Offeman in 1958 (known as the Hummers' method), and was further improved by many researchers.[84] To prepare GO, graphite is exfoliated and oxidized by strong chemical agents such as H_2SO_4, $KMnO_4$ and hydrogen peroxide. Due to the rich functional groups such as carboxylic acid, epoxide and hydroxyl groups on the GO structure, GO can be uniformly dispersed in water and are compatible with many materials such as the soluble polymers. GO can be treated by reducing agents to remove the functional groups on the surface of the carbon layer to produce pure graphene.

Graphene is a good candidate for the electrode materials of supercapacitors. The surface area of graphene can reach up to 2630 m^2/g, which promotes the EDLC behavior.[85] The high conductivity can effectively reduce the ESR and increase the Coulombic efficiency of the device.

1.5.1.3. Carbon nanotubes (CNTs)

Carbon nanotubes (CNTs) are tube-shaped materials made of carbon atoms. The structure of CNTs can be viewed as the graphene sheets rolled up to form the hollow cylindrical nanostructures (Figure 1.14). The elastic modulus of CNTs can be as high as 1 TPa, which is almost 100 times higher than that of steel.[86] Depending on the number of graphene layers in the tube, CNTs can be divided into two categories, i.e. single-walled carbon nanotubes (SWCNT) and multi-walled carbon nanotubes (MWCNT). The SWCNT contains only one single rolled graphene sheet, so the diameter of the tube is only 1~2nm. The MWCNT contains multiple layers of graphene in the tube, so the diameter can be as large as 100 nm.[87]

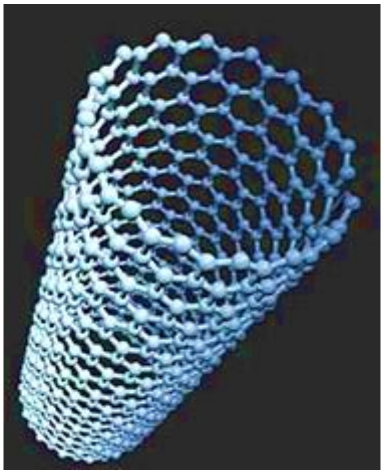

Figure 1.14. Structure of single-walled CNTs.

In the electrode applications, the CNTs function differently than the ACs. The high aspect ratio of CNT favors the formation of an entangled CNT network with interconnected porous structure. The pores of CNTs are open and accessible. The pores are in the range of mesoporous region rather than in the micropores region as in the ACs. As a result, the surface areas may not be as large as that of ACs, but they are accessible to almost all the electrolyte ions. Furthermore, the good conductivity can effectively increase the performance of the cell by reducing the energy dissipation caused by the internal resistance. Because of their high conductivity and low percolation limit, they can form a three-dimensional conducting network in the electrodes and functions as the conductive additive. Besides, CNTs can be functionalized to facilitate the dispersion in different solvents so that they have compatibility with many composite materials. The functional groups can improve the wettability of the electrodes produced by the CNTs, and the pseudocapacitance can be introduced into the cells due to the Faradaic reactions caused by the oxygen and nitrogen atoms in the functional groups. As such, the CNTs are ideal substrate for the pseudocapacitors and are often used to support the pseudocapacitive materials such as the metal oxides and the conducting polymers to achieve high pseudocapacitance.

1.5.1.4. Carbon aerogel

Aerogels are porous and ultralight solid materials that are typically derived from hydrogels. Instead of the absorbed liquids in hydrogels, most of the internal space in aerogels is occupied by air. Aerogels are often referred to as “frozen smoke” or “solid smoke” due to their extremely low density. When converting hydrogels into aerogels, the liquid component of the hydrogels is extracted by a freeze-drying or supercritical drying process, which removes the liquid while maintaining the delicate gel network structure.

Carbon aerogels have a three-dimensional (3D) mesoporous network structure formed by the condensation of the carbon nanoparticles. The 3D network provides high surface area and accessible pathway for the electrolyte ions. Some previous studies argue that the micropores, although exhibiting large surface area, are considered too small for ions to enter and therefore contribute little to the energy storage (Figure 1.15). Macropores, on the other hand, create relatively small surface area and offer low capacitance.[88] The mesopores with fully accessible surface area formed by the carbon aerogels are considered as the ideal structure for high capacitance. Besides, the electrical conductivity of the carbon aerogels can be increased by improving their degree of graphitization. Therefore, carbon aerogels are ideal electrode materials for supercapacitors. Pseudocapacitance can also arise from the surface functional groups of carbon aerogels, which can further increase their energy storage performance.[89]

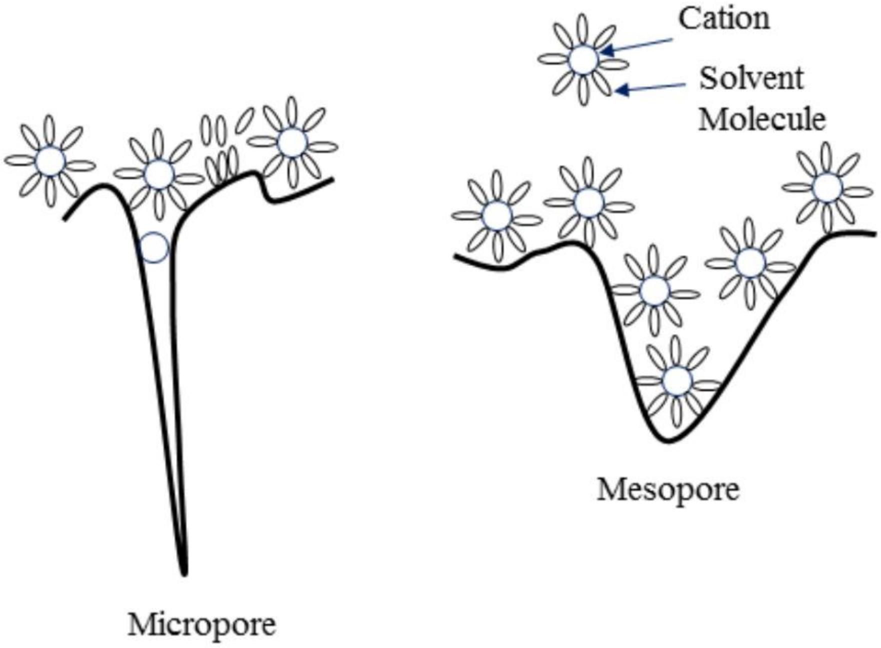

Figure 1.15. The adsorption of electrolyte ions by electrodes with different pore sizes.[90]

Carbon aerogels can be easily prepared by the direct pyrolysis of the organic aerogels formed by many polymeric composites such as resorcinol-formaldehyde (RF), phenol-furfural (PF), phenol-resorcinol-formaldehyde, melamine-formaldehyde (MF).[89] The gels are typically prepared by the sol-gel method, through which the gel pores are formed by the interconnected colloidal nanoparticles. By adjusting some parameters such as the pH, the temperature and the concentration of the gel, the pore size and their distribution can be accurately controlled. Besides, carbon aerogels can also be produced by the direct pyrolysis of bacterial cellulose, which is a natural aerogel formed by interconnected networks of cellulose nanofibers. It has been reported that by the pyrolysis of bacterial cellulose at 1300 °C under argon atmosphere, a highly conductive and stretchable carbon aerogel was formed and show excellent fire-resistant property and compressibility.[91] This novel method of preparing carbon aerogel from bio-based materials and its application in the electrodes of supercapacitors will also be discussed in this dissertation.

1.5.2. Conducting polymers (CPs)

Conducting polymers have distinctive carbon chains formed by the alternating C-C bond and the C=C bond, which are known as the conjugated chains. Polymers with the structure of conjugated chains are called conjugated polymers. The valence electrons are not bound by the atomic nucleus but are delocalized on the conjugated chain, which causes an increased mobility on the chain and brings the conductivity of the polymer to semi-conductor level (10^{-11} to 10^{-3} S/cm).[92] The simplest conjugated polymer is the polyacetylene (Figure 1.16), which contains only the conjugated backbone without any other functional groups. In their cooperative work done by Heeger, MacDiarmid and Shirakawa in the 1970s, they found that the conductivity of polyacetylene could reach the degree of metallic materials when it was oxidized by iodine or bromine.[93] Their work proves that the conductivity of conjugated polymers can be remarkably increased to the metallic level by the doping process.

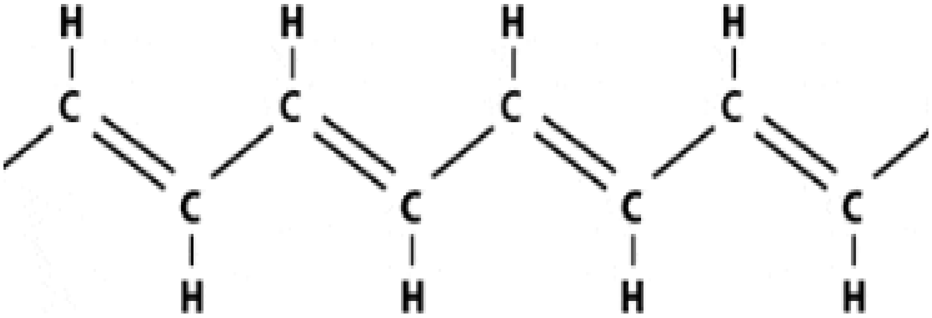

Figure 1.16. Structure of the conjugated chain (polyacetylene).

Since then, the theory for the high conductivity of the conducting polymers has been established gradually. It is widely accepted that the conjugated polymers become conductive after the doping process, which is to disturb the delocalized electrons on the conjugated backbone either by reduction or by oxidation. Two types of doping are available, i.e. the p-doping by oxidation and the n-doping by reduction. The p-doping is done by removing electrons from the polymer chain and adding anions from the electrolyte into the conjugated chain. The n-doping is done by the reduction of the polymer chain, which is essentially the opposite process of N-doing. After doping, the mobility of the charge carriers is increased and the whole molecule becomes conductive.

The capacitance of CPs-based supercapacitor is caused by the pseudocapacitive behavior in the doping process. The CPs on the electrodes can be electrochemically oxidized or reduced, which is essentially a Faradic reaction that gives rise to the pseudocapacitance. CP-based SCs usually have a higher energy density than the EDLCs and can bridge the gap between the batteries and the EDLCs. Besides their good electrochemical properties, CPs also have some unique mechanical properties. They are lightweight and flexible, which is ideal to fabricate flexible devices that can be bent or twisted. CPs are stable in strong acid or alkaline electrolytes, which makes the choice of electrolytes more versatile. Besides, the techniques used to process commercial polymers can still be applied for the synthesis of CPs, which makes large scale fabrication in industry feasible. The molecule structures of some commonly used CPs for electrode materials are shown in Figure 1.17.

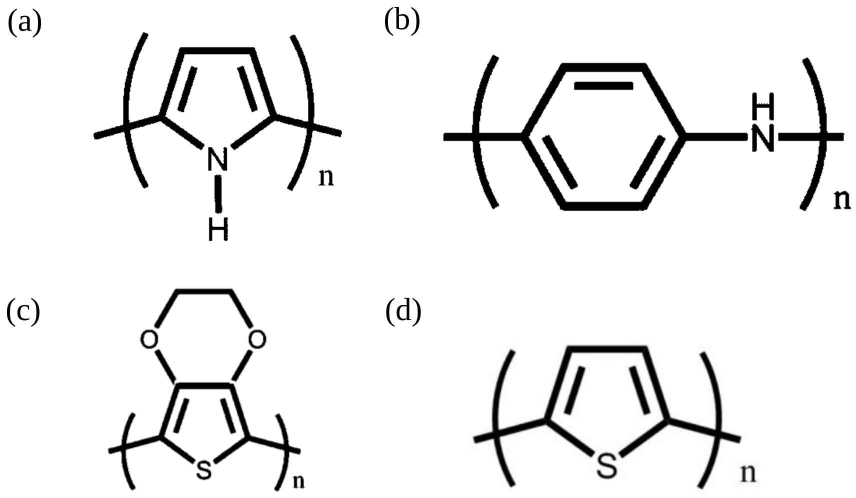

Figure 1.17. Structures of common CPs used for electrode materials. (a) polypyrrole (PPy), (b) polyaniline (PANI), (c) (ethylenedioxythiophene) (PEDOT), and (d) polythiophene (PTh).

However, several drawbacks such as the poor cycle-life and the low cycling stability restrict the performance of CPs as electrode materials.[94] The volume change during the redox reactions causes the structural degradation and eventually failure of the electrodes. Besides the redox reaction that is used to store charges, some side reactions can inevitably happen at the same time, which slowly deteriorates the electrode performance. As a result, CPs are often supported on porous rigid materials such as porous carbons and the CNTs.

1.5.3. Transition metal oxides

The transition metal oxides, such as ruthenium oxides, manganese oxides, vanadium pentoxide, nickel oxides, cobalt oxides, belong to another category of electrode materials with high pseudocapacitance. The transition metals have a variety of oxidation states that are electrical conducting or semiconducting. The metal oxides or hydroxides can undergo a series of continuous redox reaction to switch among these states, which causes a large pseudocapacitance. The reported value of specific capacitance for the transition metal electrodes can reach up to 1100 F/g.[95] As a comparison, the capacitance of ACs-based materials is only around 200 F/g. Because of many oxidation states that transition metal oxides have, the CV curves of transition metal electrodes usually show a quasi-rectangle shapes without any major peaks, which are different from the CV curves of electrodes based on the conducting polymers with obvious oxidation peaks and reduction peaks.

The main advantage of the transition metal electrodes is their high theoretical capacitance. For example, NiO shows a high theoretical capacitance value of 2573 F/g.[96] However, the main disadvantage of transition metal electrodes is their poor electrical conductivity. Many methods have been developed to compensate for the poor electrical conductivity of the transition metal oxides. The transition metal oxide can be deposited on the surface of a supporting skeleton with high surface area and good electronically conductivity, which can effectively increase the electrochemical performance. Conductive additives such as graphene and the CNTs can also be used to produce composites so that the electrodes can have both high capacitance and high electrical conductivity.

To sum up, the capacitance of SCs is produced through many different ways including the double-layers formed on the surface of electrodes, the reversible adsorption of electrolyte ions on the electrodes, the reversible doping process of conducting polymers and the redox reactions of transition metal oxides. The structure of SCs can be symmetrical or asymmetrical. The electrolytes can be chosen from aqueous or organic solutions, ion liquids or solid-state gels, etc. Different electrode materials are available with their distinctive advantages and drawbacks. The design of SCs must take all the factors into consideration and ensure that the components are compatible with each other so that the advantages of each component can be fully exploited and the performance of the device can be optimized.

1.6. Recent developments in carbon materials

Previous research show that ACs can be produced from various fossil-based hydrocarbons (e.g. coal and lignite[97, 98]) and biomass[99] (i.e. lignocellulosic materials[100]). At present coal is still the dominant raw material despite the environmental damages associated with its production and utilization.[101] This raw material, however, is not a sustainable material source for the production of ACs. Biomass, on the other hand, has been gaining popularity because of its distinctive advantages such as abundance and renewability. Various types of biomass have been used to produce ACs, including rice husks[102], coconut husks,[103] cotton stalks[104], and most recently distiller's dried grains with solubles (DDGS).[105, 106]

A novel biomass produced by bacterial, bacterial cellulose, has recently been explored for the application as electrode materials. Bacterial cellulose (BC) is chemically identical with the cellulose in the cell walls of plants, but in contrast with the plant-derived cellulose which is heterogeneous and difficult to purity and utilize, BC is free from lignin, hemicellulose and other biopolymers that exist in the cell walls.[107] Besides its purity, BC also has many distinctive properties such as high crystallinity[108], high mechanical strength[109], high water holding capacity[110] and outstanding biocompatibility[111]. BC has a unique three-dimensional (3D) network structure formed by the ultrafine cellulose fibers, which can be used to produce 3D ultra-lightweight aerogels.[112] The excellent biocompatibility of BC makes it ideal for the biomedical applications such as skin tissue repair. Besides, the commercialization of BC for application in drug delivery systems shows promising future.[113, 114] In the field of nanomaterials, it has been reported that highly conductive and flexible carbon aerogels (CA) can be produced from lyophilized BC aerogels by the pyrolysis in inert atmosphere such as argon or nitrogen.[115] BC has been used in the field of energy storages in recent years. For example, BC was employed as the template and substrate to support the electro-active materials.[116-119] The composites have unique flexible mechanical properties with good bending stability, and show high electrochemical performance with specific capacitances up to ~500 F/g and energy densities up to ~30 Wh/kg. Recently, BC-based gel electrolyte has also been developed to fabricate all-biomaterial derived SCs.[120] Nitrogen-doped electrode materials from the pyrolyzed BC are synthesized by the hydrothermal reaction between BC and aqueous ammonia solution or by the annealing of BC in NH_3 atmosphere.[121, 122] Despite these advances, the application of BC for energy storage devices still needs to be studied further.

Traditional carbonization and activation of biomass require high temperature (1000~2000℃). Recently, the microwave irradiation has been reported to be an effective and efficient method to produce carbonaceous and related materials with various hierarchical 3D structures.[123] For this method to work, microwave absorbing materials such as graphene oxide (GO) need to be present in the precursors to generate required high heat.[80] The electrodes prepared using microwave-induced graphene layers show high specific capacitance and outstanding cycling performance.[124, 125] The high temperature generated by microwave irradiation promotes the growth of graphitic carbon and increases the electrical conductivity of the obtained carbonaceous materials, which can reduce the equivalent series resistance (ESR) of an energy storage device and increase its electrochemical performance.

Hydrothermal carbonization (HTC) is another energy efficient carbonization method that is especially useful for the biomass carbonization. Traditional carbonization methods such as pyrolysis can convert dry biomass into charcoal, liquid or gaseous products at high temperatures (1000~2000 °C).[126] HTC, on the contrary, involves treatment of biomass in a pressurized, aqueous environment at a mild temperature (160~250 °C).[127] The process lowers both oxygen and hydrogen contents of the biomass through an array of reactions including hydrolysis, dehydration, decarboxylation, polymerization and aromatization.[128, 129] The products from this process are carbon-rich lignite-like solid hydrochar and water-soluble chemicals including sugar- and lignin-derived compounds.[130-132] This method can treat wet or green biomass directly and consumes less energy compared with the conventional high temperature carbonization methods. HTC is an energy efficient method to convert wet biomass for energy and chemicals,[133] and it uses water as the medium. Therefore, HTC is considered an environmentally benign and inexpensive path to develop high value applications of biomass. HTC has been used to produce functional carbon materials with hierarchical porous structures. For example, it has been reported that aqueous glucose solutions can transform into porous carbon spheres at relatively mild temperature (~160 °C) under 6~7 atm pressure due to the dehydration effect that occurs during the hydrothermal process.[134] Fluorescent carbon nanoparticles were successfully developed from chitosan using HTC, which had the potential to be used in large-scale production.[135] Carbonaceous aerogels were prepared by a one-step HTC method, and the aerogels were used as scaffolds for Fe_3O_4 nanoparticle growth. The composites exhibited excellent electrochemical performance after calcination.[136] In searching for producing bio-based carbonaceous nanomaterials using a green method, carbonization of DDGS using HTC represents a promising route.

1.7. Research needs and research goal

Due to its low-cost, renewability, and high commercial availability in the Midwest of the US, DDGS is an ideal biomass for the production of ACs. Although the preparation of ACs from DDGS has been reported in three prior studies, traditional pyrolysis method were used in these studies.[137] No in-depth investigation on carbon crystalline structure/conductivity vs pyrolysis conditions were performed and no attempts to increase the capacitance of the ACs through incorporating pseudocapacitance were made. In terms of BC, although it has been made into carbon aerogels and used for energy storage devices, new methods for nanofiber surface modification to increase the capacitance is still necessary.

The main goal of the dissertation is to develop facile, energy efficient processes to produce bio-based carbon nanomaterials that have high energy storage performance. HTC and microwave irradiation will be used as the energy efficient carbonization methods. DDGS and BC will be chosen as the representative biomass feedstock. Deposition of electrochemically active materials on the carbon nanomaterials for additional pseudocapacitance will be explored. The applications of the obtained carbon nanomaterials in supercapacitors will be demonstrated.

1.8. Organization of the dissertation

The first chapter provides a thorough literature review on energy storage devices and the materials for electrode of supercapacitors. The fundamentals of energy storage are discussed in detail, and different kinds of electrode materials are introduced to compare their properties and their performances.

In chapter 2, a one-step, facile method to produce 3D ACs from DDGS by microwave-assisted chemical activation was presented. The ACs' application potentials in dye removal and supercapacitor electrodes were demonstrated. The porous structure and surface properties of the ACs were characterized by N_2 adsorption/desorption isotherms and scanning electron microscopy. The results showed that the surface area of the as-prepared ACs was up to 1000 m^2/g. In the dye removal tests, these DDGS-based ACs exhibited a maximum adsorption ratio of 477 mg/g using methylene blue as an example. In electric double layer capacitors, electrochemical tests indicated that the ACs had ideal capacitive and reversible behaviors and exhibited excellent electrochemical performance. The specific capacitance varied between 120 and 210 F/g under different scan rates and current densities. In addition, the capacitors showed excellent stability even after one thousand charge–discharge cycles. The specific capacitance was further increased up to 300 F/g by in situ synthesis of MnO_2 particles in the ACs to induce pseudo-capacitance. This research showed that the DDGS-based ACs had great potentials in environmental remediation and energy storage applications.

In chapter 3, a facile, energy-efficient process for producing highly graphitized ACs using DDGS as the feedstock is discussed. The three-step process included hydrothermal carbonization (HTC), KOH activation, and a short burst of direct microwave irradiation. It was found that the presence of a small amount of graphene oxide (GO) in DDGS could significantly change the morphology of the produced carbon (from spherical particles to flakes) and increase the degree of carbonization and graphitization of the biomass. The ACs produced with and without GO were made into supercapacitor electrodes, and their electrochemical properties were compared. This study proves that GO-assisted HTC and direct microwave irradiation is an effective method for biomass carbonization, and the AC produced using this method is a promising electrode material for supercapacitors.

Chapters 4 and 5 focus on the development of pseudocapacitors by the electrodeposition technique. In chapter 4, a facile method to create a polyaniline (PANI) nanorod/carbon nanoparticle (CNP) composite structure that is suitable for supercapacitor use is introduced. A network of CNPs was conveniently produced on the surface of a nickel foam by collecting the candle soot above a burning candle. The PANI nanorods were then electrochemically deposited on the CNP network, forming a star-like interconnected 3D structure. As a comparison, MnO_2 particles were also deposited on the CNP network to produce a broccoli-like structure. The electrochemical properties of these two composites were examined using cyclic voltammetry, cyclic charge-discharge, and electrochemical impedance spectroscopy. The two electrodes exhibited different electrochemical behaviors: high capacitance at low current densities and marked deterioration at high ones for CNPs/PANI and relatively low but stable capacitance for CNPs/MnO_2. The reasons for this distinction were discussed based on the structures and material properties of the electrodes.

In chapter 5, bacterial cellulose (BC) was used as the raw material to produce freestanding carbon aerogel (CA). The CA developed from BC was further decorated with MnO_2/$Ni(OH)_2$ hybrid via electrodeposition and redox reaction. The application of this novel material as electrodes of supercapacitors was explored. The as-prepared composite used CA as the scaffold, and the MnO_2/$Ni(OH)_2$ hybrid formed by MnO_2 and $Ni(OH)_2$ nanoparticles served as the active materials to promote high electrochemical performance. The electrochemical performance was examined in 1 M Na_2SO_4 electrolyte. The results showed that a specific capacitance of 109 F/g was achieved at the current density of 1 A/g. The electrode could deliver an energy density of 9.4 Wh/kg and a power density of 4000W/kg. These results demonstrated the potential application of BC for electrode materials of energy storage devices. This study provides a bio-based, low-cost and renewable material source for the fabrication of electrodes in energy storage devices.

1.9. References

1. White, D.; Roschelle, A.; Peterson, P.; Schlissel, D.; Biewald, B.; Steinhurst, W. *The Electricity Journal* **2003,** 16, (9), 43-53.

2. Deane, P. M., *The first industrial revolution*. Cambridge University Press: 1979.

3. Mokyr, J. *Storia dell'economia Mondiale* **1998**, 219-45.

4. Ashton, T. S. *OUP Catalogue* **1997**.

5. Freese, B., *Coal: A human history*. Basic Books: 2016.

6. Kaldellis, J. K.; Zafirakis, D. *Renewable Energy* **2011,** 36, (7), 1887-1901.

7. Shafiee, S.; Topal, E. *Energy Policy* **2009,** 37, (1), 181-189.

8. Dyni, J. R. *Oil shale* **2003,** 20, (3), 193-253.

9. Goldemberg, J. *Science* **2007,** 315, (5813), 808-810.

10. Obama, B. *Science* **2017**.

11. Stocker, T., *Climate change 2013: the physical science basis: Working Group I contribution to the Fifth assessment report of the Intergovernmental Panel on Climate Change*. Cambridge University Press: 2014.

12. Rodhe, H. *Science* **1990,** 248, (4960), 1217.

13. Höök, M.; Tang, X. *Energy Policy* **2013,** 52, 797-809.

14. Meinshausen, M.; Meinshausen, N.; Hare, W.; Raper, S. C. B.; Frieler, K.; Knutti, R.; Frame, D. J.; Allen, M. R. *Nature* **2009,** 458, (7242), 1158-1162.

15. Hoel, M.; Kverndokk, S. *Resource and Energy Economics* **1996,** 18, (2), 115-136.

16. Griffiths, S. *Energy Policy* **2017,** 102, 249-269.

17. Mohr, S. H.; Wang, J.; Ellem, G.; Ward, J.; Giurco, D. *Fuel* **2015,** 141, 120-135.

18. Dresselhaus, M.; Thomas, I. *Nature* **2001,** 414, (6861), 332-337.

19. Dunn, B.; Kamath, H.; Tarascon, J.-M. *Science* **2011,** 334, (6058), 928-935.

20. Evans, A.; Strezov, V.; Evans, T. J. *Renewable and Sustainable Energy Reviews* **2012,** 16, (6), 4141-4147.

21. Connolly, D.; Lund, H.; Mathiesen, B. *Renewable and Sustainable Energy Reviews* **2016,** 60, 1634-1653.

22. Panwar, N. L.; Kaushik, S. C.; Kothari, S. *Renewable and Sustainable Energy Reviews* **2011,** 15, (3), 1513-1524.

23. Kralova, I.; Sjöblom, J. *Journal of Dispersion Science and Technology* **2010,** 31, (3), 409-425.

24. Doner, J. *Institute for Regulatory Policy Studies, Illinois State University, Working Paper* **2007**.

25. Islam, M. R.; Mekhilef, S.; Saidur, R. *Renewable and Sustainable Energy Reviews* **2013,** 21, 456-468.

26. Turner, J. A. *Science* **1999,** 285, (5428), 687-689.

27. Kaldellis, J. K.; Zafirakis, D. *Energy* **2007,** 32, (12), 2295-2305.

28. Keyhani, A., *Design of smart power grid renewable energy systems*. John Wiley & Sons: 2016.

29. Chen, C.; Duan, S.; Cai, T.; Liu, B.; Hu, G. *IET renewable power generation* **2011,** 5, (3), 258-267.

30. Chemali, E.; Preindl, M.; Malysz, P.; Emadi, A. *IEEE Journal of Emerging and Selected Topics in Power Electronics* **2016,** 4, (3), 1117-1134.

31. Calabrese, G., *The greening of the automotive industry*. Springer: 2016.

32. Chalamala, B. R. *Proceedings of the IEEE* **2007,** 95, (11), 2106-2107.

33. Winter, M.; Brodd, R. J. *Chemical Reviews* **2004,** 104, (10), 4245-4270.

34. Kötz, R.; Carlen, M. *Electrochimica Acta* **2000,** 45, (15–16), 2483-2498.

35. Simon, P.; Gogotsi, Y.; Dunn, B. *Science* **2014,** 343, (6176), 1210-1211.

36. He, Y.; Chen, W.; Gao, C.; Zhou, J.; Li, X.; Xie, E. *Nanoscale* **2013,** 5, (19), 8799-8820.

37. Becker, H. I., Low voltage electrolytic capacitor. In Google Patents: 1957.

38. Boos, D. L., Electrolytic capacitor having carbon paste electrodes. In Google Patents: 1970.

39. Rightmire, R. A., Electrical energy storage apparatus. In Google Patents: 1966.

40. Snook, G. A.; Kao, P.; Best, A. S. *Journal of Power Sources* **2011,** 196, (1), 1-12.

41. Sharma, P.; Bhatti, T. S. *Energy Conversion and Management* **2010,** 51, (12), 2901-2912.

42. Devillers, N.; Jemei, S.; Péra, M.-C.; Bienaimé, D.; Gustin, F. *Journal of Power Sources* **2014,** 246, 596-608.

43. Evarts, E. C. *Nature* **2015,** 526, (7575), S93-S95.

44. O'hayre, R.; Cha, S.-W.; Prinz, F. B.; Colella, W., *Fuel cell fundamentals*. John Wiley & Sons: 2016.

45. Steele, B. C. H.; Heinzel, A. *Nature* **2001,** 414, (6861), 345-352.

46. Lamy, C.; Rousseau, S.; Belgsir, E. M.; Coutanceau, C.; Léger, J. M. *Electrochimica Acta* **2004,** 49, (22–23), 3901-3908.

47. Sharaf, O. Z.; Orhan, M. F. *Renewable and Sustainable Energy Reviews* **2014,** 32, 810-853.

48. Yu, H.; Tang, Q.; Wu, J.; Lin, Y.; Fan, L.; Huang, M.; Lin, J.; Li, Y.; Yu, F. *Journal of Power Sources* **2012,** 206, 463-468.

49. Karabelli, D.; Leprêtre, J. C.; Alloin, F.; Sanchez, J. Y. *Electrochimica Acta* **2011,** 57, 98-103.

50. Lee, Y. M.; Kim, J.-W.; Choi, N.-S.; Lee, J. A.; Seol, W.-H.; Park, J.-K. *Journal of Power Sources* **2005,** 139, (1–2), 235-241.

51. Obreja, V. V. N. *Physica E: Low-dimensional Systems and Nanostructures* **2008,** 40, (7), 2596-2605.

52. Chen, W.; He, Y.; Li, X.; Zhou, J.; Zhang, Z.; Zhao, C.; Gong, C.; Li, S.; Pan, X.; Xie, E. *Nanoscale* **2013,** 5, (23), 11733-11741.

53. Zhang, J.; Jiang, J.; Li, H.; Zhao, X. *Energy & Environmental Science* **2011,** 4, (10), 4009-4015.

54. Liu, Y. Fabrication of composite electrodes and supercapacitor devices. McMaster University, 2016.

55. Zhong, C.; Deng, Y.; Hu, W.; Qiao, J.; Zhang, L.; Zhang, J. *Chemical Society Reviews* **2015,** 44, (21), 7484-7539.

56. Balducci, A.; Dugas, R.; Taberna, P. L.; Simon, P.; Plée, D.; Mastragostino, M.; Passerini, S. *Journal of Power Sources* **2007,** 165, (2), 922-927.

57. Armand, M.; Endres, F.; MacFarlane, D. R.; Ohno, H.; Scrosati, B. *Nature materials* **2009,** 8, (8), 621-629.

58. Lewandowski, A.; Olejniczak, A.; Galinski, M.; Stepniak, I. *Journal of Power Sources* **2010,** 195, (17), 5814-5819.

59. Meng, C.; Liu, C.; Chen, L.; Hu, C.; Fan, S. *Nano Letters* **2010,** 10, (10), 4025-4031.

60. Kang, Y. J.; Chung, H.; Han, C.-H.; Kim, W. *Nanotechnology* **2012,** 23, (6), 065401.

61. Endo, M.; Takeda, T.; Kim, Y.; Koshiba, K.; Ishii, K. *Carbon science* **2001,** 1, (3&4), 117-128.

62. Helmholtz, H. v. *Annalen der Physik* **1853,** 165, (6), 211-233.

63. Chapman, D. L. *The London, Edinburgh, and Dublin philosophical magazine and journal of science* **1913,** 25, (148), 475-481.

64. Stern, O. *Z. Elektrochem* **1924,** 30, (508), 1014-1020.

65. Zhang, L. L.; Zhao, X. *Chemical Society Reviews* **2009,** 38, (9), 2520-2531.

66. Bockris, J. M.; Devanathan, M.; Muller, K. In *On the structure of charged interfaces*, Proceedings of the Royal Society of London A: Mathematical, Physical and Engineering Sciences, 1963; The Royal Society: 1963; pp 55-79.

67. Namisnyk, A. M. A survey of electrochemical supercapacitor technology. University of Technology, Sydney, 2003.

68. Lee, K. Y. T. Study of Flexible Multi-wall Carbon Nano-tubes/Conductivepolymer Composites for Supercapacitor Applications. University of Toronto, 2014.

69. Zhang, B.-T.; Zheng, X.; Li, H.-F.; Lin, J.-M. *Analytica Chimica Acta* **2013,** 784, 1-17.

70. Geim, A. K.; Novoselov, K. S. *Nat Mater* **2007,** 6, (3), 183-191.

71. Prenzel, D.; Tykwinski, R. R., New Synthetic Carbon Allotropes. In *Encyclopedia of Polymeric Nanomaterials*, Springer: 2015; pp 1382-1392.

72. Behabtu, N.; Young, C. C.; Tsentalovich, D. E.; Kleinerman, O.; Wang, X.; Ma, A. W.; Bengio, E. A.; ter Waarbeek, R. F.; de Jong, J. J.; Hoogerwerf, R. E. *Science* **2013,** 339, (6116), 182-186.

73. Wen, M.; Sun, X.; Su, L.; Shen, J.; Li, J.; Guo, S. *Polymer* **2012,** 53, (7), 1602-1610.

74. Leimkuehler, E. P. Production, characterization, and applications of activated carbon. University of Missouri--Columbia, 2010.

75. Wang, Y.; Zhou, J.; Jiang, L.; Ulven, C.; Lubineau, G.; Liu, G.; Xiao, J. *J Polym Environ* **2015,** 23, (4), 595-605.

76. Ioannidou, O.; Zabaniotou, A. *Renewable and Sustainable Energy Reviews* **2007,** 11, (9), 1966-2005.

77. Bouchelta, C.; Medjram, M. S.; Bertrand, O.; Bellat, J.-P. *Journal of Analytical and Applied Pyrolysis* **2008,** 82, (1), 70-77.

78. Zhong, Z.-Y.; Yang, Q.; Li, X.-M.; Luo, K.; Liu, Y.; Zeng, G.-M. *Industrial Crops and Products* **2012,** 37, (1), 178-185.

79. Abioye, A. M.; Ani, F. N. *Renewable and Sustainable Energy Reviews* **2015,** 52, 1282-1293.

80. Singh, R. K.; Kumar, R.; Singh, D. P. *RSC Advances* **2016,** 6, (69), 64993-65011.

81. Lee, C.; Wei, X.; Kysar, J. W.; Hone, J. *Science* **2008,** 321, (5887), 385-388.

82. Chen, S.; Wu, Q.; Mishra, C.; Kang, J.; Zhang, H.; Cho, K.; Cai, W.; Balandin, A. A.; Ruoff, R. S. *Nature materials* **2012,** 11, (3), 203-207.

83. Kim, H.; Abdala, A. A.; Macosko, C. W. *Macromolecules* **2010,** 43, (16), 6515-6530.

84. Hummers, W. S.; Offeman, R. E. *Journal of the American Chemical Society* **1958,** 80, (6), 1339-1339.

85. Stoller, M. D.; Park, S.; Zhu, Y.; An, J.; Ruoff, R. S. *Nano Letters* **2008,** 8, (10), 3498-3502.

86. Thostenson, E. T.; Ren, Z.; Chou, T.-W. *Composites Science and Technology* **2001,** 61, (13), 1899-1912.

87. Baughman, R. H.; Zakhidov, A. A.; de Heer, W. A. *Science* **2002,** 297, (5582), 787-792.

88. Kim, Y. J.; Horie, Y.; Ozaki, S.; Matsuzawa, Y.; Suezaki, H.; Kim, C.; Miyashita, N.; Endo, M. *Carbon* **2004,** 42, (8–9), 1491-1500.

89. Hwang, S.-W.; Hyun, S.-H. *Journal of Non-Crystalline Solids* **2004,** 347, (1–3), 238-245.

90. Basnayaka, P. A., *Development of Nanostructured Graphene/Conducting Polymer Composite Materials for Supercapacitor Applications*. University of South Florida: 2013.

91. Wu, Z.-Y.; Li, C.; Liang, H.-W.; Chen, J.-F.; Yu, S.-H. *Angewandte Chemie* **2013,** 125, (10), 2997-3001.

92. Janata, J.; Josowicz, M. *Nature materials* **2003,** 2, (1), 19-24.

93. Chiang, C. K.; Fincher Jr, C.; Park, Y. W.; Heeger, A. J.; Shirakawa, H.; Louis, E. J.; Gau, S. C.; MacDiarmid, A. G. *Physical Review Letters* **1977,** 39, (17), 1098.

94. Wang, Y.; Jiang, L.; Wang, Y. *Electrochimica Acta* **2016,** 210, 190-198.

95. Lokhande, C. D.; Dubal, D. P.; Joo, O.-S. *Current Applied Physics* **2011,** 11, (3), 255-270.

96. Faraji, S.; Ani, F. N. *Journal of Power Sources* **2014,** 263, 338-360.

97. Maldhure, A. V.; Ekhe, J. D. *Chemical Engineering Journal* **2011,** 168, (3), 1103-1111.

98. Yagmur, E.; Tunc, M. S.; Banford, A.; Aktas, Z. *Journal of Analytical and Applied Pyrolysis* **2013,** 104, (0), 470-478.

99. Foo, K. Y.; Hameed, B. H. *Bioresource Technology* **2011,** 102, (20), 9794-9799.

100. Foo, K. Y.; Hameed, B. H. *Chemical Engineering Journal* **2011,** 166, (2), 792-795.

101. Zhao, X.-Y.; Huang, S.-S.; Cao, J.-P.; Xi, S.-C.; Wei, X.-Y.; Kamamoto, J.; Takarada, T. *Journal of Analytical and Applied Pyrolysis* **2014,** 105, (0), 116-121.

102. Guo, Y.; Zhao, J.; Zhang, H.; Yang, S.; Qi, J.; Wang, Z.; Xu, H. *Dyes and Pigments* **2005,** 66, (2), 123-128.

103. Tan, I. A. W.; Ahmad, A. L.; Hameed, B. H. *Chemical Engineering Journal* **2008,** 137, (3), 462-470.

104. Deng, H.; Zhang, G.; Xu, X.; Tao, G.; Dai, J. *Journal of Hazardous Materials* **2010,** 182, (1–3), 217-224.

105. Jin, H.; Wang, X.; Gu, Z. *Materials Focus* **2013,** 2, (6), 497-501.

106. Hong, J.; Xiaomin, W.; Zhengrong, G. *Materials Focus* **2013,** 2, (2), 105-112.

107. Zhu, H.; Luo, W.; Ciesielski, P. N.; Fang, Z.; Zhu, J. Y.; Henriksson, G.; Himmel, M. E.; Hu, L. *Chemical Reviews* **2016,** 116, (16), 9305-9374.

108. Iguchi, M.; Yamanaka, S.; Budhiono, A. *Journal of Materials Science* **2000,** 35, (2), 261-270.

109. Yamanaka, S.; Watanabe, K.; Kitamura, N.; Iguchi, M.; Mitsuhashi, S.; Nishi, Y.; Uryu, M. *Journal of Materials Science* **1989,** 24, (9), 3141-3145.

110. Ul-Islam, M.; Khan, T.; Park, J. K. *Carbohydrate Polymers* **2012,** 88, (2), 596-603.

111. Helenius, G.; Bäckdahl, H.; Bodin, A.; Nannmark, U.; Gatenholm, P.; Risberg, B. *Journal of Biomedical Materials Research Part A* **2006,** 76A, (2), 431-438.

112. Liebner, F.; Haimer, E.; Wendland, M.; Neouze, M.-A.; Schlufter, K.; Miethe, P.; Heinze, T.; Potthast, A.; Rosenau, T. *Macromolecular Bioscience* **2010,** 10, (4), 349-352.

113. Almeida, I. F.; Pereira, T.; Silva, N. H. C. S.; Gomes, F. P.; Silvestre, A. J. D.; Freire, C. S. R.; Sousa Lobo, J. M.; Costa, P. C. *European Journal of Pharmaceutics and Biopharmaceutics* **2014,** 86, (3), 332-336.

114. Fu, L.; Zhang, J.; Yang, G. *Carbohydrate Polymers* **2013,** 92, (2), 1432-1442.

115. Chen, L.-F.; Huang, Z.-H.; Liang, H.-W.; Guan, Q.-F.; Yu, S.-H. *Advanced Materials* **2013,** 25, (34), 4746-4752.

116. Xu, J.; Zhu, L.; Bai, Z.; Liang, G.; Liu, L.; Fang, D.; Xu, W. *Organic Electronics* **2013,** 14, (12), 3331-3338.

117. Li, S.; Huang, D.; Zhang, B.; Xu, X.; Wang, M.; Yang, G.; Shen, Y. *Advanced Energy Materials* **2014,** 4, (10), n/a-n/a.

118. Liu, Y.; Zhou, J.; Tang, J.; Tang, W. *Chemistry of Materials* **2015,** 27, (20), 7034-7041.

119. Wang, F.; Kim, H.-J.; Park, S.; Kee, C.-D.; Kim, S.-J.; Oh, I.-K. *Composites Science and Technology* **2016,** 128, 33-40.

120. Wang, X.; Kong, D.; Zhang, Y.; Wang, B.; Li, X.; Qiu, T.; Song, Q.; Ning, J.; Song, Y.; Zhi, L. *Nanoscale* **2016,** 8, (17), 9146-9150.

121. Chen, P.; Xiao, T.-Y.; Qian, Y.-H.; Li, S.-S.; Yu, S.-H. *Advanced Materials* **2013,** 25, (23), 3192-3196.

122. Chen, L.-F.; Huang, Z.-H.; Liang, H.-W.; Yao, W.-T.; Yu, Z.-Y.; Yu, S.-H. *Energy & Environmental Science* **2013,** 6, (11), 3331-3338.

123. Kumar, R.; Singh, R. K.; Dubey, P. K.; Singh, D. P.; Yadav, R. M. *ACS Applied Materials & Interfaces* **2015,** 7, (27), 15042-15051.

124. Kumar, R.; Singh, R. K.; Savu, R.; Dubey, P. K.; Kumar, P.; Moshkalev, S. A. *RSC Advances* **2016,** 6, (32), 26612-26620.

125. Kumar, R.; Kim, H.-J.; Park, S.; Srivastava, A.; Oh, I.-K. *Carbon* **2014,** 79, 192-202.

126. Demirbaş, A. *Energy Conversion and Management* **2001,** 42, (10), 1229-1238.

127. Tekin, K.; Karagöz, S.; Bektaş, S. *Renewable and Sustainable Energy Reviews* **2014,** 40, 673-687.

128. Funke, A.; Ziegler, F. *Biofuels, Bioproducts and Biorefining* **2010,** 4, (2), 160-177.

129. Hoekman, S. K.; Broch, A.; Robbins, C. *Energy & Fuels* **2011,** 25, (4), 1802-1810.

130. Mäkelä, M.; Benavente, V.; Fullana, A. *Applied Energy* **2015,** 155, 576-584.

131. Xiao, L.-P.; Shi, Z.-J.; Xu, F.; Sun, R.-C. *Bioresource Technology* **2012,** 118, 619-623.

132. Burguete, P.; Corma, A.; Hitzl, M.; Modrego, R.; Ponce, E.; Renz, M. *Green Chemistry* **2016,** 18, (4), 1051-1060.

133. Zhao, P.; Shen, Y.; Ge, S.; Chen, Z.; Yoshikawa, K. *Applied Energy* **2014,** 131, 345-367.

134. Yao, C.; Shin, Y.; Wang, L.-Q.; Windisch, C. F.; Samuels, W. D.; Arey, B. W.; Wang, C.; Risen, W. M.; Exarhos, G. J. *The Journal of Physical Chemistry C* **2007,** 111, (42), 15141-15145.

135. Yang, Y.; Cui, J.; Zheng, M.; Hu, C.; Tan, S.; Xiao, Y.; Yang, Q.; Liu, Y. *Chemical Communications* **2012,** 48, (3), 380-382.

136. Wu, X.-L.; Wen, T.; Guo, H.-L.; Yang, S.; Wang, X.; Xu, A.-W. *ACS Nano* **2013,** 7, (4), 3589-3597.

137. Jin, H.; Wang, X.; Gu, Z.; Polin, J. *Journal of Power Sources* **2013,** 236, 285-292.

2. DEVELOPMENT OF ACTIVATED CARBONS FROM AGRICULTURAL RESIDUALS AND THEIR APPLICATIONS FOR ELECTRODES OF SUPERCAPACITORS AND CONTAMINANTS REMOVAL

2.1. Introduction

Dried Distillers Grains with Solubles (DDGS) is the primary by-product from dry-milled corn ethanol production. Each year the U.S. produces 14 billion gallons of corn ethanol and as a result 30 million tons of DDGS is generated.[1] DDGS typically contains about 42% fiber, 27% crude protein, 7% starch, and 0.6% phosphorus,[2] and is primarily used as an animal feed. Due to its large yield, the value of DDGS is fairly low, selling at less than 10 cents/lb. in bulk. It is therefore important to find new value-added uses for DDGS to increase the sustainability of the corn ethanol industry.

One potential use of DDGS is to produce activated carbons (ACs), which are carbonaceous materials with high specific surface area, microporous structure and various surface functional groups. ACs can be produced using different activation methods and activation agents. The specific surface area of ACs measured by Brunauer-Emmett-Teller (BET) method typically ranges from 1,000 to 2,000 m^2/g. Due to their high specific surface area, high thermal stability, relatively low cost, wide availability and strong adsorption capability, ACs have been widely used to remove heavy metals[3] and dyes[4] from liquids. Various techniques, including physical, chemical and biological methods, and their combinations, have been investigated for color removal from dye-laden wastewater.[5] Among these techniques, the physical adsorption by ACs is considered to be a simple, low-cost and effective method.[6]

Another important use of ACs is to make electrodes for energy storage devices such as batteries and capacitors. EDLCs are widely recognized as an alternative to batteries with the advantages of high power density, large capacity, relatively low leakage current, long cycle life and simple charge-discharge mechanisms.[7] As a result, EDLCs have played an increasingly important role in energy storage applications. The electrodes in an EDLC show significant effects on the electrochemical properties of the supercapacitor.[8] The ideal electrode material should possess large specific surface area, optimum pore size and size distribution, high electric conductivity, high chemical and thermal stability in electrolytes, and should have low-cost abundant supply.

Although ACs have been produced from different types of biomass, developing ACs from DDGS using energy-efficient microwave-induced heating has not been attempted. Microwave heating has the advantages of higher heating rate and lower energy cost. The goal of this study is to study the processing-property relationship of the DDGS-based ACs produced via microwave heating and phosphoric acid activation. Processing parameters including the acid/DDGS ratio and heating temperature are varied and their effects on the surface area, pore size and pore size distribution of the obtained ACs are determined. Great application potentials of the DDGS-based ACs are demonstrated through dye removal tests and supercapacitor applications.

2.2. Experimental

2.2.1. Materials

DDGS from Tharaldson Ethanol Plant (Casselton, North Dakota) was ground into powder and sieved through a 0.5mm screen. The composition of DDGS was analyzed following the AOAC Official Methods.[9] The contents of neutral detergent fiber and acid detergent fiber were measured using an ANKOM Fiber Analyzer. Crude protein content was determined using a Tecator Kjeltec 1030 Autoanalyzer. Crude fat content was measured through ether extraction using a Goldfisch fat extractor. The composition analysis shows that the as-received DDGS contains about 91 wt.% dry matter, which comprises primarily fiber (~ 60 wt.%), protein (~ 30 wt.%) and fat (~ 10 wt.%). Phosphoric acid (85%, J.T. Baker) was used as the activation agent. Methylene blue (MB) (10mg/ml in water, Alfa Aesar) was used as the adsorbate to test the adsorption behavior of the produced ACs. Conductive carbon black (TIMCAL SUPER C45), polyvinylidene fluoride (PVDF) binder and N-methyl-2-pyrrolidone (NMP) were purchased from MTI Corporation. All the chemicals in this study were used without further purification.

2.2.2. Preparation and characterization of DDGS-based ACs

DDGS was first impregnated with phosphoric acid at 1/1 and 2/1 acid/DDGS weight ratios. Distilled water was then added into the mixtures to lower their viscosity to enable magnetic stirring. The ratio of DDGS to distilled water was set at 1:1 for all the samples. The stirring lasted for 1 h at 50 ℃ and homogeneous mixtures were formed at the end of the process. These precursors were then carbonized and activated using a microwave-assisted chemical activation method, in which the precursors were heat treated under different temperatures in a microwave furnace (CEM MAS 7000 Microwave Ashing Oven) for 20 minutes. After the treatment, the samples were cooled down to ambient temperature and washed with 0.5M KOH solution and distilled water consecutively till the pH of the effluent was in the range of 6.0–7.0. A constant nitrogen flow of 1000 mL/min was supplied to the furnace during the entire heating and cooling process. The final AC products were obtained by drying the washed samples at 75 °C to a constant weight, followed by grinding and sieving them through a 500 mesh. The AC products were designated by their activation temperatures and acid/DDGS ratios. For example, the AC obtained at 300°C with an acid/DDGS ratio of 2/1 was designated as AC-300-2. The surface morphology of the DDGS before and after the heat treatment was studied using SEM (JEOL JSM-6490LV). Energy-dispersive X-ray spectroscopy (EDS) was used to analyze the elements on the surface of the obtained ACs.

2.2.3. Specific surface area and pore size distribution measurements

The specific surface area, pore size and pore size distribution of the DDGS-based ACs were measured using an Accelerated Surface Area and Porosimetry System (ASAP2420, Micrometritics company) following the Brunauer−Emmett−Teller (BET) and Density functional theory (DFT) methods. Nitrogen was used as the adsorbate and the adsorption test was carried out at 77 K. Before the tests all the samples were heated to 160 °C at 10 °C/min under vacuum and kept isothermally for 240 min for degassing.

2.2.4. Adsorption tests

To investigate the ACs' ability to remove dyes from water, 100 mg of selected ACs were added into 100 mL of MB solution (300 mg/L) in 125 ml Erlenmeyer flasks and all the flasks were shaken at 200 rpm using a Water Bath Orbital shaker (Thermo Scientific MaxQ 7000) at 50 °C. The concentrations of the MB solutions after different adsorption times were determined using a UV–Vis spectrophotometer (Varian Cary 5000, Agilent Technologies) by monitoring the intensity of the absorbance peak at 665 nm wavelength. A calibration curve was first obtained by measuring the intensities of the same peak of the MB solutions with known concentrations. In order to acquire adsorption equilibrium, 100 mg AC was added into 100 ml MB solution (300 mg/L) in a flask and the flask was shaken (200 rpm at 50 °C) until the equilibrium was obtained (about 12 hours). All the experiments were carried out without pH adjustment. The weights of MB adsorbed by each gram of ACs (i.e. adsorption ratio) at equilibrium (q_e) and at time t (q_t) were calculated by the following two equations, respectively.

$$q_e = \frac{C_0 - C_e}{W} V$$

$$q_t = \frac{C_0 - C_t}{W} V$$

where C_0, C_t, and C_e are the initial MB mass concentration, the MB concentration at time t, and the MB concentration at equilibrium, respectively. V is the volume of the solution and W is the mass of the adsorbent.

2.2.5. Fabrication and electrochemical property testing of electrodes

To prepare supercapacitor electrodes using the DDGS-based ACs, the ACs, carbon black and PVDF (80:10:10 by weight) were mixed and ground thoroughly. NMP was added to the mixtures and pastes were formed after stirring. The pastes were then coated onto nickel foam current collectors, followed by drying in a vacuum oven overnight at 75 °C to remove NMP. The dried foams were pressed under a pressure of 10 MPa to ensure good electrical contacts between the ACs and the current collectors. The mass of the active materials (i.e., ACs, carbon black and PVDF) on the electrodes ranged from 5 to 12 mg.

The performance of the electrodes was analyzed at room temperature by cyclic voltammetry and chronopotentiometry tests using an electrochemical workstation (CHI 660C, CH Instruments, Inc.). A three-electrode cell was used for the tests with a platinum mesh as the counter electrode, Hg/HgO as the reference electrode, and 6M KOH as the electrolyte, respectively. The voltammetry experiments were performed at different potential scan rates (5 - 100 mV/s) between 0 and -1 V. The specific capacitances (C_{sp}) were calculated from the obtained CV curves using the following equations:[8]

$$C_{sp} = \frac{\int idu}{2wv\Delta V}$$

where i and u are the instant current and instant potential, respectively. w is the mass of the active materials on the electrodes, v is the scan rate, and ΔV is the difference in voltage at the start and the end of a scan cycle.

The energy density (De) and power density (D_p) of the electrodes were calculated based on the cyclic charge/discharge (CCD) measurements performed between 0 and -1 V at various current densities (0.25 ~ 5 A/g):

$$D_e = \frac{1}{2} C_{sp} (\Delta V)^2$$

$$D_p = \frac{D_e}{\Delta t}$$

The specific capacitance was also calculated using:

$$C_{sp} = \frac{I\Delta t}{w\Delta V}$$

where I is the charge/discharge current, Δt is the time for a full discharging process, w is the mass of the active materials on the electrodes, and ΔV is the voltage window in the CCD tests. The electrochemical impedance spectroscopy (EIS) analysis was performed using a potentiostats (Gamry instruments, Reference 600) within the 0.01 to 20K Hz frequency range under open circuit potential with a perturbation of 5 mV.

2.2.6. In-situ synthesis of MnO_2 during DDGS carbonization

DDGS and phosphoric acid were first mixed at 1:1 ratio (total weight ~ 20 g). 15 mL $KMnO_4$ solution (100 mM) was then added and the mixture was stirred for 30 minutes to form a homogenous slurry. The slurry was carbonized using a microwave oven at 600°C under continuous nitrogen flow (1 L/min) for 20 minutes. The product was washed repeatedly using distilled water and fine black power was achieved after oven drying. The powder was made into electrodes and tested by the same methods as used on the pure ACs.

2.3. Results and discussion

2.3.1. Surface morphology analysis

The optical and SEM images of the ground DDGS powder are shown in Figure 2.1a and 2.1b, respectively. The sample exhibits spherical micro-grains with relatively smooth surface. After activation, the grainy structure disappears and a new nano-porous surface is presented (Figure 2.1c). This dramatic change in structure is supposed to be caused by the oxidizing reaction with activation agents. This porous structure can provide large surface area and allow high adsorption rate.

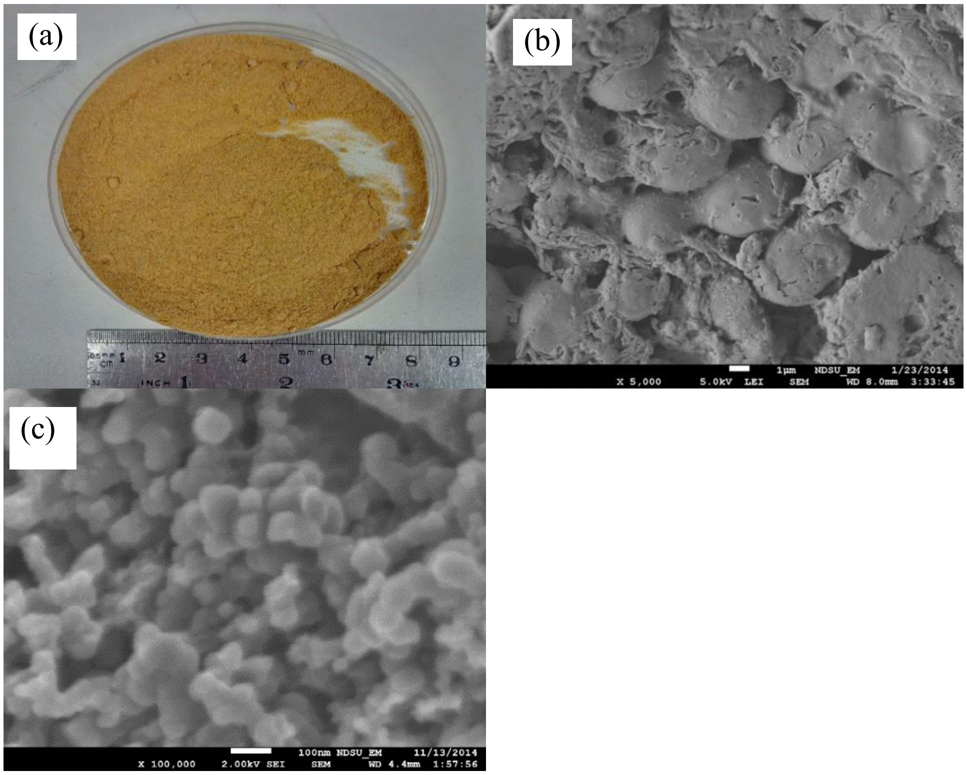

Figure 2.1. Optical (a) and SEM (b) images of the ground DDGS powder. (c) The powder after microwave-induced activation.

2.3.2. Surface area and pore size distribution

Surface area, pore size and pore size distribution of the DDGS-based ACs were calculated using Brunauer–Emmett–Teller (BET) theory and density functional theory (DFT).[10] As shown in

Table 1, the ACs exhibit a wide range of specific surface areas (217-1035 m^2/g) with the maximum value achieved under the condition of 800°C and 2:1 acid/DDGS ratio (i.e. sample AC-800-2). The results from Table 1 indicate that the development of porous structure is strongly affected by both the acid impregnation ratio and temperature. In general, high acid ratio leads to high surface area and there appears to be an optimal temperature for each acid ratio. The optimal temperature for impregnation ratio 1:1 is 500 - 600 °C, while for impregnation ratio 2:1 the largest surface area is achieved at 800 °C. This may be because with more activation agent, a higher temperature is needed for a complete reaction within the 20 min reaction time. After the reaction is completed, prolonged heating may enlarge the pores and therefore decrease the surface area. This explains the surface area decrease above 600 °C for the samples with 1:1 acid ratio. In order to study the effects of the surface area and pore size to dye adsorption and electrode capacitance, sample AC-600-1, AC-500-2 and AC-800-2 were chosen for further N_2 adsorption–desorption analysis, MB adsorption tests and electrochemical property tests. These three representative samples have a specific surface area of 571.6, 823.5 and 1035.8 m^2/g, respectively. The samples with smaller surface areas were not tested because of their expected low performance in adsorption and electrochemical tests.

Table 2.1. Surface areas of the ACs prepared under different conditions.

Sample	**Acid/DDGS ratio**	**Carbonization temperature**	**BET surface area (m^2/g)**
AC-400-1	1:1	400	221.4
AC-500-1	1:1	500	574.8
AC-600-1	1:1	600	571.6
AC-700-1	1:1	700	302.9
AC-800-1	1:1	800	217.9
AC-400-2	2:1	400	824.4
AC-500-2	2:1	500	823.5
AC-600-2	2:1	600	389.4
AC-700-2	2:1	700	893.3
AC-800-2	2:1	800	1035.8

The N_2 adsorption-desorption isotherms of the three ACs (Figure 2.2) exhibit features of both type I and type IV isotherms according to the BDDT (Brunauer-Deming-Deming-Teller) classification,[11] which suggests that the ACs contain well-developed micropores (< 2 nm) and mesopores (2–50 nm).[12] It can be observed that at extremely low pressure (P/P_0 near 0), the isotherms show drastic adoption and desorption, which is considered to be caused by the presence of ample micropores.[13] Besides, the occurrences of hysteresis loop under relatively high pressure ($0.5< P/P_0 <1$) indicate the existence of mesoporous structure.[14] The adsorption and desorption isotherms coincide at low pressure ($P/P_0 < 0.5$), suggesting that the uptake of nitrogen by the ACs materials with micropores is reversible.

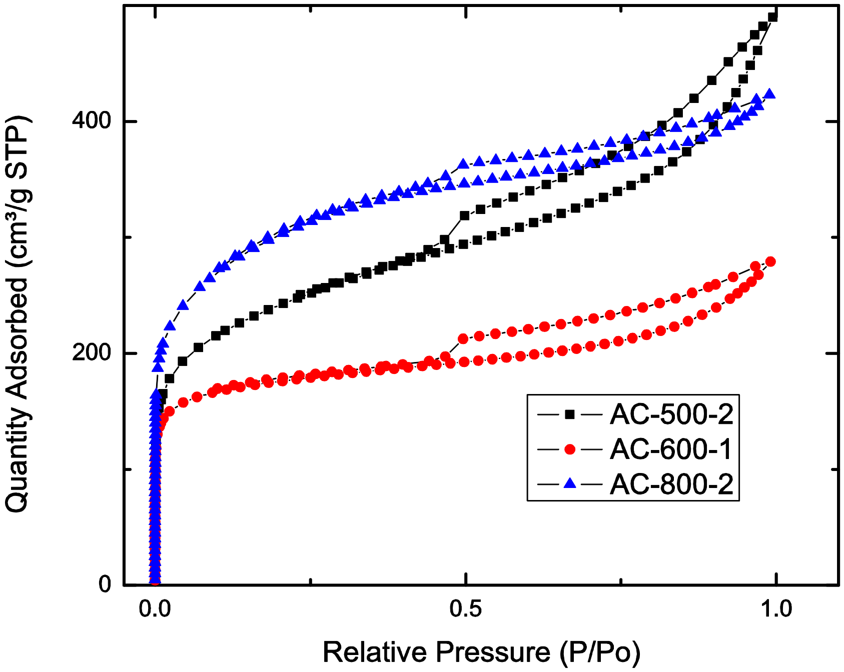

Figure 2.2. N_2 adsorption–desorption isotherms at 77 K.

The microstructures of the three ACs were further investigated using the DFT theory. The pore volume distribution determined by the DFT theory is given in Table 2.2, which indicates distinctive behaviors of the three samples. Comparing AC-800-2 with AC-500-2 (because their total pore volumes are close), the former has a much larger concentration of micropores (pores < 2 nm) and a smaller concentration of mesopores (2 nm < pores < 50 nm). Smaller pores give rise to larger surface areas when the volumes are equal, which explains AC-800-2's larger surface area. Previous research shows that micropores develop better at a higher heating rate and as a result, the micropore volume and the specific surface area increase.[15],[16] The heating rate is high in this study due to the use of microwave heating, thus facilitating the creation of micropores in general. The higher acid/DDGS ratio in AC-800-2 caused a larger scale of acid-carbon reaction during the activation process, and therefore more micropores were created.

Table 2.2. Pore volume distributions of the three ACs based on DFT analysis.

Sample	**Pore volume, volume percentage (cm^3/g, %)**				
	< 2 nm	2 – 10 nm	10 – 50 nm	> 50 nm	Total
AC-600-1	0.176	0.060	0.063	0.004	0.304
	58.2%	19.7%	20.8%	1.4%	100%
AC-500-2	0.153	0.223	0.159	0.019	0.554
	27.7%	40.2%	28.8%	3.3%	100%
AC-800-2	0.299	0.165	0.040	0.002	0.506
	58.9%	32.4%	8.1%	0.5%	100%

The pore size distribution diagrams of the three ACs are shown in Figure 2.3, which agree with the pore characteristics given by Table 2.2. It is obvious that AC-500-2 has substantially higher distribution in the mesopore region than the other two samples. This higher distribution also corresponds closely to the larger isotherm hysteresis loop of AC-500-2 (Figure 2.2). The inset of Figure 2.3 shows the distribution of the pores within the 5 nm range, which clearly indicates higher concentrations of the micropores (especially those below 1 nm) in AC-600-1 and AC-800-2. The different surface areas and pore size distributions of the three ACs are expected to cause different results in dye removal and electrochemical tests, as is discussed below.

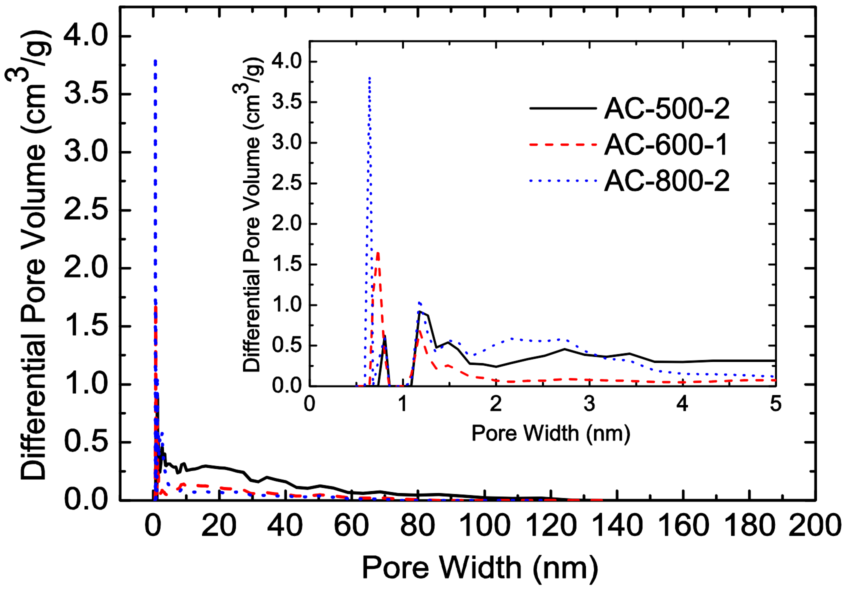

Figure 2.3. Pore size distribution from DFT analysis of the three samples. The inset shows the distribution below 5 nm.

2.3.3. MB adsorption

Figure 2.4 shows MB adsorption ratio as a function of adsorption time for the three ACs. All the samples show high-rate adsorption within the first 30 minutes, followed by second-stage low-rate adsorption and eventual equilibrium at the end of the experiments. Clearly, the adsorption capacity (i.e. the adsorption ratio at equilibrium) increases with increasing surface area of the ACs because more surface area is available for dye molecule absorption.

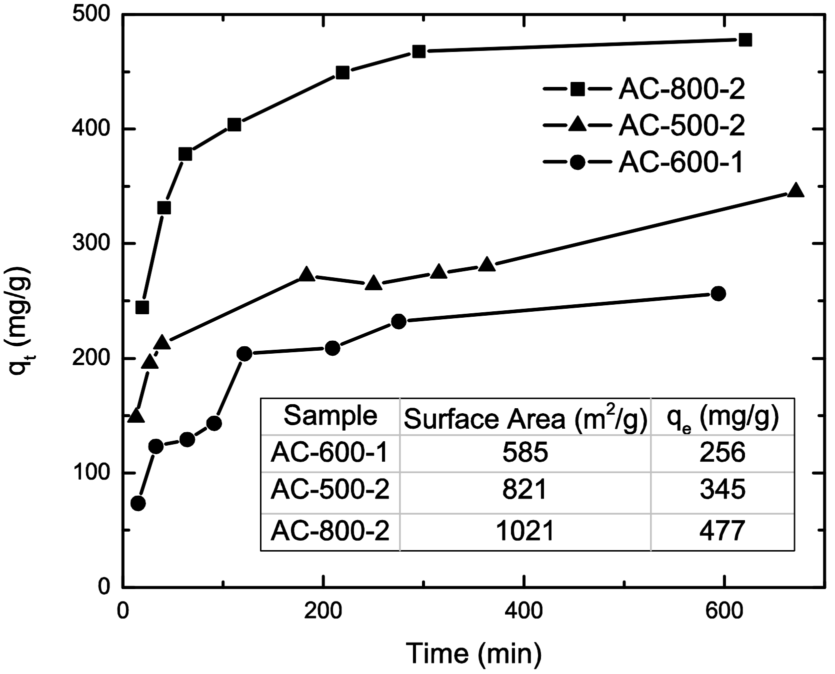

Sample	Surface Area (m^2/g)	q_e (mg/g)
AC-600-1	585	256
AC-500-2	821	345
AC-800-2	1021	477

Figure 2.4. MB adsorption as a function of time for the three ACs.

Several thermodynamic models have been used to simulate the adsorption process and they can offer important process information (e.g. equilibrium concentration) when the equilibrium is reached.[17] On the contrary, a kinetics analysis focuses on the changes in chemical properties with time as well as the rates of the changes. A pseudo-first-order kinetic model was used in this study to further understand the adsorption behavior of the ACs. In this model the mass action rate of a chemical phenomenon and the diffusion through a boundary liquid film assume the pseudo-first-order rate equation devised by Lagergren,[18]

$$\log(q_e - q_t) = log q_e - kt$$

where qe and qt are the amounts of dye adsorbed at time t and at equilibrium, respectively.[19] k is the pseudo-first-order rate constant of adsorption. As shown in Figure 2.5, the plots of $\log(q_e - q_t)$ versus time for the three ACs exhibit relatively linear relationships, and this linearity confirms that the adsorption process is governed by the first-order kinetics. Figure 2.5

demonstrates the applicability of the pseudo-first-order kinetic model and therefore it can be used to predict ACs' adsorption behavior. The $|k|$ values for the three ACs follow the order of AC-800-2 > AC-500-2 > AC-600-1, which agrees with the adsorption rate/capacity results given in Figure 2.4.

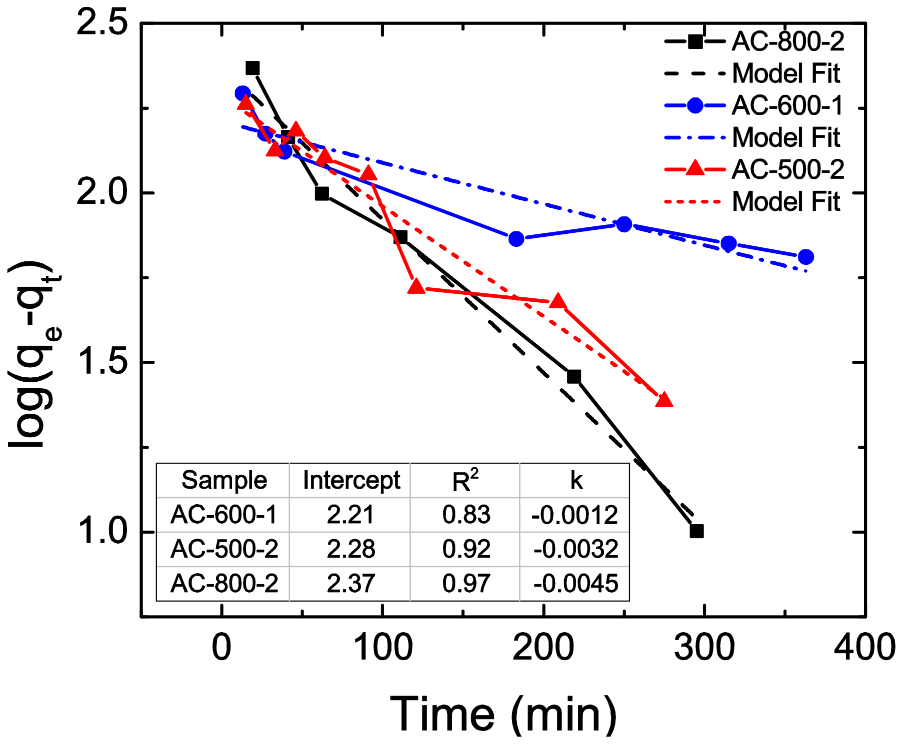

Sample	Intercept	R^2	k
AC-600-1	2.21	0.83	-0.0012
AC-500-2	2.28	0.92	-0.0032
AC-800-2	2.37	0.97	-0.0045

Figure 2.5. Pseudo-first-order kinetic model simulation for the MB adsorption of the ACs.

2.3.4. Electrochemical analysis

Figure 2.6 shows the CV plots of the electrodes made with the three ACs. The scan rate was set at 10mV/s for all the tests. The near-rectangular shape of the CV curves indicates a well-defined EDLC behavior. The table inset in Figure 2.6 shows that despite the fact that sample AC-800-2 has the largest surface area, it only exhibits a medium specific capacitance. Although large surface area is generally considered to benefit the specific capacitance, pore size and its distribution play equally, if not more, important roles in determining the capacitance (and so the energy storage capability) of an electrode. Indeed, some studies have shown that the ACs with small pore size and narrow pore size distribution tend to have reduced specific capacitance.[20] During the charge/discharge process, micropores primarily act as the ion traps for charge storage while the mesopores play dual roles: offering surface for ion adsorption and forming pathways for ion transport[21]. Both micropores and mesopores are critical in achieving large capacitance and high-energy storage. Comparing AC-800-2 with AC-500-2, the former has larger total surface area but much smaller percentage of mesopores (Table 2). This smaller percentage can lead to lack of adequate pathways for ion transport, thus hindering the charge/discharge process. As a result, the capacitance of AC-800-2 is reduced.

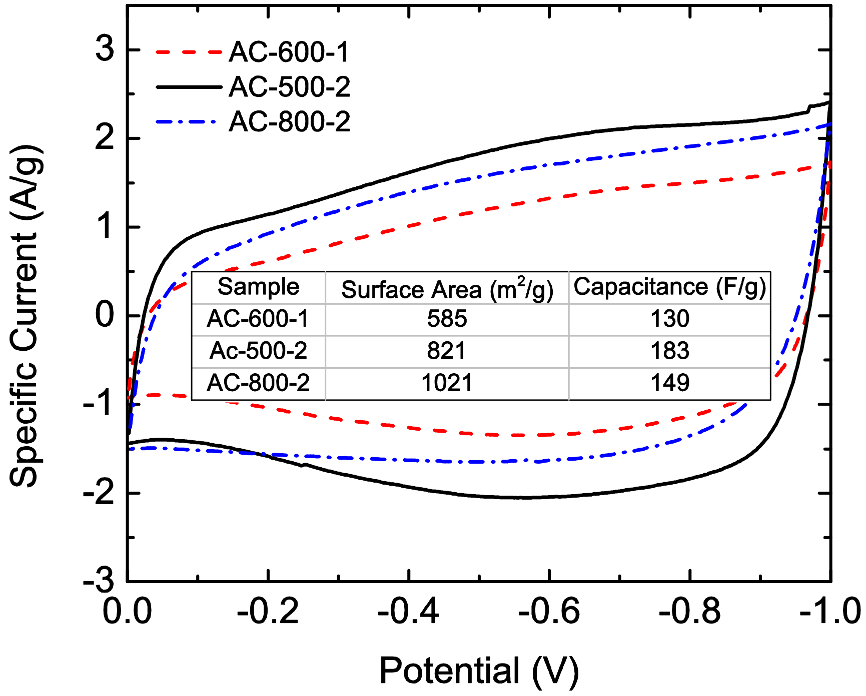

Sample	Surface Area (m^2/g)	Capacitance (F/g)
AC-600-1	585	130
Ac-500-2	821	183
AC-800-2	1021	149

Figure 2.6. CV plots of the three ACs at the scan rate 10 mV/s. The inset gives the surface area and capacitance calculated based on the plots for the three samples.

To study the electrochemical properties of the electrodes under different scan rates and current densities, AC-500-2 (the sample with the highest capacitance) was chosen for further characterization. Figure 2.7a shows its CV curves under twelve different scan rates (up to 100mV/s) in 6M KOH aqueous solutions. A quasi-rectangular shape for a CV curve indicates a perfect electrical double-layer capacitance performance with fast charge/discharge rates. The Figure 2.7a demonstrates that the curves of AC-500-2 can retain their quasi-rectangular shapes relatively well up to 50 mV/s, indicating the electrode's pure EDLC behavior and its capability to rapidly forming the double-layer even at high scan rates. The CV plots do severely deviate from their original quasi-rectangular shapes at very high scan rates (> 50 mV/s) and their corresponding capacitances decrease as a result (Figure 2.7b). The decrease is considered to be caused by the nonzero time constant and elevated transient current, which lead to a longer charge/discharge time and thus the deviations.[22] Specific capacitance of the electrode can be calculated based on the plots using the equation $C_{sp} = \frac{\int idu}{2w\Delta V}$. Depending on the scan rate, the capacitance values ranging from 120 to 210 F/g are obtained, with the highest one being achieved at the scan rate of 5 mV/s.[23, 24]

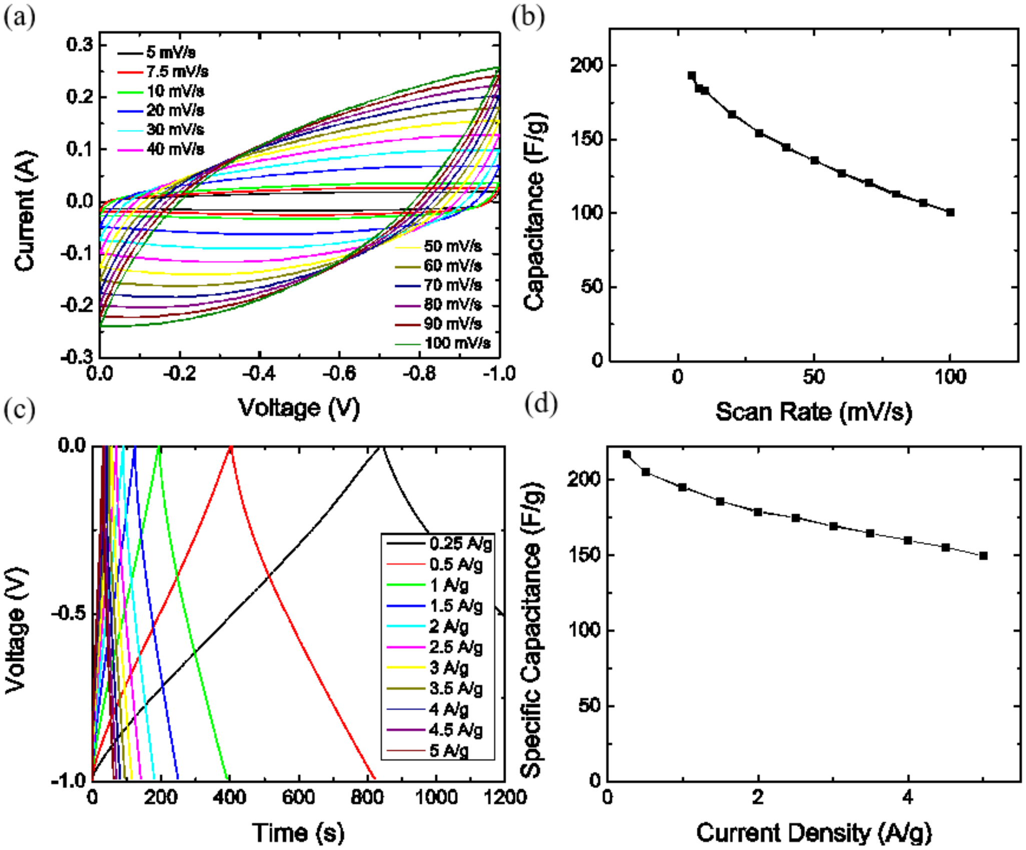

Figure 2.7. (a) CV plots of AC-500-2 at different scan rates. (b) Specific capacitance vs. scan rate of AC-500-2. (c) CCD plots for AC-500-2 at different current densities. (d) Specific capacitance vs. current density for the same sample.

Cyclic charge/discharge (CCD) experiments were performed at different current densities (0.25 - 5.0 A/g) in order to assess the energy and power characteristics of the DDGS-based electrodes (Figure 2.7c). The results reveal that the potential–time curves for all the current densities are isosceles triangles, indicating ideal EDLC behavior, which confirms the results obtained by cyclic voltammetry. Moreover, no discernible internal resistance (IR) drop can be found on both the charge and discharge curves at even the highest current density, suggesting low energy dissipation of the capacitor. The capacitances calculated from the CCD tests are in good accordance with the values derived from the CV tests, ranging from 217 to 150 F/g with the maximum acquired at the current density of 0.25 A/g. As shown by the Figure 2.7d, Csp of the electrode decreases slightly with increasing current density, which can be explained by the fact that at low current densities the electrolyte ions have adequate time to diffuse into the nano-sized pores in the electrode, while at high current densities the process of diffusion cannot be done completely and hence a decrease in the corresponding capacitance is resulted.

The DDGS-based electrodes also show excellent durability. In Figure 2.8a after 1000 cycles of charge–discharge at current density of 1 A/g, the system still retains nearly 99% of its initial capacitance, showing that the material has great stability even at strong alkali environments.

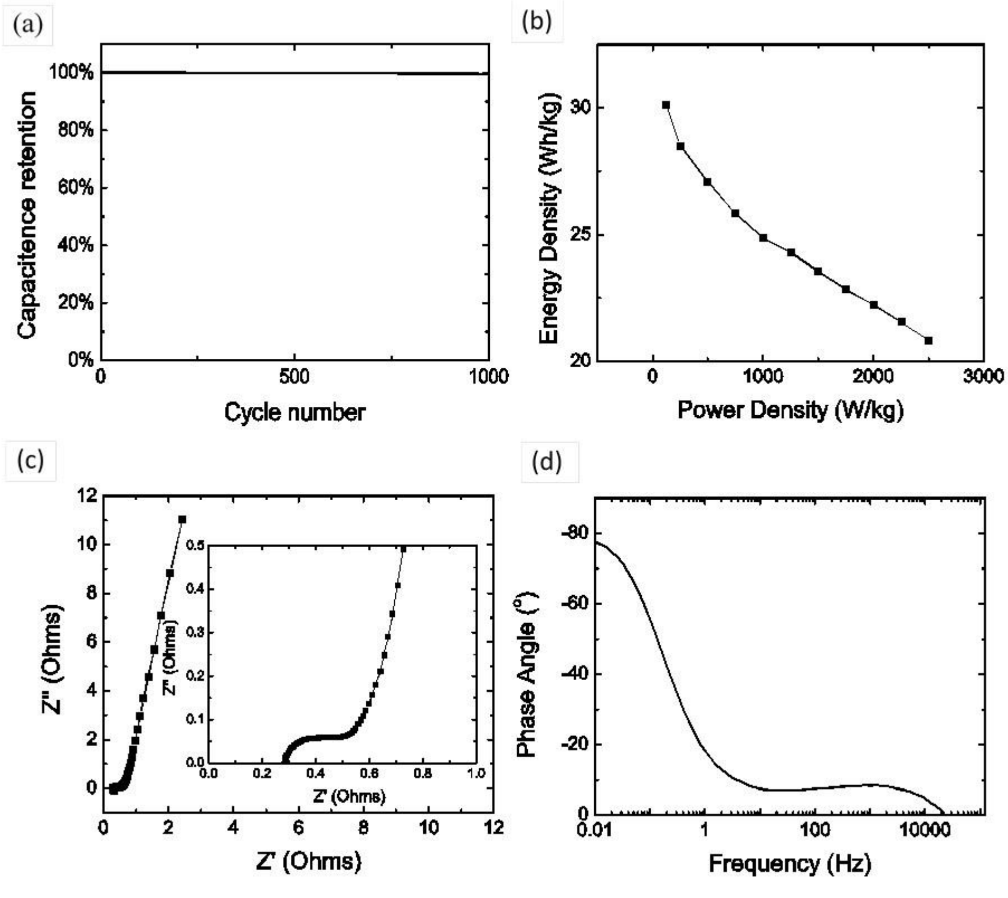

Figure 2.8. (a) Capacitance retention over 1000 cycles. (b) Ragone plot at different current densities. (c) Nyquist plot of the working electrode. (d) Bode plot of the working electrode. All the results are for AC-500-2.

Ragone plots are widely used to evaluate the performance of energy storage devices by plotting energy density versus power density.[25] To investigate the practical function of the prepared electrodes, the energy density and power density were calculated at different current densities according to the equations $D_e = \frac{1}{2} C_{sp} (\Delta V)^2$ and $D_p = \frac{D_e}{\Delta t}$ and the results are plotted in Figure 2.8b, which shows that the working electrode exhibits high power densities up to 2500 W/Kg. As a comparison, conventional batteries such as lithium ion batteries can currently reach a power density around 100 W/Kg.[26] This large difference is caused by their different energy storage mechanisms. EDLCs have the advantages of high power density and rapid charge/discharge due to the reason that the energy stored in a capacitor is by the form of electron field instead of chemical reactions, and the mobility of electrons is much larger than that of lithium ions or any other redox couples.

The electrochemical impedance spectroscopy (EIS) analysis provides additional evaluation on EDLCs' electrochemical performance, such as its frequency dependence and equivalent series resistance (ESR). It is one of the principal methods used for EDLC testing. The EIS analysis in this study was carried out from 0.01 Hz to 105 Hz at open circuit potential with a perturbation of 5 mV. As shown by the complex-plane (Nyquist) impedance plot presented in Figure 2.8c, the impedance spectrum is composed of a semicircle section with a small radius in the high-frequency region, followed by a straight line in the low-frequency region. At low frequencies, the spectrum approaches 90° with respect to the real axis due to the strong capacitive behavior of the electrode. The spectrum intersects with the real axis at a ~45° angle at high frequencies. This type of spectrum can be explained by a series resistor-capacitor (RC) model in which an ideal capacitor is connected with a serial resistance (ESR). In the impedance phase angle - frequency plot (Bode plot, Figure 2.8d), at low frequencies, the working electrode behaves like an ideal capacitor with a phase angle near 90°, but at high frequencies, the resistive component dominates and the phase angle is reduced to nearly 10°, which renders the working electrode resistor-like behavior. This phenomenon is considered to be caused by reduced pore penetration depth at high frequencies, which results in less fraction of pores taking part in the charge/discharge process.[27]

2.3.5. Pseudocapacitance of the DDGS-based ACs

MnO_2 is widely recognized as one of the most suitable materials to make electrodes with high pseudocapacitance because of its high theoretical specific capacitance (1370 F/g),[28] low cost and low environmental impact.[29] Pseudocapacitance is based on the Faradaic redox reactions during charging/discharging processes, which often result in a specific capacitance several times higher than that of electrostatic double-layer capacitance. The mechanism of the redox reaction/charge storage for MnO_2 can be described as follows:[28]

$$(MnO_2) \quad + C^+ + e^- \leftrightarrow (MnO_2C)$$

where C+ denotes electrolyte cations such as Li+, Na+, K+. The specific capacitance of the DDGS-based ACs in this study was further increased by in-situ synthesis of MnO_2 during AC production. The MnO_2 was formed by the reaction between carbon and KMnO4, which can be described as follows in a pH neutral solution:[30]

$$4MnO_4^- + 3C + H_2O = 4MnO_2 + CO_3^{2-} + 2HCO_3^-$$

In Figure 2.9a the formed MnO_2 particles are seen widely distributed on the surface of ACs. The energy dispersive X-ray spectroscopy (EDS) results confirms the existence of Mn (Figure 2.9b). The CV and CCD test results for the AC/ MnO_2 electrode under different voltage scan rates and current rates are shown in Figures 2.9c and 2.9d, respectively. Based on the two Figures, the highest specific capacitance was calculated to be 296.8 F/g (at 10 mV/s) from the CV test and 285.7 F/g (at 1 A/g) from the CCD test. These values are about 1/3 higher than those of the pure ACs, highlighting the significant contribution from the pseudocapacitive behavior of

MnO_2. It should be pointed out that noticeable IR drops can be observed from Figure 2.9d, which is most likely due to the relatively low electrical conductivity of MnO_2.[29]

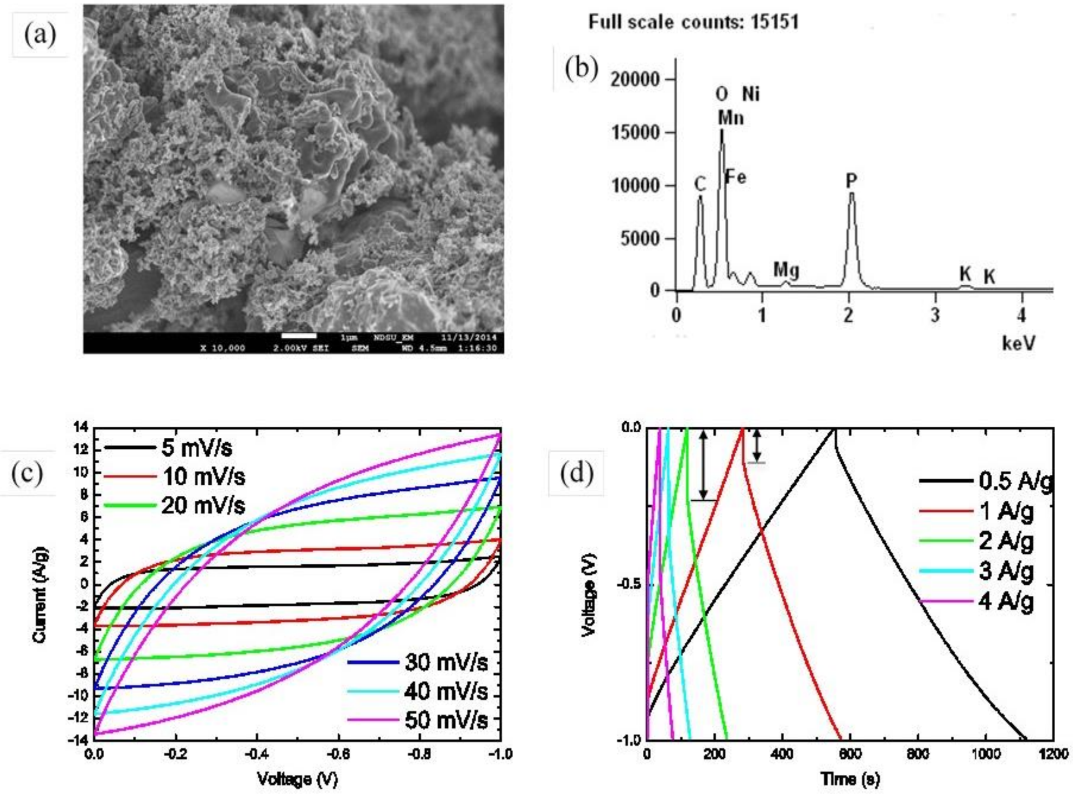

Figure 2.9. (a) SEM picture of in-situ synthesized MnO_2 particles on AC. (b) EDS counts on a selected area of the SEM. (c) CV plots of AC/MnO_2 electrode at different scan rates. (d) CCD plots for AC/MnO_2 at different current densities. Arrows indicate the IR drops when the current direction changes.

2.4. Conclusion

In this research, we developed a one-step facile method to produce 3D porous ACs from DDGS using a microwave-assisted chemical activation method. The surface area of the obtained ACs varied from several hundreds to the maximum of nearly 1036 m^2/g, depending on the acid ratio and the activation temperature. Pore size analysis found that the ACs contained large fraction of micropores. MB adsorption tests showed that the adsorption capacity of the ACs was proportional to their surface areas, with the highest being 477 mg/g for the 1036 m^2/g surface area. The EDLCs based on the DDGS-based ACs exhibited excellent electrochemical performance and stability. The specific capacitances ranging from 120 to 210 F/g were achieved and the electrode showed minimal degradation after 1000 charge/discharge cycles. The specific capacitance can be further improved up to nearly 300 F/g by forming AC/MnO_2 composite with pseudocapacitance behavior. The adsorption and electrochemical test results indicated that the adsorption capacity was determined by the total surface area of the ACs, while the capacitance was critically controlled by both the surface area and the pore size distribution. This study demonstrated the potentials of DDGS in environmental remediation and energy storage applications.

2.5. References

1. Kim, Y.; Mosier, N. S.; Hendrickson, R.; Ezeji, T.; Blaschek, H.; Dien, B.; Cotta, M.; Dale, B.; Ladisch, M. R. *Bioresource Technology* **2008,** 99, (12), 5165-5176.
2. Stein, H. H.; Shurson, G. C. *Journal of Animal Science* **2009,** 87, (4), 1292-1303.
3. Wang, X.; Liang, X.; Wang, Y.; Wang, X.; Liu, M.; Yin, D.; Xia, S.; Zhao, J.; Zhang, Y. *Desalination* **2011,** 278, (1–3), 231-237.
4. Sharma, Y. C.; Uma. *Journal of Chemical & Engineering Data* **2009,** 55, (1), 435-439.
5. Berrios, M.; Martín, M. Á.; Martín, A. *Journal of Industrial and Engineering Chemistry* **2012,** 18, (2), 780-784.
6. Vijayaraghavan, K.; Balasubramanian, R. *Journal of Environmental Chemical Engineering* **2013,** 1, (3), 473-479.
7. Kötz, R.; Carlen, M. *Electrochimica Acta* **2000,** 45, (15–16), 2483-2498.
8. Zhang, L. L.; Zhao, X. S. *Chemical Society Reviews* **2009,** 38, (9), 2520-2531.
9. Horwitz, W.; Latimer, G. W., *Official methods of analysis of AOAC International*. AOAC International: Gaithersburg, Md., 2005.

10. Figueroa-Gerstenmaier, S.; Bonet Avalos, J.; Gelb, L. D.; Gubbins, K. E.; Vega, L. F. *Langmuir* **2003,** 19, (20), 8592-8604.

11. Gañan, J.; González-García, C. M.; González, J. F.; Sabio, E.; Macías-García, A.; Díaz-Díez, M. A. *Applied Surface Science* **2004,** 238, (1–4), 347-354.

12. Rodriguez-Reinoso, F.; Martin-Martinez, J. M.; Prado-Burguete, C.; McEnaney, B. *The Journal of Physical Chemistry* **1987,** 91, (3), 515-516.

13. Sevilla, M.; Parra, J. B.; Fuertes, A. B. *ACS Applied Materials & Interfaces* **2013,** 5, (13), 6360-6368.

14. Groen, J. C.; Peffer, L. A. A.; Pérez-Ramírez, J. *Microporous and Mesoporous Materials* **2003,** 60, (1–3), 1-17.

15. Fu, P.; Hu, S.; Xiang, J.; Sun, L.; Su, S.; Wang, J. *Journal of Analytical and Applied Pyrolysis* **2012,** 98, (0), 177-183.

16. Moreno, A. H.; Arenillas, A.; Calvo, E. G.; Bermúdez, J. M.; Menéndez, J. A. *Journal of Analytical and Applied Pyrolysis* **2013,** 100, (0), 111-116.

17. Liu, L.; Lin, Y.; Liu, Y.; Zhu, H.; He, Q. *Journal of Chemical & Engineering Data* **2013,** 58, (8), 2248-2253.

18. Boyd, G. E.; Adamson, A. W.; Myers, L. S. *Journal of the American Chemical Society* **1947,** 69, (11), 2836-2848.

19. Wang, S.; Zhu, Z. H.; Coomes, A.; Haghseresht, F.; Lu, G. Q. *Journal of Colloid and Interface Science* **2005,** 284, (2), 440-446.

20. Zhao, X.-Y.; Huang, S.-S.; Cao, J.-P.; Xi, S.-C.; Wei, X.-Y.; Kamamoto, J.; Takarada, T. *Journal of Analytical and Applied Pyrolysis* **2014,** 105, (0), 116-121.

21. Zhi, M.; Xiang, C.; Li, J.; Li, M.; Wu, N. *Nanoscale* **2013,** 5, (1), 72-88.

22. Prabaharan, S. R. S.; Vimala, R.; Zainal, Z. *Journal of Power Sources* **2006,** 161, (1), 730-736.

23. Xu, B.; Wu, F.; Chen, R.; Cao, G.; Chen, S.; Zhou, Z.; Yang, Y. *Electrochemistry Communications* **2008,** 10, (5), 795-797.

24. Wang, D.-W.; Li, F.; Liu, M.; Lu, G. Q.; Cheng, H.-M. *Angewandte Chemie International Edition* **2008,** 47, (2), 373-376.

25. Yan, J.; Fan, Z.; Wei, T.; Cheng, J.; Shao, B.; Wang, K.; Song, L.; Zhang, M. *Journal of Power Sources* **2009,** 194, (2), 1202-1207.

26. Wei, D.; Scherer, M. R. J.; Bower, C.; Andrew, P.; Ryhänen, T.; Steiner, U. *Nano Letters* **2012,** 12, (4), 1857-1862.

27. Wang, G.; Zhang, L.; Zhang, J. *Chemical Society Reviews* **2012,** 41, (2), 797-828.

28. Toupin, M.; Brousse, T.; Bélanger, D. *Chemistry of Materials* **2004,** 16, (16), 3184-3190.

29. Wei, W.; Cui, X.; Chen, W.; Ivey, D. G. *Chemical Society Reviews* **2011,** 40, (3), 1697-1721.

30. Jin, X.; Zhou, W.; Zhang, S.; Chen, G. Z. *Small* **2007,** 3, (9), 1513-1517.

3. ROLES OF GRAPHENE OXIDE IN HYDROTHERMAL CARBONIZATION AND MICROWAVE IRRADIATION OF DDGS TO PRODUCE SUPERCAPACITOR ELECTRODES

3.1. Introduction

Activated carbon (AC) has been widely used for the preparation of electrodes of supercapacitors for a long time. The microstructure and electrochemical properties of AC depend mainly on the origins of its precursors and the preparation methods. AC is traditionally produced from nonrenewable coal and peat; biomass such as coconut shell and wood are also used as alternative precursors for AC production. The latter has the advantages of being renewable and largely CO_2 neutral, and therefore has attracted more research interest than the former in recent years. Different biomass materials have been studied for their suitability as AC precursors; process conditions and the resultant microstructure, morphology and electrochemical properties of the produced AC have been investigated.[1-3] Distiller's dried grains with solubles (DDGS), a residual from the corn ethanol industry, is one of the abundant agricultural byproducts that lack high value industrial applications.[4] Carbonization of DDGS to produce high-value carbon materials is a new route to create bio-based energy storage materials and to increase the profit of the corn industry.[5]

In this chapter, a facile method to produce DDGS-based carbonaceous materials using HTC method was developed. Graphene oxide (GO) was added to DDGS to facilitate its carbonization and microwave irradiation was applied to the materials after HTC to reduce GO and promote the formation of highly conductive graphitic carbon. The obtained materials were made into electrodes and their electrochemical properties were tested. This research shows that the GO- and microwave-assisted HTC method is an effective way to carbonize biomass and the produced carbon materials are promising electrode materials for energy storage devices.

3.2. Experimental section

3.2.1. Materials and instruments

DDGS from Tharaldson Ethanol Plant (Casselton, North Dakota) was ground into powder and sieved through a 0.5 mm screen. Hydrothermal autoclave reactor (CIT-HTC230-V50) was purchased from Col-Int Tech. Potassium hydroxide (KOH, Sigma-Aldrich, reagent grade) was used as the activation agent, and the activation process was carried out using a microwave furnace (CEM MAS 7000, maximum power 1400 W) under a nitrogen flow of 1 L/min. Single layer graphene oxide dispersion (GO, 10 mg/ml) was purchased from ACS Material, LLC. Conductive carbon black (TIMCAL SUPER C45), polyvinylidene fluoride (PVDF) binder and N-methyl-2-pyrrolidone (NMP) were purchased from MTI Corporation. All the chemicals in this study were used without further purification. A commercial kitchen microwave (Panasonic NN-T945SF, maximum power 1250 W) was used to further treat the samples. A commercial supercapacitor with activated carbon electrodes (Maxwell Technologies Inc., manufacturer part number BCAP0100 P270 T01) was purchased from Digi-Key Electronics for performance comparison test.

3.2.2. Synthesis of AC from DDGS by HTC method

The scheme of the synthesis process is shown in Figure 3.1. The process includes three main steps: HTC, hydrochar activation, and final carbonization and reduction. In HTC, 15 g DDGS was mixed with 25 g distilled water and 2 g GO dispersion (10 mg/ml) was then added. The mixture was stirred continuously until a homogeneous suspension was formed. 30 g of the suspension was carefully added into the Teflon container of the autoclave (about 80% of the container's volume) and the autoclave was securely sealed. The autoclave was then heated at 200 °C for 18 h for hydrothermal carbonization of the DDGS. The autoclave was cooled down to room temperature naturally at the end of the process and black carbonaceous hydrochar was obtained. In the activation process, 10 g of the hydrochar was first mixed with KOH at 1:1 mass ratio by milling in a mortar; 15 g distilled water was then added and the mixture was stirred to form a paste; The paste was put into the CEM microwave furnace and heated at 600 °C for 20 min under a 1000 mL/min constant nitrogen flow. The produced AC was washed using deionized water until the pH of the effluent was neutral. In the last step, the dried AC was sealed in a vial filled with argon gas and the vial was put in the Panasonic kitchen microwave and heated for 30 s at 1200 W to reduce the GO and graphitize the AC. To explore the carbonization effects of direct microwave irradiation on the hydrochar, the hydrochar before the KOH activation was also treated using the kitchen microwave under the same condition. For comparison, DDGS was also carbonized and activated using the exact same procedure without the assistance of GO.

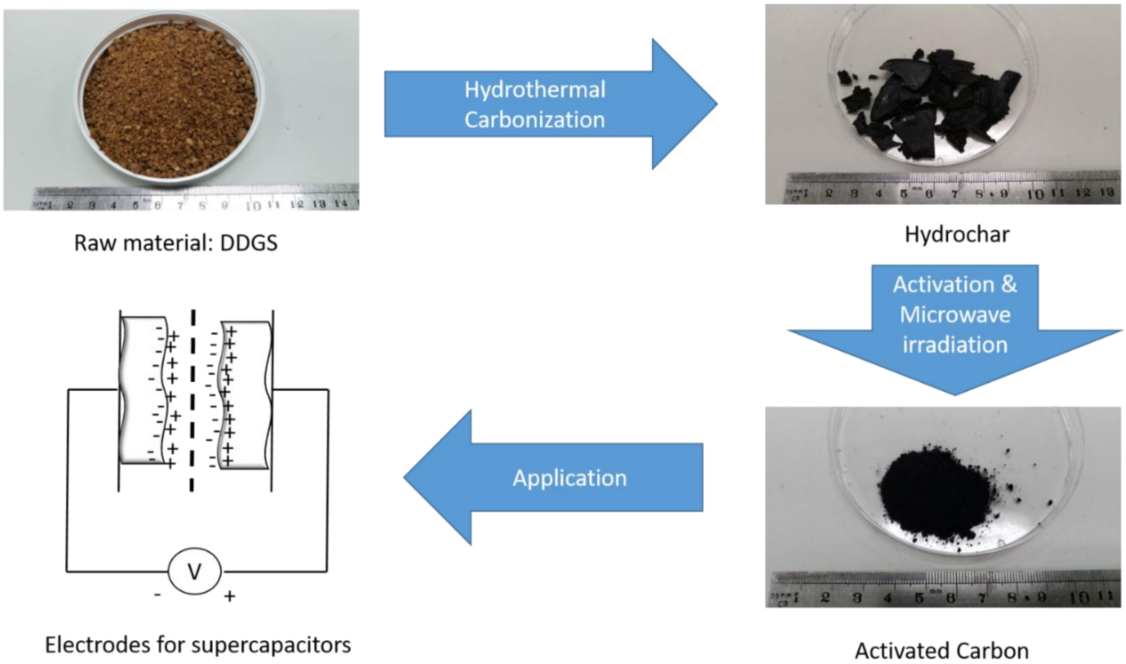

Figure 3.1. Schematic diagram of hydrothermal carbonization and direct microwave irradiation of DDGS and its application as electrodes for supercapacitors.

The surface morphology and the internal structure of the produced AC were studied using scanning electron microscopy (SEM, JEOL JSM-6490LV) and transmission electron microscopy (TEM, JEOL JEM-2100), respectively. Raman measurements were performed using a Nicolet

NXR 9650 FT-Raman spectrometer. X-ray powder diffraction (XRD) analysis was performed on a Phillips X'Pert MPD Powder X-ray Diffractometer. The X-ray used was the Kα radiation (λ=0.1541841 nm) generated from copper at 40 kV and 80 mA. X-ray photoelectron microscopy (XPS) was performed using Thermo Scientific’s K-AlphaTM X-ray Photoelectron Spectrometer system. Fourier transform infrared (FTIR) spectroscopy was performed using a Thermo Scientific Nicolet 8700 FT-IR spectrometer. The KBr pellet method was used and each sample was scanned 32 times at a resolution of 4 cm-1. To measure the electrical conductivity of the AC powder, 0.1g of the powder was compressed in a circular die (ϕ 20 mm) using a hydraulic press at a pressure of 10 MPa. The formed thin disc was then placed in a test cell (EQ-STC split-able test cell, MTI Corporation) for conductivity measurement using a digital multimeter (MASTECH MS8050). The surface area and pore size distribution of the AC were tested using a TriStar II 3020 Automatic Analyzer. The samples were degassed at 150 °C in vacuum overnight, and adsorption/desorption isotherms were taken at 77K using nitrogen as the analysis adsorptive gas.

3.2.3. Electrode preparation and electrochemical tests

To prepare the supercapacitor electrodes, the produced AC was mixed and ground with conductive carbon black and PVDF (80:10:10 by weight) in a mortar; NMP was added to the mixtures and pastes were formed after stirring; the pastes were then coated onto nickel foam current collectors and dried in a vacuum oven overnight at 75 °C to remove NMP; the dried foams were pressed under a 10 MPa pressure to ensure good electrical contacts between the AC and the current collectors. The mass loading of the active materials on the electrodes was around 3 mg/cm^2. For comparison, electrodes were also prepared under the same condition using the AC removed from the Maxwell supercapacitor. The AC was scraped off from the metal foil of the capacitor and then dispersed in NMP to form a paste. The rest of the procedure was identical to the one described above.

All electrochemical tests were performed using a Reference 600 (Gamry Instruments) potentiostat/galvanostat at room temperature. A three-electrode cell was used for the electrochemical test with a graphite rod as the counter electrode, saturated calomel electrode as the reference electrode, and 1M sodium sulfate solution as the electrolyte. Electrochemical performances of the electrodes were tested using cyclic voltammetry (CV), cyclic charge-discharge (CCD) and electrochemical impedance spectroscopy (EIS). The CV tests were performed at different scan rates (10~50 mV/s) between 0 and 0.8 V; the CCD tests were carried out at current densities ranging from 1 A/g to 5 A/g within a voltage window between 0 V and 0.8 V; EIS tests were carried out from 105 Hz to 0.01 Hz with a 5 mV amplitude versus the open circuit potential.

The specific capacitance (Csp) of a single electrode was calculated by the following equation:

$$C_{sp} = \frac{I\Delta t}{w\Delta V}$$

where I is the constant current during the charge/discharge process, w is the total mass of the carbon electrodes, Δt is the time for a full discharging process and ΔV is the voltage window in the CCD test.

The energy density (De) and power density (Dp) of the electrodes were calculated based on the CCD test results using the following equation:

$$D_e = \frac{1}{2} C_{sp} (\Delta V)^2$$

$$D_p = \frac{D_e}{\Delta t}$$

To test the cyclic stability of the electrodes, the CCD test are conducted at a high current density of 5 A/g for 1500 cycles, and the capacitance of the electrodes calculated every 100 cycles.

3.3. Results and discussion

The previous research in chapter 2 shows that the AC produced from DDGS using only microwave furnace activation exhibits spherical structures with relatively smooth surfaces.[5] Other studies about HTC indicate that micron-sized spherical carbon particles are typically formed using the HTC method.[6-8] The GO-assisted HTC treatment used in this study, however, obviously has a large impact on the microstructure of the formed hydrochar, which shows a large number of flakes with a thickness around 40 nm (Figures 3.2a and 3.2b). By contrast, the hydrochar produced under the same HTC condition but without adding GO exhibits an ordinary micro-spherical structure (Figures 3.2c and 3.2d). Considering the thickness of a single layer graphene oxide sheet is only around 1 nm, the much-thicker flakes were most likely formed by a deposition process on the GO substrates.

Micro/nano sized hydrocarbon spheres can be formed through two routes in HTC.[9] First, the fibrous cellulose network of biomass can be disrupted and nano/micro sized cellulose fragments are formed as a result. These fragments form spherical envelopes to minimize their contact with the surrounding water. The cellulose inside undergoes intramolecular condensation, dehydration and decarboxylation reactions, producing hydrochar composed of extensive aromatic networks. Second, various carbohydrates in the biomass can be broken down into glucoses and dissolve in water. The glucoses then undergo a series of dehydration (hydroxymethylfurfural is formed), polymerization and aromatization reactions. The polymerization of hydroxymethylfurfural (HMF) leads to particle nucleation and growth; aromatization of the polymerized HMF (p-HMF) is followed and eventually it leads to the formation spherical carbonaceous particles. When GO is added, its oxygenated surface can attract the cellulose fragments and nucleate the growing p-HMF chains. Either way hydrocarbon will be deposited on the surface of GO and this deposition process eventually produces hydrochar flakes as shown in Figures 3.2a and 3.2b. In addition, it is also possible that the graphitic surface of GO and its oxygenated surface groups catalyzes carbonization of DDGS and promotes carbon growth on the GO surfaces.[6, 10] The flakes produced by this template-guided process exhibit large surface area due to the two-dimensional, high-surface/volume-ratio structure of the GO sheets, which is beneficial to the electrochemical performance of the electrodes that is made from these flakes, as will be discussed later. Compared with Figures 3.2a and 3.2b, the SEM images of the DDGS treated by HTC without using GO (Figures 3.2c and 3.2d) show spherical micro-grains with relatively smooth surface, which is similar to the DDGS without HTC treatment.[5] These experiments confirm that through the addition of only a small amount of GO solution, the morphology after HTC treatment can be significantly changed.

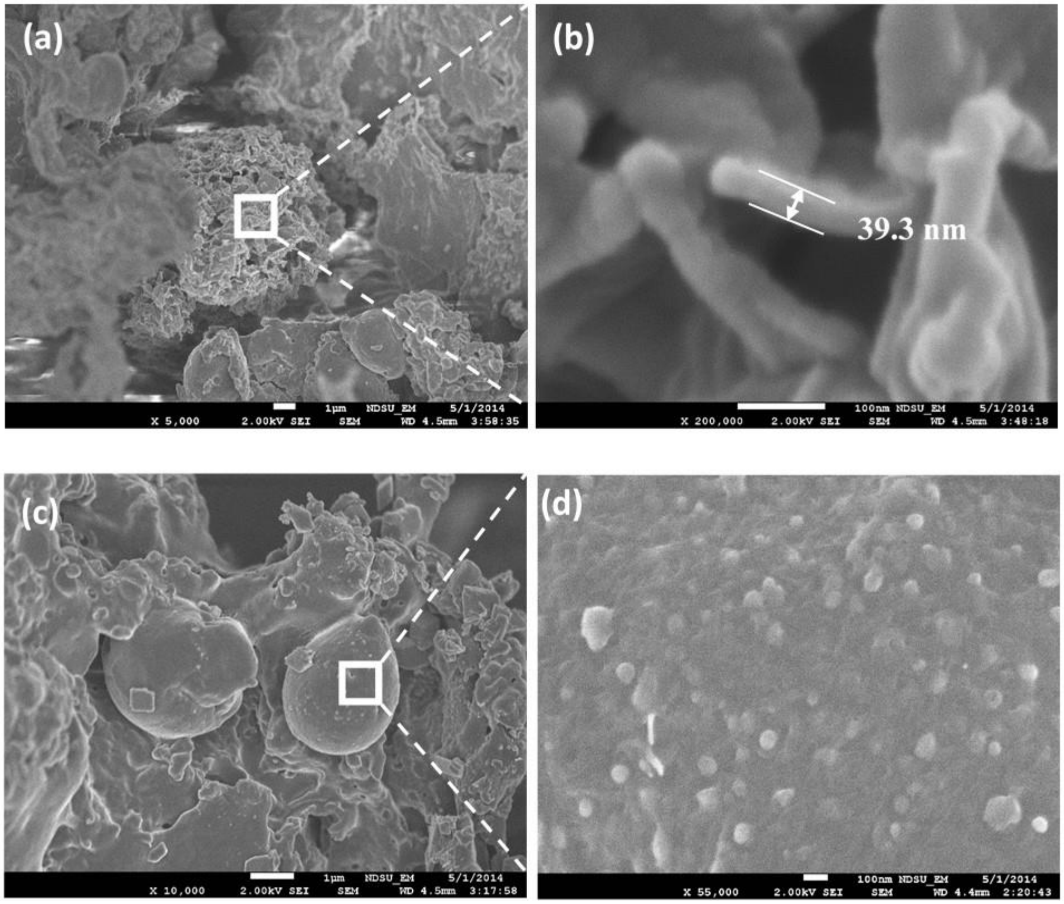

Figure 3.2. SEM images of the hydrochar produced from DDGS using HTC. (a) and (b) GO-assisted HTC. (c) and (d) HTC without GO under the same condition.

Previous researches show that GO can be reduced by being exposed to microwave irradiation in a kitchen microwave for a short period of time (~1 min).[11-14] Absorption of microwave by GO leads to extremely high temperature, which removes the oxygenated functional groups on GO and graphitizes the disordered carbon, and consequently restores high conductivity of graphene.[15] In this study, the hydrochar before and after KOH activation was both treated using direct microwave irradiation. The char was completely dried and sealed in a vial filled with argon gas, and was treated by the kitchen microwave for 30 s. For the char before the activation, sporadic sparking occurred several seconds after the microwave was turned on, and some smog was generated in the sealed container. The sparking was due to the presence of GO in the char and the smoke was produced from the hot spots surrounding the GO. Due to the extremely low concentration of GO in the char, no large scale thermal activities were observed. The result shows that electrical conductivity of the HTC-carbonized hydrochar is low because a significant amount of its carbon still exists as non-conductive carbon or carbon compounds despite markedly lowered oxygen and hydrogen contents in the material after HTC. By contrast, for the char after the activation, violent sparking was observed almost immediately after the irradiation was started. The temperature increased significantly and the entire sample started glowing red. The hydrochar was activated at 600 ^{o}C for 20 min. The degree of carbonization of the hydrochar was further increased during this process by removing most of the non-carbon elements. Therefore, the electrical conductivity of the material after the activation was much higher. Under microwave, this material generated high intensity heat, leading to graphitization of carbon and thermal reduction of GO, i.e., deoxygenation and reordering of the graphene basal plane,[11, 16] which can be detected using XRD and Raman. Because the first treatment method (i.e., without the KOH activation) had only negligible effects on the material, the samples discussed below all underwent the second method (i.e., KOH activation followed by microwave irradiation).

The XRD patterns of the activated hydrochar before and after microwave reduction are shown in Figure 3.3a. Before the reduction, the (002) peak of graphite at around 25° can be observed. However, compared with the sharp (002) peak of natural graphite, the corresponding peak of the hydrochar is broad and weak, indicating a low degree of crystallinity of the material.[17, 18] The hump at around 42° indicates short range order in stacked graphene layers.[18-20] The fact that this hump turns into a stronger peak after microwave reduction indicates that the treated sample contains a higher content of graphene layers. This result is also confirmed by the Raman spectrum shown in Figure 3.3b. Both the D and G bands of the sample after the reduction are more pronounced compared with those before the reduction because of increased degree of carbonization. The higher intensity of the G band than the D band also suggests that most oxygenated groups have been removed from GO by the reduction process and the treated sample contains a significant content of graphene layers.[21] The ratio of the intensity of the D and G bands, which is often used to estimate the degree of disorder, was decreased from 1.1 to 0.6, suggesting a higher degree of graphitization after the microwave irradiation. Both the XRD and Raman results confirm that, through a short burst of microwave irradiation, the GO-assisted hydrochar can be further carbonized and GO can be reduced to pristine graphene, producing a carbon material with high electrical conductivity.

The decrease in the oxygenated groups caused by microwave irradiation was also confirmed by the XPS and FTIR results. The XPS C1s spectra before and after the irradiation are compared in Figure 3.3c. It can be observed that the region between 286 and 289 eV, which represents the epoxide, hydroxyl, carboxyl groups, is decreased after the irradiation.[12, 22] The atomic percentage of oxygen calculated by the XPS spectra shows that the content of oxygen decreases from 22.22% to 16.96% by the treatment. The FTIR spectra in Figure 3.3d show that the peaks for the oxygen-containing groups, i.e. C=O (1730 cm-1), C-O (1414 cm-1 and 1228 cm-1), and O-H (3400 cm-1), are attenuated significantly after the irradiation.[13, 23] Both results indicate the reduction of GO.

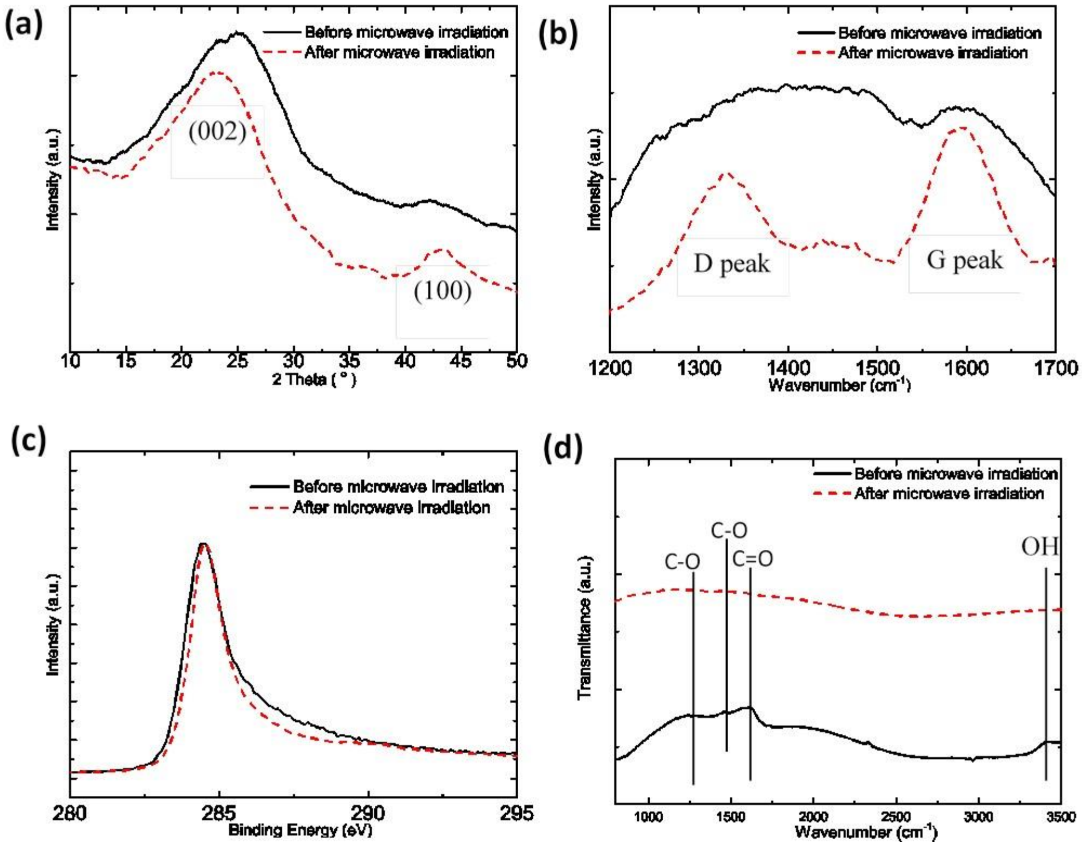

Figure 3.3. XRD patterns (a), Raman spectra (b), XPS spectra (c) and FTIR results (d) of the GO-assisted, KOH-activated hydrochar before and after microwave irradiation.

The morphology of the hydrochar changed dramatically after the chemical activation and the microwave irradiation, and a 3D porous carbon network was formed as shown in Figure 3.4. The relatively smooth surface shown in Figure 3.2 is now decorated with numerous interconnected pores measuring 100~1000 nm (Figures 3.4b and 3.4c). This dramatic morphology change is caused by the oxidizing reaction between carbon and the activation agent. Many activation mechanisms have been proposed to explain the KOH activation process. Otowa et al. proposed that when the temperature for activation was below 700 °C, several simultaneous/consecutive reactions happened as follows.[24]

$$2KOH \rightarrow K_2O + H_2O \text{ (dehydration)}$$

$$C + H_2O \rightarrow CO + H_2 \text{ (water-gas reaction)}$$

$$CO + H_2O \rightarrow CO_2 + H_2 \text{ (water-gas shift reaction)}$$

$$CO_2 + K_2O \rightarrow K_2CO_3 \text{ (carbonate formation)}$$

According to this mechanism, KOH dehydrates and transforms into K_2O at 400 °C, then the reaction of carbon and H_2O causes the carbon to be partially consumed, forming a porous structure which is the typical character of AC. K_2CO_3 is formed by the reaction of K_2O and CO_2, and it can be removed by washing the AC continuously using DI water. It has been reported that the formation of K_2CO_3 was observed at about 400 °C, and all the KOH was completely consumed and transformed to K_2CO_3 around 600°C.[25] Figure 3.4d shows that the final AC after the microwave irradiation possesses a hierarchical structure with pore size ranging from micrometer to nanometer. This interconnected 3D network can provide significant surface area, transportation pathways, and reservoirs for the electrolyte ions in a supercapacitor, which is necessary to achieve high energy storage performance.

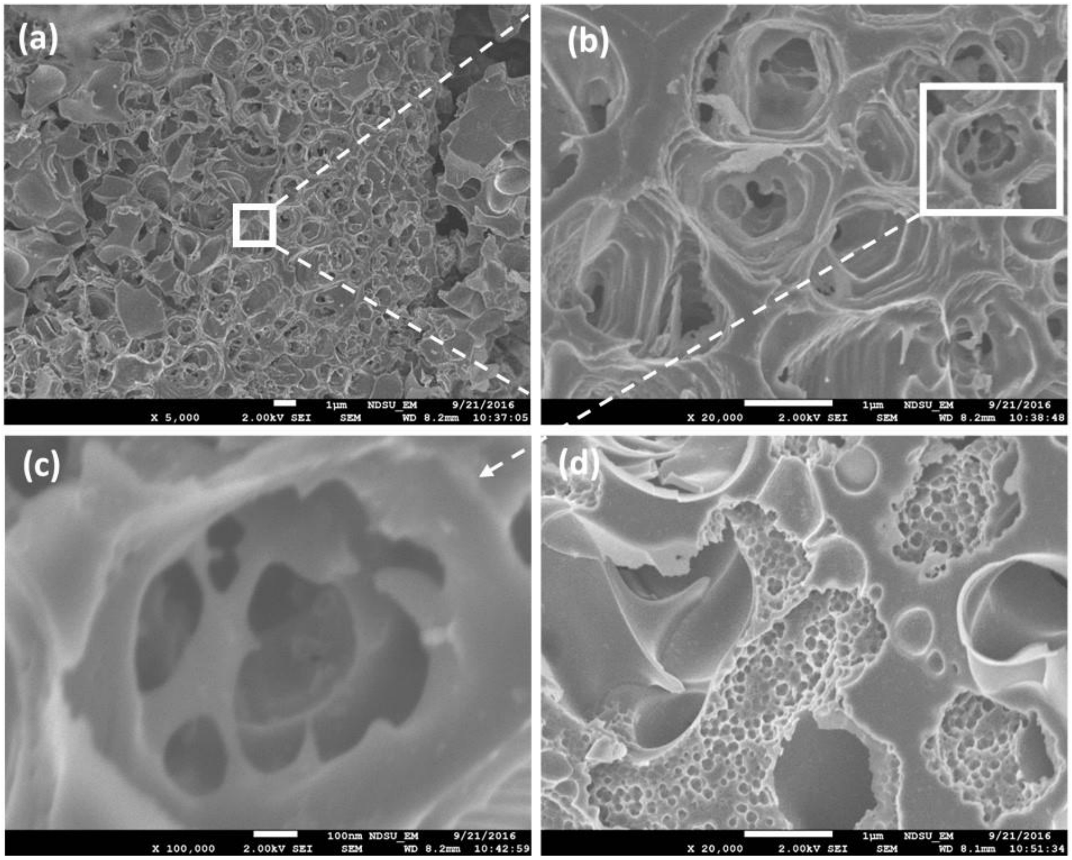

Figure 3.4. SEM images taken at different magnifications for the DDGS-based AC after the KOH chemical activation and the microwave irradiation.

TEM study was performed to determine the internal structure differences between the AC produced with and without using GO. The AC without GO presents an amorphous structure without showing any graphitic layers (Figure 3.5a). In contrast, the layered graphene planes, which align in different directions in different regions of the sample (i.e. a polycrystalline structure), can be observed in the AC with GO (Figures 3.5b). The interplanar distance of the graphene is estimated to be 0.34 nm (Figure 3.5b inset). The selected area electron diffraction (SAED) pattern shows three major diffraction rings (Figure 3.5c), which can be attributed to the (002), (101) and (112) planes of the stacked graphene layers.[26] Several diffraction spots originated from single crystal diffraction are also visible in the Figure 3.5c. This diffraction pattern confirms the polycrystalline structure of the GO-containing AC.

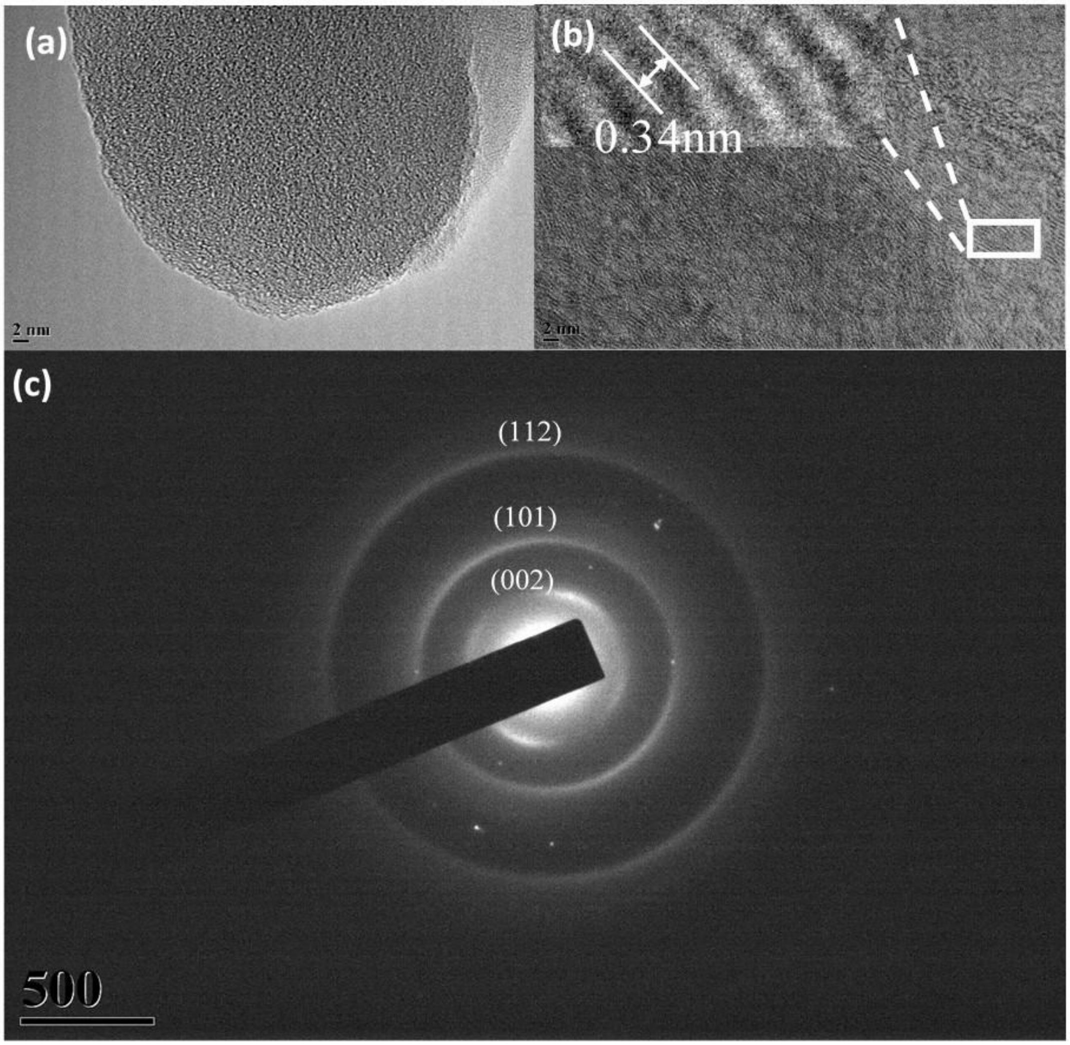

Figure 3.5. (a) TEM images of the AC without GO. (b) TEM images of the AC with GO. The insert shows interplanar distance of the graphene layers. (c) SAED pattern of the AC with GO, showing mostly a polycrystalline structure.

The N_2 adsorption–desorption isotherms of the AC prepared with and without GO are compared in Figure 3.6a. Both curves can be characterized as type II isotherms according to the BDDT (Brunauer–Deming–Deming–Teller) classification.[27] The isotherms are S-shaped and they represent standard form of multilayer isotherms.[28] The fast increase in adsorbed volume at the initial region ($P/P_0<0.2$) on the adsorption curves indicates the presence of a large amount of micropores.[29] The intermediate region is relatively flat and it corresponds to monolayer adsorption, and the last increasing region reflects multilayer adsorption. The hysteresis loops are attributed to the existence of mesoporous structure. The surface area for the AC with and without GO were calculated to be 479.1543 m²/g and 432.4943 m²/g, respectively. It should be noted that due to a relatively low activation temperature (600°C) used in the experiments, the surface area is not as large as those reported by other groups. Higher temperature can facilitate the development of porous structure, which can further increase the surface area of AC.[5] The pore size distribution (Figure 3.6b) was calculated based on the BJH theory. For both samples, the sizes of most of the pores are within the micropore region (i.e. < 2 nm). The average pore width for both samples is around 2.9 nm.

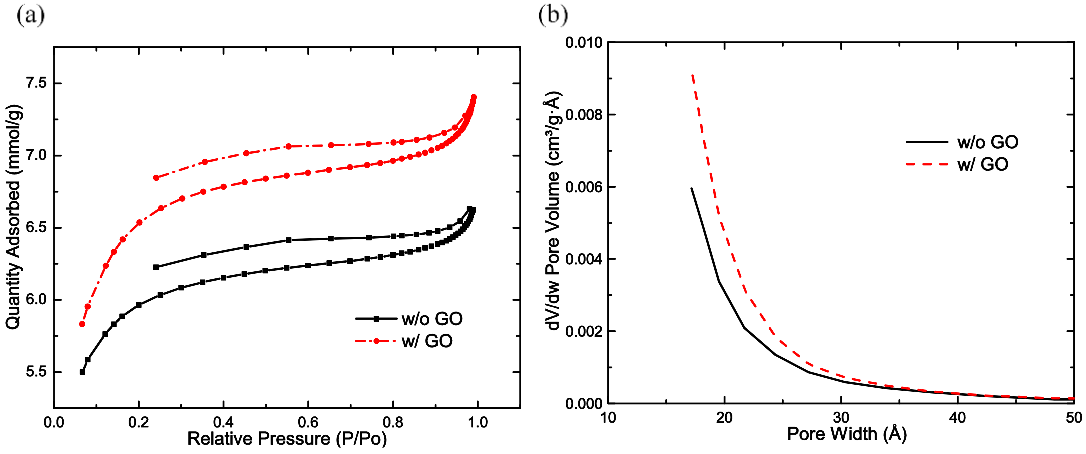

Figure 3.6. N_2 adsorption–desorption results at 77 K for the AC with and without GO. (a) Isotherms. (b) Pore volume distributions based on BJH analysis.

CV, CCD and EIS tests were conducted in 1 M Na_2SO_4 aqueous solution to study the electrochemical properties of the electrodes fabricated using the produced AC. The CV tests were conducted by sweeping the voltage linearly from 0 to 0.8 V versus a saturated calomel reference electrode. It can be observed from Figure 3.7a that the CV curves at low scan rates (10 and 20 mV/s) show a near-rectangular shape, indicating an electric double-layer capacitors behavior with good rate performance. The shape of the CV curves deviates from the quasi-rectangular shape at high scan rates due to the existence of resistances between electrodes and electrolyte.

The CCD results at different current densities (1~5 A/g) are shown in Figure 3.7b. Both the charge and discharge curves are highly linear and the charge/discharge curves are almost symmetrical. The value of specific capacitance is 101.5 F/g at 1 A/g, and it decreases to 70.1 F/g at 5 A/g (Figure 3.7c). This decrease is common among many studies and it can be attributed to insufficient ion transport and adsorption and high IR drop under high current densities.[30-32] The CCD curves demonstrate the supercapacitors have excellent electrochemical reversibility and high Coulombic efficiency. The IR drop at a high current density reflects the intrinsic resistance of the active material.

EIS analysis was carried out within a frequency range from 0.01 Hz to 100k Hz. The Nyquist plot, i.e. the imaginary part (Z') of the impedance vs. the real part (Z'') of the impedance, is shown in Figure 3.7d. The intercept on the real axis represents the equivalent series resistance (ESR), which represents the effect of the intrinsic active material resistance, the ionic resistance of the electrolyte and the contact resistance at the active material/current collector interface. The inset in Figure 3.7d reveals an ESR of ~4.2 Ω, which can be ascribed to the influence of the insulating binder material (PVDF) used during the electrode fabrication. The ESR also explains the IR drop at the beginning of discharge process at the CCD experiments. A relatively short line with a 45° angle to the real axis at high frequencies was observed, which is called Warburg region and is related to the diffusion of the ions into the bulk of electrodes.[33] At low frequencies region, the curve becomes almost vertical to the real axis, indicating ideal capacitive behavior. The semi-circle near the real axis at high frequency represents the charge transfer resistance (R_{ct}) at the electrode/electrolyte interface.[34] Based on the Nyquist plot, the as-prepared electrodes show an Rct around 2 Ω, which is common for porous electrodes.[35] The inset of Figure 3.7c shows an equivalent circuit for the EIS data, where R_s is the bulk solution resistance, C_{cl} represents the double layer capacitance, R_{ct} is the charge transfer resistance, W is the Warburg impedance resulted from the diffusion of ions, and C_l is the limit pseudocapacitor caused by the residual heteroatoms of the HTC process.[36, 37]

The impedance phase angle dependence on frequency (Bode plot) is presented in Figure 3.7e. It can be observed that at low frequencies, the working electrode shows a near 90° phase angle, which is the behavior of an ideal capacitor. At high frequencies, however, the phase angle is reduced to nearly 10°, indicating that the supercapacitor behaves like a pure resistor. This is because at high frequencies, electrolyte ions can hardly penetrate into micropores of the electrodes, which can dramatically reduce the specific capacitance.[38] Furthermore, the electrodes also show excellent cyclic durability as shown in Figure 3.7f. The capacitance retention is around 92.3% of the original value even after 5000 charge/discharge cycles at a high current density of 5 A/g, indicating good stability at high current densities.

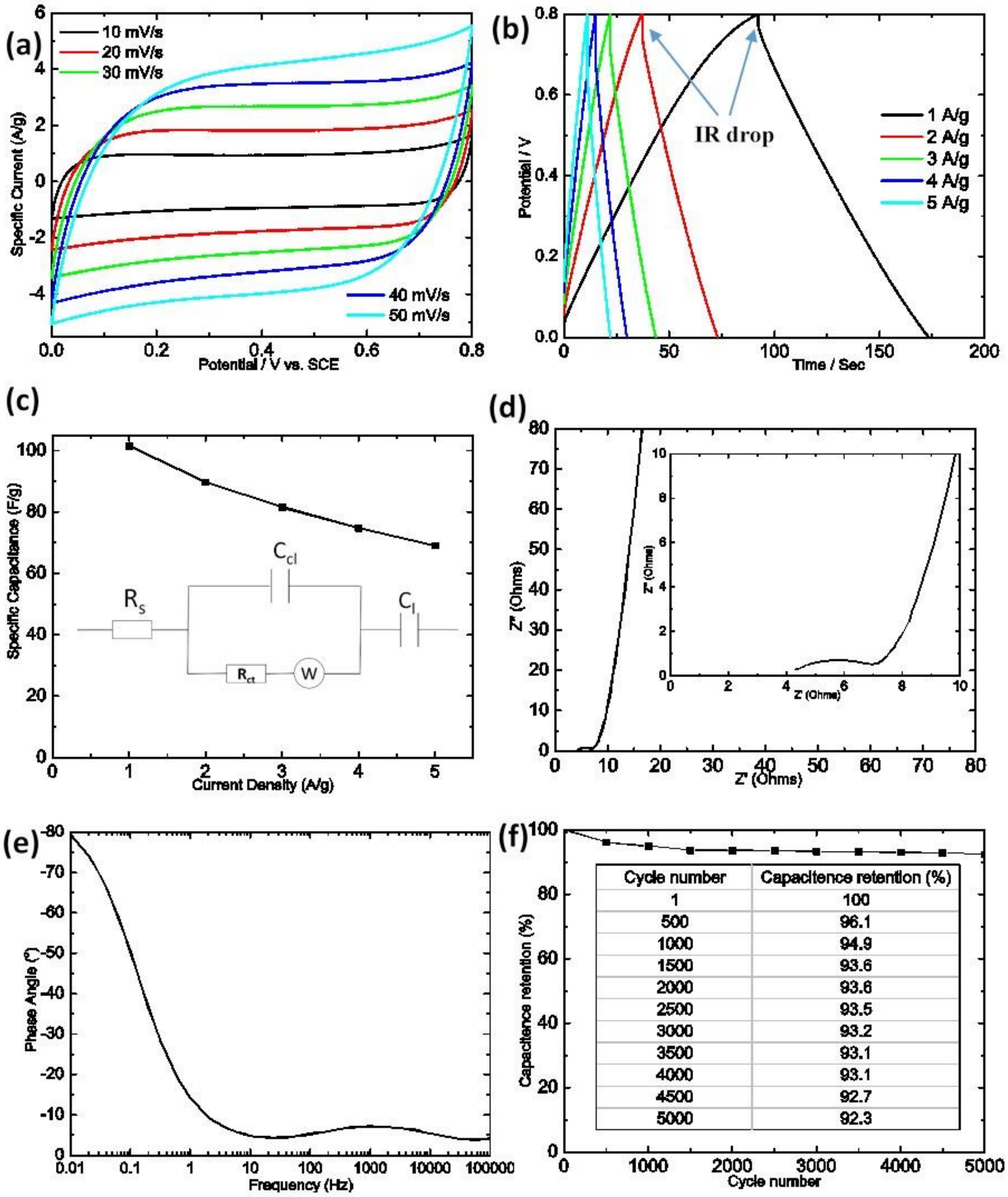

Cycle number	Capacitence retention (%)
1	100
500	96.1
1000	94.9
1500	93.6
2000	93.6
2500	93.5
3000	93.2
3500	93.1
4000	93.1
4500	92.7
5000	92.3

Figure 3.7. Electrochemical test results of the electrodes made from the DDGS-based AC produced through consecutive HTC-KOH activation-microwave irradiation processes. (a) CV curves at various scan rates. (b) Cyclic charge/discharge curves at different current densities (c) Specific capacitance vs. current density ranging from 1 to 5 A/g. The inset shows an equivalent circuit that fits the EIS data. (d) Nyquist plot of the EIS data. (e) Bode plot of the EIS data. (f) Capacitance retention over 5000 cycles at 5 A/g.

The Ragone plot, which shows the energy densities versus the power densities at different current densities, is presented in Figure 3.8. The plot shows that the electrode exhibits high power densities up to 4000 W/Kg and high energy densities near 9 Wh/Kg. Based on the electrochemical tests, it can be concluded that the electrode has high energy densities, excellent cyclability and fast charge/discharge process, which meet the demand of the electrochemical performances of a typical supercapacitor.[39, 40]

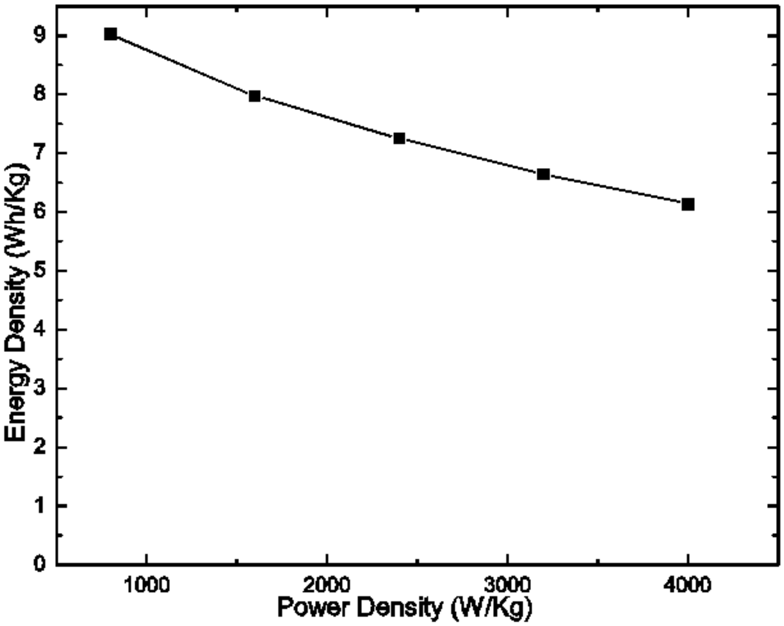

Figure 3.8. Ragone plot at different current densities for the DDGS-based electrodes.

All the afore-discussed results are based on the samples that contain GO to promote biomass carbonization and graphitization. Aside from the evidences from the microscope and spectroscopy studies, the importance of GO can also be shown through electrochemical tests. DDGS without GO was converted into AC following the exact same procedure and the product was subjected to CCD and EIS tests, whose results are compared with those for the samples containing GO in Figures 3.9a and 3.9b, respectively. The conductivity measurement results show that the areal electrical resistivity of the AC with and without GO is 3.13 Ω/cm^2 and 5.51 Ω/cm^2, respectively. The conductivity increase due to the GO addition is also reflected by the decreases in the IR drop (Figure 3.9a) and in the ESR (Figure 3.9b), which both are attributed to the higher conductivity imparted by a higher degree of biomass carbonization and graphitization that is facilitated by GO. The electrode containing GO also shows longer charge and discharge time, indicating a larger specific capacitance (54.4% higher) compared with the electrode without GO (Figure 3.9a). The CCD and EIS results of the AC from the commercial supercapacitor are also shown in Figure 3.9 for comparison. The AC produced in this study possess significantly larger capacitance than the commercial one (23.6 F/g). This result demonstrates that the AC produced using HTC treatment and microwave irradiation is a promising electrode material for supercapacitors.

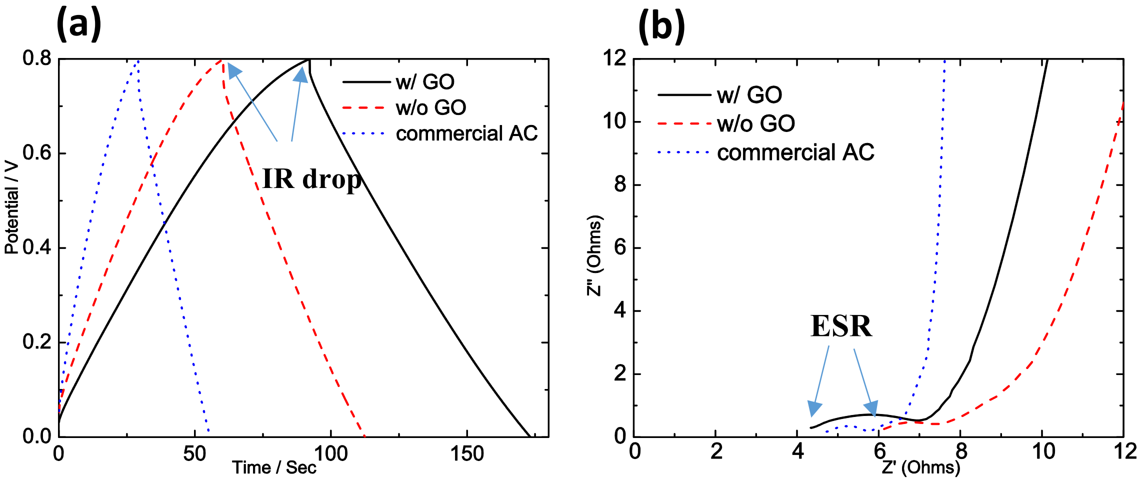

Figure 3.9. Electrochemical properties of the AC with and without GO and the commercial AC. (a) CCD curves at 1 A/g. (b) EIS curves in the high frequency region.

3.4. Conclusion

In summary, a facile GO-assisted HTC and microwave irradiation process was developed to convert DDGS into supercapacitor-ready AC. GO was shown to play an important role in increasing the electrochemical properties of the produced AC. It changed the shape of the hydrochar particles from spheres to flakes by serving as a carbonization template. It absorbed microwave irradiation to create high temperature for carbonization and graphitization. The final microwave irradiation was proved to be a highly effective method to rapidly increase the degree of carbonization and graphitization of the hydrochar. This study shows that direct carbonization of wet DDGS (or other biomass) using HTC followed by microwave irradiation represents a highly energy-efficient method to produce high value carbon materials.

3.5. References

1. Tay, T.; Ucar, S.; Karagöz, S. *Journal of Hazardous Materials* **2009,** 165, (1–3), 481-485.

2. Liou, T.-H. *Chemical Engineering Journal* **2010,** 158, (2), 129-142.

3. Zhang, J.; Xiang, J.; Dong, Z.; Liu, Y.; Wu, Y.; Xu, C.; Du, G. *Electrochimica Acta* **2014,** 116, 146-151.

4. Kim, Y.; Mosier, N. S.; Hendrickson, R.; Ezeji, T.; Blaschek, H.; Dien, B.; Cotta, M.; Dale, B.; Ladisch, M. R. *Bioresource Technology* **2008,** 99, (12), 5165-5176.

5. Wang, Y.; Zhou, J.; Jiang, L.; Ulven, C.; Lubineau, G.; Liu, G.; Xiao, J. *J Polym Environ* **2015,** 23, (4), 595-605.

6. Krishnan, D.; Raidongia, K.; Shao, J.; Huang, J. *ACS Nano* **2014,** 8, (1), 449-457.

7. Heilmann, S. M.; Jader, L. R.; Sadowsky, M. J.; Schendel, F. J.; Von Keitz, M. G.; Valentas, K. J. *Biomass and Bioenergy* **2011,** 35, (7), 2526-2533.

8. Sevilla, M.; Macia-Agullo, J. A.; Fuertes, A. B. *Biomass and Bioenergy* **2011,** 35, (7), 3152-3159.

9. Falco, C.; Baccile, N.; Titirici, M.-M. *Green Chemistry* **2011,** 13, (11), 3273-3281.

10. Singh, R. K.; Kumar, R.; Singh, D. P. *RSC Advances* **2016,** 6, (69), 64993-65011.

11. Voiry, D.; Yang, J.; Kupferberg, J.; Fullon, R.; Lee, C.; Jeong, H. Y.; Shin, H. S.; Chhowalla, M. *Science* **2016,** 353, (6306), 1413-1416.

12. Zhu, Y.; Murali, S.; Stoller, M. D.; Velamakanni, A.; Piner, R. D.; Ruoff, R. S. *Carbon* **2010,** 48, (7), 2118-2122.

13. Chen, W.; Yan, L.; Bangal, P. R. *Carbon* **2010,** 48, (4), 1146-1152.

14. Kumar, R.; Singh, R. K.; Dubey, P. K.; Singh, D. P.; Yadav, R. M. *ACS Applied Materials & Interfaces* **2015,** 7, (27), 15042-15051.

15. Kumar, R.; Singh, R. K.; Tiwari, V. S.; Yadav, A.; Savu, R.; Vaz, A. R.; Moshkalev, S. A. *Journal of Alloys and Compounds* **2017,** 695, 1793-1801.

16. Kumar, R.; Singh, R. K.; Vaz, A. R.; Moshkalev, S. A. *RSC Advances* **2015,** 5, (83), 67988-67995.

17. Hu, H.; Zhao, Z.; Zhou, Q.; Gogotsi, Y.; Qiu, J. *Carbon* **2012,** 50, (9), 3267-3273.

18. Bele, S.; Samanidou, V.; Deliyanni, E. *Chemical Engineering Research and Design* **2016,** 109, 573-585.

19. Stobinski, L.; Lesiak, B.; Malolepszy, A.; Mazurkiewicz, M.; Mierzwa, B.; Zemek, J.; Jiricek, P.; Bieloshapka, I. *Journal of Electron Spectroscopy and Related Phenomena* **2014,** 195, 145-154.

20. Kumar, R.; Singh, R. K.; Savu, R.; Dubey, P. K.; Kumar, P.; Moshkalev, S. A. *RSC Advances* **2016,** 6, (32), 26612-26620.

21. Li, Y.; Zhao, X.; Zhang, P.; Ning, J.; Li, J.; Su, Z.; Wei, G. *Journal of Materials Chemistry C* **2015,** 3, (16), 4126-4133.

22. Zhu, Y.; Murali, S.; Stoller, M. D.; Ganesh, K.; Cai, W.; Ferreira, P. J.; Pirkle, A.; Wallace, R. M.; Cychosz, K. A.; Thommes, M. *Science* **2011,** 332, (6037), 1537-1541.

23. Guo, H.-L.; Wang, X.-F.; Qian, Q.-Y.; Wang, F.-B.; Xia, X.-H. *ACS Nano* **2009,** 3, (9), 2653-2659.

24. Otowa, T.; Tanibata, R.; Itoh, M. *Gas Separation & Purification* **1993,** 7, (4), 241-245.

25. Díaz-Terán, J.; Nevskaia, D. M.; Fierro, J. L. G.; López-Peinado, A. J.; Jerez, A. *Microporous and Mesoporous Materials* **2003,** 60, (1–3), 173-181.

26. Ma, J.; Li, G.-y.; Chu, Z.-y.; Li, X.-d.; Li, Y.-h.; Hu, T.-j. *Carbon* **2014,** 69, 634-637.

27. Gregg, S.; Jacobs, J. *Transactions of the Faraday Society* **1948,** 44, 574-588.

28. Fraissard, J. P., *Physical Adsorption: Experiment, Theory, and Applications*. Springer Science & Business Media: 1997; Vol. 491.

29. Zhao, Y.; Liu, M.; Deng, X.; Miao, L.; Tripathi, P. K.; Ma, X.; Zhu, D.; Xu, Z.; Hao, Z.; Gan, L. *Electrochimica Acta* **2015,** 153, 448-455.

30. Portet, C.; Taberna, P. L.; Simon, P.; Flahaut, E.; Laberty-Robert, C. *Electrochimica Acta* **2005,** 50, (20), 4174-4181.

31. Gupta, V.; Miura, N. *Electrochemical and Solid-State Letters* **2005,** 8, (12), A630-A632.

32. Portet, C.; Taberna, P. L.; Simon, P.; Flahaut, E. *Journal of Power Sources* **2005,** 139, (1–2), 371-378.

33. Wei, L.; Sevilla, M.; Fuertes, A. B.; Mokaya, R.; Yushin, G. *Advanced Functional Materials* **2012,** 22, (4), 827-834.

34. Chang, J.; Gao, Z.; Wang, X.; Wu, D.; Xu, F.; Wang, X.; Guo, Y.; Jiang, K. *Electrochimica Acta* **2015,** 157, 290-298.

35. Ren, G.; Li, S.; Fan, Z.-X.; Hoque, M. N. F.; Fan, Z. *Journal of Power Sources* **2016,** 325, 152-160.

36. Wu, X.-L.; Wen, T.; Guo, H.-L.; Yang, S.; Wang, X.; Xu, A.-W. *ACS Nano* **2013,** 7, (4), 3589-3597.

37. Chen, W.-C.; Wen, T.-C. *Journal of Power Sources* **2003,** 117, (1–2), 273-282.

38. Wang, G.; Zhang, L.; Zhang, J. *Chemical Society Reviews* **2012,** 41, (2), 797-828.

39. Zhang, L. L.; Zhao, X. S. *Chemical Society Reviews* **2009,** 38, (9), 2520-2531.

40. Kumar, R.; Kim, H.-J.; Park, S.; Srivastava, A.; Oh, I.-K. *Carbon* **2014,** 79, 192-202.

4. THE APPLICATION OF CARBON NANOPARTICLES/POLYANILINE ELECTRODE AND ITS COMPARATIVE STUDY WITH CNPS/MNO_2 IN SUPERCAPACITORS

4.1. Introduction

The combustion process of a hydrocarbon material is a complicated process that involves the decomposition of long-chain hydrocarbons during the initial stage, followed by the formation of C_2, C_3, C_2H_2 and other small radicals. The formation of C-H containing graphitic fragments and dense carbon clusters (e.g. carbon nanoparticles (CNPs)) leads to the complex carbonaceous structures in heavy soot.[1] Due to incomplete combustion of fossil fuels, CNPs are unavoidably generated during the combustion process and these ultra-fine particles are generally emitted into air,[2] accounting for a significant source of air pollution.[3, 4] On the other hand, the CNPs generated in the combustion process can be conveniently collected by placing noncombustible substrates, such as carbon fabrics,[5] anodic aluminum oxide films[1] or glass slides,[6] over the flame. Carbon quantum dots, a promising candidate for carbon materials with unique properties, can also be produced using this facile and low-cost way, which has attracted increasing attention recently.[7] The as-formed CNPs generally have a spherical shape and pile up loosely on the substrates, forming a porous, fractal-like network structure with a large specific surface area.[8] The diameter of a single CNP typically ranges from 10 to 50 nm, which is similar to the pore size of the network. CNPs have been widely investigated for their application as a detector for the identification of highly toxic contaminants such as heavy metal ions Hg^{2+} and Ag^+.[9, 10] CNPs have been used as a low-cost and effective fluorescent sensing platform for Ag+ detection both in pure buffer and real samples. They exhibit a lower detection limit (500 ppm) compared to that of previously reported single-walled carbon nanotubes (SWCNT) and graphene oxide (GO) sensing platforms.[11] In the field of bio-nanotechnology, CNPs are recognized as a class of novel fluorescent nanomaterials with multi-color fluorescence and excellent photostability in various pH conditions.[12, 13] The unique interconnected 3D structure of CNPs can be used as a template for making superamphiphobic coatings.[14-16] This structure is also suitable for supercapacitor applications, featuring a relatively high specific capacitance and a high cycle stability due to the ease of ion transportation in the structure.[6]

Electrochemical capacitors (ECs) (also widely known as supercapacitors), a form of electrochemical energy storage device with short charging/discharging time, high power density and long cycle life, have recently attracted much attention and become one of the most promising energy-storage devices for the future.[17] ECs have the ability to output significantly more power in a relatively short time compared with traditional batteries, but also come with disadvantages including limited total energy capacity.[18] A complete EC generally consists of two electrodes, electrolyte and a non-conductive separator. The electrodes are generally made by materials with large specific area, well-developed porous structure and high electronic conductivity, and are the most decisive factors for the overall performance of supercapacitors among the three components.[19] Based on different energy storage mechanisms, ECs can be classified into two categories. The electrical double-layer capacitors (EDLCs) are the basic type of ECs, in which the energy is stored as electrostatic field generated by charges gathering at the interface between the electrode surface and the electrolyte (also called non-Faradaic charge storage).[18] The pseudocapacitors are a modified and improved version of EDLCs, whose capacitance arises not only from the non-Faradaic charge storage, but are also increased by fast and reversible redox reactions between electrodes materials and the electroactive composition in electrolytes.[20]

The CNPs generated during a combustion process show great potential as electrodes of ECs because of the existence of interconnected pores of the fractal-like network, and their energy storage performance can be enhanced by incorporating materials with pseudocapacitive behavior.[21] Yuan et al. fabricated a highly flexible solid-state supercapacitor with CNPs/MnO_2 nanorods hybrid structure on the basis of CNPs produced by a flame synthesis method, and enhanced its performance by using electrochemical deposited MnO_2 nanoparticles.[22] The device exhibited good electrochemical performance due to the porous and conductive CNPs as an outstanding substrate for the electrodes. Conducting polymers, such as polyaniline (PANI), polypyrrole, polythiophene and derivatives of polythiophene, can also be used to fabricate pseudocapacitors with their advantages of high charge density and relatively low cost compared with the metal oxides.[23] Male et al. successfully developed a hybrid material via in situ polymerization of aniline with graphitized mesoporous carbon, and the mesoporous carbon can increase the specific capacitance and cycle stability of the electrodes.[24] The PANI/activated carbon (AC) nanocomposite were also successfully prepared by electropolymerization of aniline monomers on the surface of AC, and a high specific capacitance of 338.15 F/g was achieved because of the large surface area provided by the AC and the pseudocapacitance contribution of PANI.[25] In this study, we explored the methods to prepare CNPs/PANI composites and fabricate the electrodes of ECs by in situ electrodeposition technique, and compared their performance with that of CNPs/MnO_2 composites. No binders and conductive additives were used to fabricate the electrodes, which simplifies the preparing process and contributes to a higher power density and better cycling performance.[26] A flexible, solid-state supercapacitor was also fabricated using polyvinyl alcohol (PVA)/H_3PO_4 solution as electrolyte, and the complete device was used to light a light-emitting diode (LED) in order to demonstrate its application for energy storage.

4.2. Experimental section

4.2.1. Materials and chemicals

Paraffin candles and laminating pouches were purchased from a local store. Aniline, poly (vinyl alcohol) (PVA, Mw = ~31,000), manganese nitrate ($Mn(NO_3)_2$) and sodium nitrate ($NaNO_3$) were purchased from Sigma-Aldrich. Sulfuric acid (98%) was purchased from BDH Aristar Corporation. Nickel and copper foams with a thickness of 0.08 mm were purchased from MTI Corporation. Sodium sulfate (Na_2SO_4) and hydrochloric acid (HCl) were purchased from EMD Millipore Company. Phosphoric acid (H_3PO_4, 85%) was purchased from J.T.Baker. All the chemicals in this study were used without further purification.

4.2.2. Collection of porous CNPs

Nickel foam was consecutively sonicated in 1 M HCl solution, acetone, ethanol and deionized water each for 15 min, and then used as the substrate to collect CNPs. The pre-treated nickel foam was then held above the flame of a burning paraffin candle for 30s and a layer of dark soot coating was generated on its surface (Figure 4.1a). The morphology of the CNPs coating was characterized using a JEOL JSM-7600F high-resolution field emission scanning electron microscope (FE-SEM). The size of CNPs was characterized on a submicron particle sizer (NICOMP 380) using the dynamic light scattering (DLS) technique. The CNPs were dispersed in water and sonicated for 60 minutes before the DLS test. Sodium dodecylbenzenesulfonate was used as the surfactant to improve CNP dispersion in water. The CNPs were also collected on a clean silicon wafer for the Raman measurement using a Nicolet NXR 9650 FT-Raman spectrometer.

4.2.3. Synthesis of CNPs/PANI and CNPs/MnO_2 composites

To electrochemically deposit PANI on the CNPs, a piece of CNPs-coated nickel foam (2 cm × 1 cm) was immersed into an aqueous solution of 0.1 M aniline and 1 M H2SO4. This nickel foam was used as the working electrode during the electrochemical deposition process, and a platinum mesh and a saturated calomel electrode (SCE) were used as the counter electrode and the reference electrode, respectively. The current for the oxidation of aniline was set constant at 2 mA/cm^2 and the process lasted for 10 minutes. The MnO_2 nanoparticles were galvanostaticly deposited using the same experimental setup as used in the PANI deposition. The process was carried out in an aqueous solution of 20 mM $Mn(NO_3)_2$ and 100 mM $NaNO_3$. The current for anodic electrochemical deposition was set constant at 0.5 mA/cm^2 and the process lasted for 10 minutes. All the samples were thoroughly washed with deionized water after deposition to remove remaining solution and then dried at 70 °C overnight for further characterization. Using the above conditions, CNPs were found to account for approximately 5 wt.% of the produced CNPs/PANI or CNPs/MnO_2 composites.

In order to investigate the function of the CNPs in the electrodes, both PANI and MnO_2 were also directly electrodeposited on bare nickel foam under the same conditions, and the electrochemical properties of the products were tested and compared with the ones with CNPs.

4.2.4. Electrochemical characterization

Cyclic voltammetry (CV) tests were performed on a Reference 600 potentiostat/galvanostat (Gamry instruments) at different scan rates (10~50 mV/s) between 0 and 0.8 V. 1 M Na_2SO_4 aqueous solution was used as the electrolyte for all the tests. The specific capacitances (Csp) were calculated from the obtained CV curves using the following equations:[27]

$$C_{sp} = \frac{\int i du}{2wv\Delta V}$$

where i and u are the instant current and instant potential, respectively. w is the mass of active materials on the electrodes, v is the scan rate, and ΔV is the difference in voltage at the start and the end of a scan cycle.

The specific capacitance was also calculated based on the results from cyclic charge-discharge (CCD) tests using:

$$C_{sp} = \frac{I\Delta t}{w\Delta V}$$

where I is the charge/discharge current, Δt is the time for a full discharging process, w is the mass of the active materials on the electrodes, and ΔV is the voltage window in the CCD tests. The CCD tests were carried out at current densities from 1 A/g to 5 A/g at the voltage window from 0 V to 0.8 V. The energy density (De) and power density (Dp) of the electrodes were calculated based on the CCD test results:

$$D_e = \frac{1}{2} C_{sp} (\Delta V)^2$$

$$D_p = \frac{D_e}{\Delta t}$$

To test the cyclic stability of the electrodes, the CCD test are conducted at 5 A/g for 5000 cycles and the capacitance of the electrodes after different numbers of charge-discharge cycles was calculated. The electrochemical impedance spectroscopy (EIS) analysis was performed using the Reference 600 potentiostats within the 0.01 to 100K Hz frequency range under open circuit potential with a perturbation of 5 mV.

4.2.5. Fabrication of solid-state flexible supercapacitor

H_3PO_4/PVA gel was used as the electrolyte to prepare a solid-state supercapacitor. In a typical process, 5 g PVA was added into 50 ml deionized water under vigorous stirring at 90 ℃ until the solution became clear, then 5 g H_3PO_4 was added and the stirring was continued for 30 minutes. The nickel foam finished with CNP and PANI depositions was dipped (half-length) into the electrolyte solution while the electrolyte was still hot for 10 minutes. The electrode soaked with the electrolyte solution was then air-dried at room temperature for 4 h. A piece of copper foam with the same size was also soaked with the electrolyte using the same method, and it was used as the counter electrode of the device. A piece of filter paper (Whatman CFP4) soaked with the electrolyte was placed between the two electrodes to prevent short circuit. The soaked parts of the two electrodes were pressed together under a pressure of ca. 10 MPa for 10 minutes and this compressed structure was sealed in a laminating pouch purchased at a local office supply store. The uncoated parts of the two electrodes were left out of the pouch for connection.

4.3. Results and discussions

4.3.1. Structure of CNPs/PANI electrodes

Figure 4.1a shows that CNPs are being deposited on a piece of cleaned nickel foam by placing the foam above a paraffin candle flame. The surface of the nickel foam turned black in about 30 s after a uniform coating of CNPs was created. The thickness of the coating increased as the collecting time increased. However, due to relatively weak physical interactions among the particles in the as-generated network structure, thick coatings were fragile and prone to damage, and therefore a thin coating collected within 30 s was chosen for further experiments. The nickel foam retains its high flexibility and conductivity after being coated with CNPs, and can be folded and twisted without damaging the structure of the electrode (Figure 4.1b). Figures 4.1c and 4.1d show the SEM images of the CNPs at high and low magnifications, revealing a loose, fractal-like network formed by particles with a typical diameter less than 50 nm. The particle size measured by the DLS method shows a mean diameter of 37.2 nm, with a standard deviation of 23.5 nm and

χ^2 of 0.34. The relatively wide size distribution is considered to be caused by some degree of CNP agglomeration in water despite the use of the surfactant.

The interconnected open pores shown in Figures 4.1c and 4.1d facilitate electrolyte diffusion and fast ion transportation, which is crucial to fast charge/discharge and high double-layer capacitance. Further, the CNPs can also serve as a high surface area support and a current collector for electroactive materials that promote capacitor performance by offering additional pseudocapacitance.[28] Therefore, in this study PANI nanorods were grown on the surface of the CNP porous structure by electrochemical deposition to further increase its surface area and to render pseudocapacitance.

The Raman spectrum of the CNPs shows the presence of both the D band (1343 cm-1) and the G band (1588 cm-1) at almost equal intensity and comparable width (Figure 4.1f). The peak width, peak intensity and intensity ratio of the two bands are often used to indicate the level of structural order of carbon materials, with the G band representing graphitic carbon and the D band suggesting defects in the graphene structure. The equal intensity and comparable width for the CNPs indicate ample presence of non-graphitic carbon in the material.[29, 30]

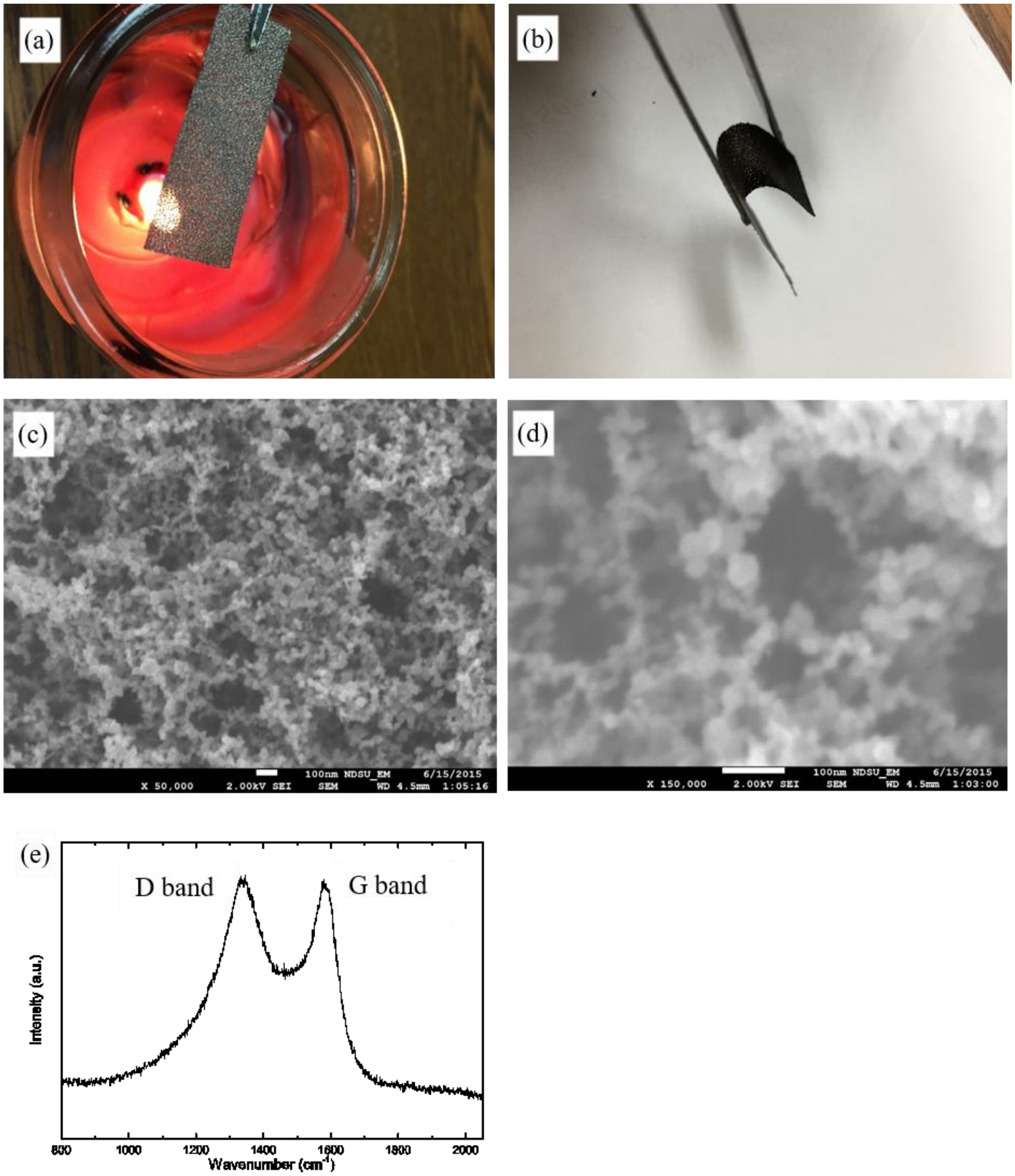

Figure 4.1. Preparation and structure of the CNP-coated nickel foam. (a) A piece of nickel foam being placed about 2 cm above a paraffin flame for CNP deposition. (b) Demonstration of the flexibility of the CNPs-coated nickel foam. (c) Low and (d) high magnification SEM images of the CNP network deposited on the nickel foam. (e) Raman spectrum of the CNPs.

Figure 4.2 shows the structure of the CNP networks after PANI was deposited. In Figure 4.2a PANI nanorods randomly grow on the CNP surface, resulting in a second layer of 3D network structure; in Figure 4.2b multiple PANI nanorods grow from a single nucleus, forming a star shaped structure with a large surface area, which should facilitate the redox reactions between PANI and electrolytes. Figures 4.1 and 4.2 together show that the CNP/PANI electrode developed in this study possesses a hierarchical, highly porous network structure that is very suitable for charge storage and flow.

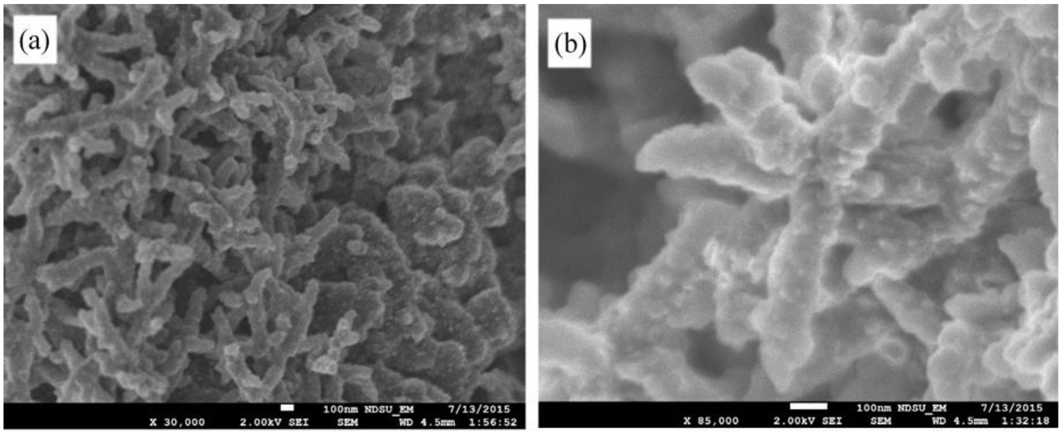

Figure 4.2. Hierarchical porous structure formed by PANI nanorods grown on the CNP network. SEM images of the structure at (a) Low and (b) high magnifications.

4.3.2. Electrochemical properties

The CNPs/PANI composites studied in the last section were dried overnight and then used directly as supercapacitor electrodes without using any binder materials or conductive additives. Cyclic voltammetry (CV), cyclic charge-discharge (CCD) tests and electrochemical impedance spectroscopy (EIS) were used to characterize their electrochemical performances as electrodes. All experiments were carried out using 1M Na_2SO_4 solution as the electrolyte, saturated calomel electrode (SCE) as the reference electrode and Pt mesh as the current collector. As shown in Figure 4.3a, a pair of redox peaks appear on the CV curve at a low scan rate (10 mV/s), indicating the existence of redox reactions resulted from Faradaic transformation of the emeraldine–pernigraniline forms of PANI during the charge and discharge process.[31-33] As the scan rate increases the shape of the CV curve is distorted and the cathodic peak (Peak C) shifts in the positive direction and the anodic peaks (Peak A) shifts in the negative direction, which is mainly related to the internal resistance of the electrode due to relatively large PANI particle size.[34] The specific capacitance calculated by the CV curve at 10 mV/s is 147 F/g, and the value decreases as the scan rate increases, which is a typical phenomenon of supercapacitors caused by the nonzero time constant and elevated transient current.[35]

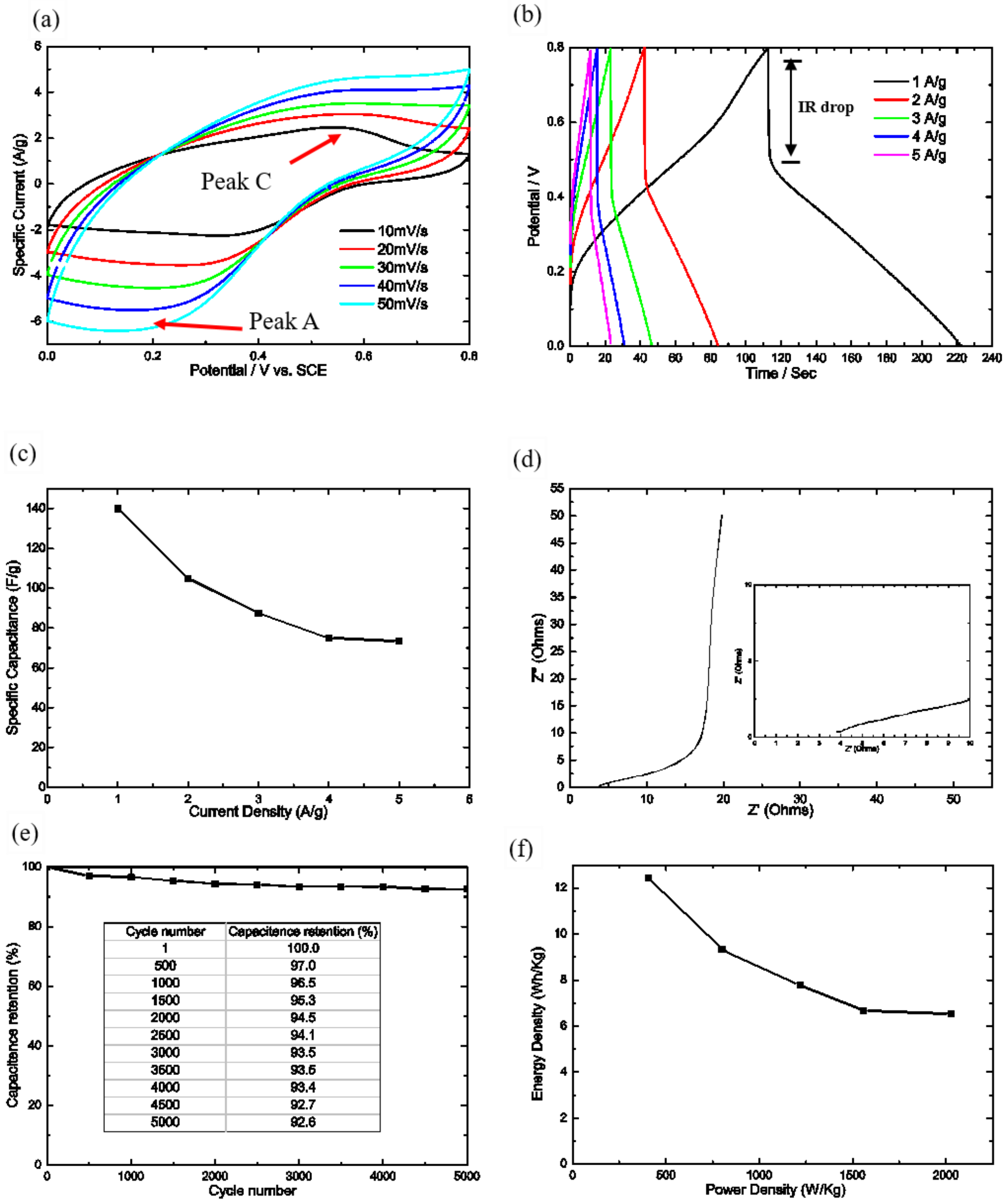

Cycle number	Capacitence retention (%)
1	100.0
500	97.0
1000	96.5
1500	95.3
2000	94.5
2500	94.1
3000	93.5
3500	93.6
4000	93.4
4500	92.7
5000	92.6

Figure 4.3. Electrochemical properties of the CNPs/PANI electrode. (a) CV plots at different scan rates. (b) CCD plots at different current densities. (c) Specific capacitance vs. current density. (d) Nyquist plot. (e) Capacitance retention over 5000 charge-discharge cycles at a current density of 5 A/g. (f) Ragone plot at different current densities.

The CCD curves (Figure 4.3b) are non-linear and quasi-symmetrical due to the redox reaction associated with the PANI. The discharge curves of the CNPs/PANI electrode show two distinctive stages, i.e. the first one in the range from 0.8 to 0.45 V and the second one from 0.45 to 0 V. The first stage shows a large IR drop and lasts around several seconds, indicating a large internal resistance. This is because that the conductivity of PANI in its leucoemeraldine or pernigraniline form is low, so the supercapacitor based on the CNPs/PANI composites has a large internal resistance when it is fully charged or discharged.[36, 37] In addition, the relatively high contact resistance between the loosely packed CNPs also contributes to this large drop. The second stage with a much longer discharge time can be ascribed to a combination of the EDLC behavior of the CNPs and the pseudo-capacitive behavior of the PANI.[38, 39] The specific capacitance calculated by the CCD curves is around 140 F/g at the charge/discharge rate of 1 A/g, which agrees well with the value calculated by the CV curve. The specific capacitance shows a 42% decrease as the charge/discharge current density increases from 1 A/g to 5 A/g (Figure 4.3c), indicating a relatively poor performance at high current. The decrease of the specific capacitance at high current densities is possibly caused by the lack of sufficient involvement of the electro-active materials in the Faradaic reactions at high charge–discharge rates.[40]

An EIS analysis was used to investigate the electrochemical performance of the CNPs/PANI electrode in more detail, including its frequency dependence, capacitance properties, and the equivalent series resistance (ESR). The Nyquist plot (Figure 4.3d) of the electrode shows that the curve increases sharply and becomes almost perpendicular to the real axis in the low-frequency region, which indicates a typical capacitive behavior. In the high frequency region, its intersection with the real axis represents the ESR derived from ionic resistance of electrolytes, intrinsic resistance of substrates, contact resistance at the interface of active material/current collector, etc.[41] The intercept of the Nyquist plot with the X-axis at high frequency region is around 3Ω, indicating a relatively large ESR that may lead to noticeable energy dissipation during the charge/discharge processes. The Warburg resistance, which is represented by the portion with a 45° slope on the curve, can be found in the middle-frequency region and is resulted from the frequency dependence of ion diffusion/transport in the electrolyte.[42]

The CNPs/PANI-based electrodes also show excellent durability. Figure 4.3e shows that the electrode retains nearly 92% of its initial capacitance after 5000 charge–discharge cycles at a current density of 5 A/g, demonstrating high stability of the materials and the structure of the electrode even at a high current density. As a widely used characterization method to evaluate the performance of energy storage devices, the Ragone plot of the electrode is provided in Figure 4.3f by plotting the energy densities versus the power densities at different current densities. The plot shows that the electrode exhibits high power densities up to 2000 W/Kg, which is much larger than that of conventional batteries such as lithium ion batteries.[43]

We also attempted to measure the electrochemical properties of the electrodes that were produced by direct electrodeposition of PANI on bare nickel foam. However, the PANI produced this way exhibited poor structural stability and detached easily from the nickel foam when the electrode underwent DI water rinse. Therefore, it is impractical to use this product to fabricate the electrodes of supercapacitors.

For comparison, MnO_2 nanoparticles were also anodically electrodeposited onto the CNPs to produce CNPs/MnO_2 electrodes. Unlike the smooth MnO_2 particles synthesized using templates such as triblock polymer P123,[44] the surface of the electrodeposited MnO_2 particles showed high roughness due to the numerous protruding MnO_2 nanosheets (Figures 4.4a and 4.4b, which are only a few nanometers in thickness and exhibit many wrinkles and ripples. This morphology can effectively improve the contact area between the MnO_2 nanocrystals and electrolytes, and therefore boost the electrochemical reactions. It should be noted that without the CNPs as the network for the MnO_2 particles to be deposited on, the MnO_2 particles tend to grow unevenly on the bare nickel foam and result in a non-uniform coating (Figure 4.4c). This phenomenon can severely affect the effective contact area between the active materials and the electrolyte, thus impacting the electrochemical performance of the electrodes. This effect can be clearly seen from the capacitance comparison below.

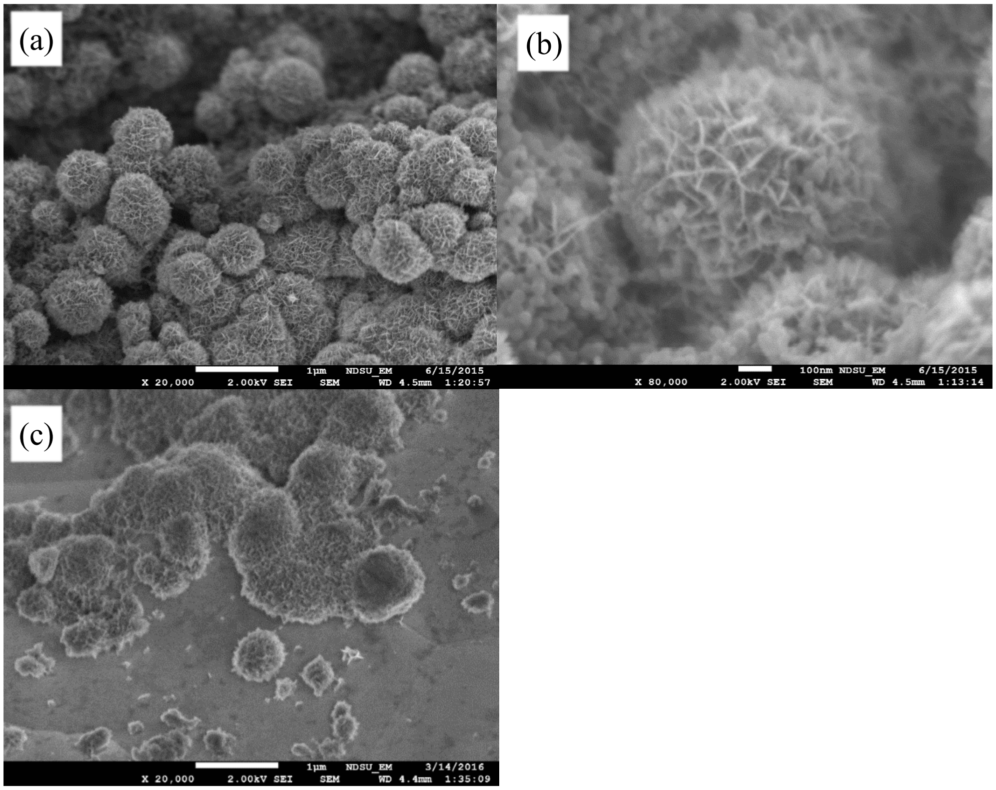

Figure 4.4. SEM images of the MnO_2 particles anodically electrodeposited on the CNP network at (a) Low and (b) high magnifications. (c) Non-uniform deposition of MnO_2 particles on the bare nickel foam.

To compare the performance of CNPs/MnO_2 with that of CNPs/PANI, the same electrochemical tests were performed. The CV curves of CNPs/MnO_2 measured within a potential window of 0~0.8 V (Figure 4.5a) show a typical rectangular shape without obvious distortion even at a high scan rate of 50 mV/s, indicating an ideal capacitive behavior resulted from a reversible reaction of the active materials of the electrode. Unlike the CV curves of the CNPs/PANI electrodes, the relatively flat curves of the CNPs/MnO_2 electrodes without any obvious redox peaks confirms that this kind of supercapacitors are charged and discharged at a pseudo-constant rate over the entire voltammetric cycles.[45] In the CNPs/MnO_2 electrodes, CNPs act as a flexible conductive scaffold and the MnO_2 nanosheets render pseudocapacitance to the electrodes. Similar to CNPs/PANI, the specific capacitance of CNPs/MnO_2 decreases with increasing scan rate, ranging from 96 F/g at 10 mV/s to 75 F/g at 50 mV/s (Figure 4.5b). However, the decrease is much smaller than that of CNPs/PANI (Figure 4.3c).

The CCD curves obtained at different current densities (1~5 A/g) exhibit isosceles triangles, which indicate ideal capacitive behavior and confirm the result from the CV tests (Figure 4.5c). Moreover, no discernible IR drop can be found on both the charge and discharge curves at even the highest current density, suggesting low energy dissipation of the capacitor, which is of great importance for energy storage devices because it causes heat generation during charge/discharge. The specific capacitance calculated by the CCD curve is 99 F/g at the charge/discharge rate of 1 A/g, which agrees well with the value calculated by the CV curve. Both the CV and CCD plots indicate that the CNPs/MnO_2 electrodes are more suitable for applications that require high current densities because their capacitive performance does not deteriorate as much as CNPs/PANI does under increasing current densities. The Nyquist plot from EIS test (Figure 4.5d) shows a straight and nearly vertical line in the low-frequency region, indicating characteristic capacitive behavior for supercapacitors.

The capacitance retention of the CNPs/MnO_2 electrodes is 85% after 5000 charge–discharge cycles, which is slightly lower than that of the CNPs/PANI electrodes (Figure 4.5e). The

Ragone plot shows that their power density can also reach a maximum value of 2000 W/Kg, similar to that of the CNPs/PANI electrodes (Figure 4.5f).

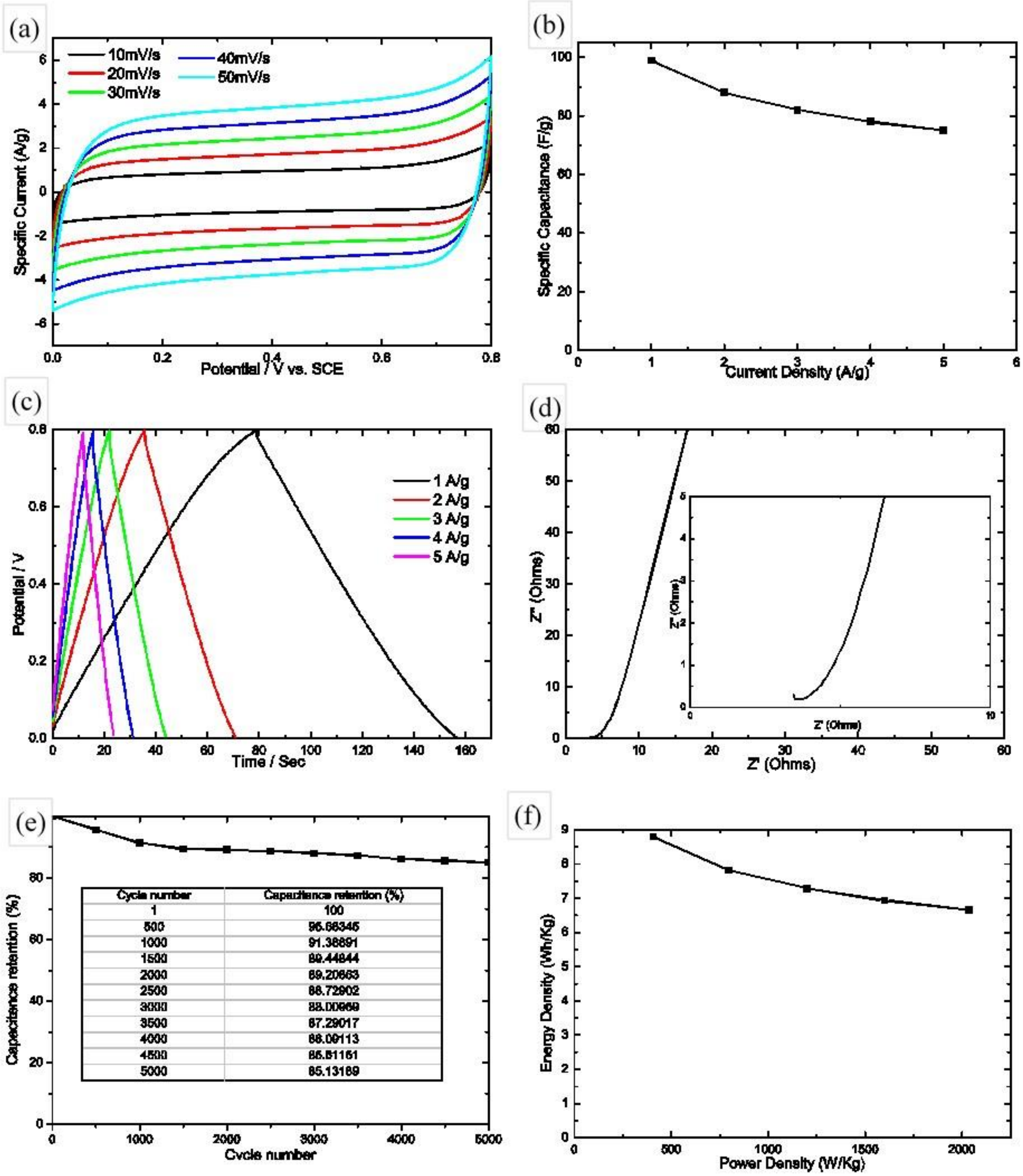

Cycle number	Capacitance retention (%)
1	100
500	95.66345
1000	91.36891
1500	89.44844
2000	89.20663
2500	88.72902
3000	88.00969
3500	87.29017
4000	86.09113
4500	85.61161
5000	85.13169

Figure 4.5. Electrochemical properties of the CNPs/ MnO_2 electrode. (a) CV plots at different scan rates. (b) CCD plots at different current densities. (c) Specific capacitance vs. current density for the electrode. (d) Nyquist plot. (e) Capacitance retention of the electrode over 5000 charge-discharge cycles at a current density of 5 A/g. (f) Ragone plot at different current densities.

Direct electrodeposition of MnO_2 on bare nickel foam results in large MnO_2 particles unevenly deposited the nickel foam surface (Figure 4.4c). This result shows that the pre-deposited CNPs play an important role in producing an even, fine MnO_2 coating on the foam. The capacitance of this CNPs-free electrode is only 32% of that of the CNPs/MnO_2 electrode, which is most likely caused by the reduced surface area and the lack of the porous CNP nanostructure.

A number of solid-state supercapacitors using CNPs/PANI as the electrodes and H_3PO_4/PVA ion gel as the electrolyte were fabricated to demonstrate the flexibility of the electrodes and their practical applications in energy storage devices. A schematic of the supercapacitor is shown in Figure 4.6a. Figure 4.6b shows that the supercapacitor is highly flexible and lightweight, and can be twisted and bended without losing structural integrity of the device. In Figure 4.6c, a LED lights up when it is powered by three of the solid-state flexible supercapacitors connected in series. It should be noted that the illumination was not disturbed when the capacitors were bended or twisted. This demonstration shows promising potentials of the candle soot based carbon nanoparticles in flexible supercapacitors.

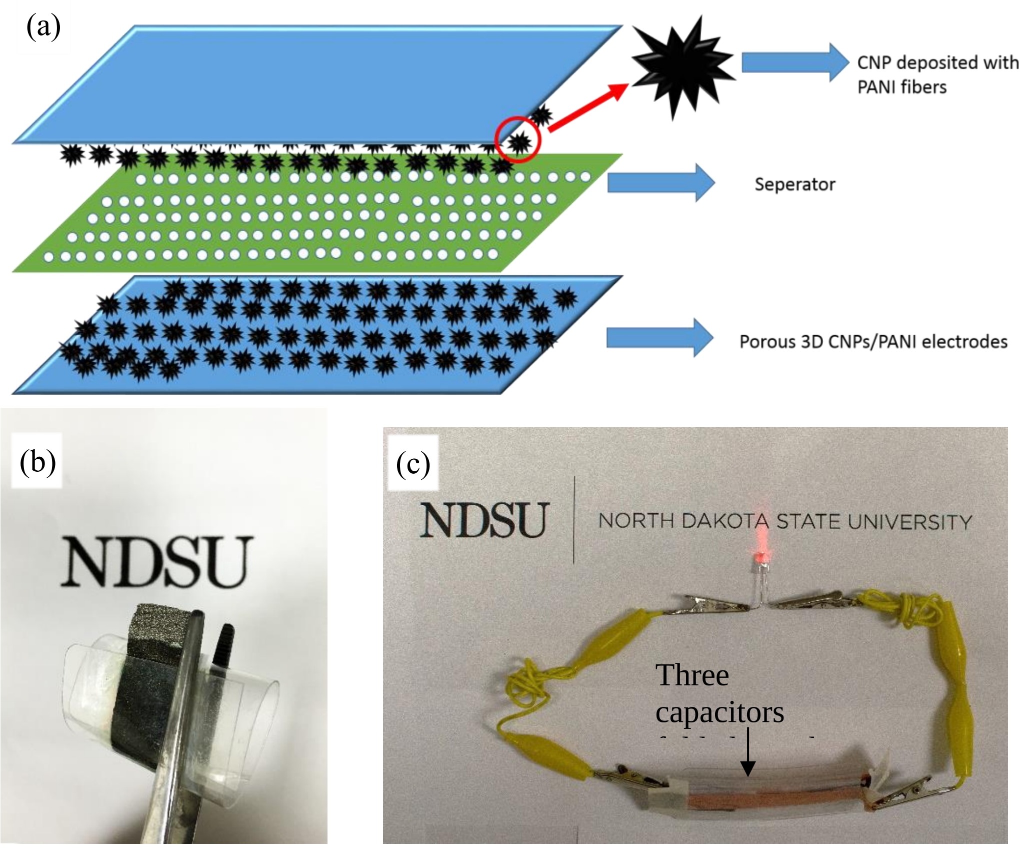

Figure 4.6. (a) Schematic illustration of the structure of a supercapacitor using CNPs/PANI as electrodes. (b) Demonstration of the flexibility of the solid-state supercapacitor. (c) Three of the flexible supercapacitors connected in series light up a LED.

4.4. Conclusions

In this study CNPs were generated by incomplete combustion of paraffin wax and PANI fibers were galvanostatically deposited on the surface of the CNPs. The CNPs/PANI composites showed interconnected 3D porous structure featuring star-like PANI fibers. As a comparative study, CNPs/MnO_2 composites were also produced using the same method and the deposited MnO_2 spheres exhibited numerous nanosheets on their surfaces. The CV curves of CNPs/PANI electrodes showed noticeable cathodic and anodic peaks, while the CNPs/MnO_2 electrodes showed a rectangular shape. The CNPs/PANI electrodes showed a high specific capacitance of 140 F/g at the current density of 1 A/g, but the value decreased markedly at high scan rates and high current densities. On the other hand, although the capacitance of CNPs/MnO_2 electrodes were lower than that of CNPs/PANI, its deterioration with increasing scan rate and current density was much more limited. Both electrodes can find suitable applications in flexible supercapacitors according to their distinctive advantages and disadvantages.

4.5. References

1. Su, Z.; Zhou, W.; Zhang, Y. *Chemical Communications* **2011,** 47, (16), 4700-4702.

2. Pagels, J.; Wierzbicka, A.; Nilsson, E.; Isaxon, C.; Dahl, A.; Gudmundsson, A.; Swietlicki, E.; Bohgard, M. *Journal of Aerosol Science* **2009,** 40, (3), 193-208.

3. Lewtas, J. *Mutation Research/Reviews in Mutation Research* **2007,** 636, (1–3), 95-133.

4. Isaxon, C.; Gudmundsson, A.; Nordin, E. Z.; Lönnblad, L.; Dahl, A.; Wieslander, G.; Bohgard, M.; Wierzbicka, A. *Atmospheric Environment* **2015,** 106, 458-466.

5. Yuan, L.; Tao, Y.; Chen, J.; Dai, J.; Song, T.; Ruan, M.; Ma, Z.; Gong, L.; Liu, K.; Zhang, X.; Hu, X.; Zhou, J.; Wang, Z. L. *Advanced Functional Materials* **2011,** 21, (11), 2150-2154.

6. Zhang, B.; Wang, D.; Yu, B.; Zhou, F.; Liu, W. *RSC Advances* **2014,** 4, (6), 2586-2589.

7. Tian, L.; Ghosh, D.; Chen, W.; Pradhan, S.; Chang, X.; Chen, S. *Chemistry of Materials* **2009,** 21, (13), 2803-2809.

8. Deng, X.; Mammen, L.; Butt, H.-J.; Vollmer, D. *Science* **2012,** 335, (6064), 67-70.

9. Yang, K.; Zhu, L.; Xing, B. *Environmental Science & Technology* **2006,** 40, (6), 1855-1861.

10. Li, H.; Zhai, J.; Tian, J.; Luo, Y.; Sun, X. *Biosensors and Bioelectronics* **2011,** 26, (12), 4656-4660.

11. Li, H.; Zhai, J.; Sun, X. *Langmuir* **2011,** 27, (8), 4305-4308.

12. Tan, M.; Zhang, L.; Tang, R.; Song, X.; Li, Y.; Wu, H.; Wang, Y.; Lv, G.; Liu, W.; Ma, X. *Talanta* **2013,** 115, 950-956.

13. Liu, H.; Ye, T.; Mao, C. *Angewandte Chemie International Edition* **2007,** 46, (34), 6473-6475.

14. Liu, X.; Xu, Y.; Ben, K.; Chen, Z.; Wang, Y.; Guan, Z. *Applied Surface Science* **2015,** 339, 94-101.

15. Sahoo, B. N.; Balasubramanian, K.; Sucheendran, M. *The Journal of Physical Chemistry C* **2015,** 119, (25), 14201-14213.

16. Karthik, N.; Sethuraman, M. G. *New Journal of Chemistry* **2015,** 39, (5), 3337-3340.

17. Miller, J. R.; Simon, P. *Science* **2008,** 321, (5889), 651-652.

18. He, Y.; Chen, W.; Gao, C.; Zhou, J.; Li, X.; Xie, E. *Nanoscale* **2013,** 5, (19), 8799-8820.

19. Wang, G.; Zhang, L.; Zhang, J. *Chemical Society Reviews* **2012,** 41, (2), 797-828.

20. Lu, Q.; Chen, J. G.; Xiao, J. Q. *Angewandte Chemie International Edition* **2013,** 52, (7), 1882-1889.

21. Pandolfo, A. G.; Hollenkamp, A. F. *Journal of Power Sources* **2006,** 157, (1), 11-27.

22. Yuan, L.; Lu, X.-H.; Xiao, X.; Zhai, T.; Dai, J.; Zhang, F.; Hu, B.; Wang, X.; Gong, L.; Chen, J.; Hu, C.; Tong, Y.; Zhou, J.; Wang, Z. L. *ACS Nano* **2012,** 6, (1), 656-661.

23. Snook, G. A.; Kao, P.; Best, A. S. *Journal of Power Sources* **2011,** 196, (1), 1-12.

24. Male, U.; Srinivasan, P. *Journal of Applied Polymer Science* **2015,** 132, (37), n/a-n/a.

25. Olad, A.; Gharekhani, H. *Progress in Organic Coatings* **2015,** 81, 19-26.

26. Chen, W.; Rakhi, R. B.; Hu, L.; Xie, X.; Cui, Y.; Alshareef, H. N. *Nano Letters* **2011,** 11, (12), 5165-5172.

27. Zhang, L. L.; Zhao, X. S. *Chemical Society Reviews* **2009,** 38, (9), 2520-2531.

28. Fan, L. Z.; Hu, Y. S.; Maier, J.; Adelhelm, P.; Smarsly, B.; Antonietti, M. *Advanced Functional Materials* **2007,** 17, (16), 3083-3087.

29. Gogotsi, Y.; Libera, J. A.; Kalashnikov, N.; Yoshimura, M. *Science* **2000,** 290, (5490), 317-320.

30. Vinayan, B. P.; Nagar, R.; Raman, V.; Rajalakshmi, N.; Dhathathreyan, K. S.; Ramaprabhu, S. *Journal of Materials Chemistry* **2012,** 22, (19), 9949-9956.

31. Yang, J. E.; Jang, I.; Kim, M.; Baeck, S. H.; Hwang, S.; Shim, S. E. *Electrochimica Acta* **2013,** 111, 136-143.

32. Wang, K.; Meng, Q.; Zhang, Y.; Wei, Z.; Miao, M. *Advanced Materials* **2013,** 25, (10), 1494-1498.

33. Wang, D.-W.; Li, F.; Zhao, J.; Ren, W.; Chen, Z.-G.; Tan, J.; Wu, Z.-S.; Gentle, I.; Lu, G. Q.; Cheng, H.-M. *ACS Nano* **2009,** 3, (7), 1745-1752.

34. Yan, J.; Fan, Z.; Sun, W.; Ning, G.; Wei, T.; Zhang, Q.; Zhang, R.; Zhi, L.; Wei, F. *Advanced Functional Materials* **2012,** 22, (12), 2632-2641.

35. Prabaharan, S. R. S.; Vimala, R.; Zainal, Z. *Journal of Power Sources* **2006,** 161, (1), 730-736.

36. Fan, W.; Zhang, C.; Tjiu, W. W.; Pramoda, K. P.; He, C.; Liu, T. *ACS Applied Materials & Interfaces* **2013,** 5, (8), 3382-3391.

37. Wang, K.; Wu, H.; Meng, Y.; Zhang, Y.; Wei, Z. *Energy & Environmental Science* **2012,** 5, (8), 8384-8389.

38. Li, L.; Song, H.; Zhang, Q.; Yao, J.; Chen, X. *Journal of Power Sources* **2009,** 187, (1), 268-274.

39. Wu, Q.; Xu, Y.; Yao, Z.; Liu, A.; Shi, G. *ACS Nano* **2010,** 4, (4), 1963-1970.

40. Jana, M.; Kumar, J. S.; Khanra, P.; Samanta, P.; Koo, H.; Murmu, N. C.; Kuila, T. *Journal of Power Sources* **2016,** 303, 222-233.

41. Gao, H.; Xiao, F.; Ching, C. B.; Duan, H. *ACS Applied Materials & Interfaces* **2012,** 4, (5), 2801-2810.

42. Mao, L.; Zhang, K.; On Chan, H. S.; Wu, J. *Journal of Materials Chemistry* **2012,** 22, (1), 80-85.

43. Wei, D.; Scherer, M. R. J.; Bower, C.; Andrew, P.; Ryhänen, T.; Steiner, U. *Nano Letters* **2012,** 12, (4), 1857-1862.

44. Wang, P.; Zhao, Y.-J.; Wen, L.-X.; Chen, J.-F.; Lei, Z.-G. *Industrial & Engineering Chemistry Research* **2014,** 53, (52), 20116-20123.

45. Lang, X.; Hirata, A.; Fujita, T.; Chen, M. *Nat Nano* **2011,** 6, (4), 232-236.

5. FREESTANDING CARBON AEROGEL PRODUCED FROM BACTERIAL CELLULOSE AND ITS APPLICATION AS SCAFFOLD OF $MNO_2/NI(OH)_2$ HYBRID FOR HIGH-PERFORMANCE SUPERCAPACITOR ELECTRODES

5.1. Introduction

Cellulose, an organic compound consisting of β (1,4) linked D-glucose linear chains, is the most abundant natural polymer on earth. Due to their insolubility in water, thermal stability, high mechanical properties, high availability and low cost, cellulose-based natural materials (e.g. wood, hemp, cotton, linen, etc.) have been used for thousands of years to produce building materials, furniture, fabrics, papers, textiles, threads, etc. Cellulose is currently still among the most widely studied biopolymers as a renewable and degradable source of carbon materials.[1] Cellulose is produced on a large scale by a diverse group of organisms in nature, including plants, bacteria, algae and fungi.[2] The annual production of cellulose worldwide is around 1.5×10^{12} tons, thus it is considered to be an inexhaustible source of raw materials for renewable products.[3, 4] Most of the natural cellulose is produced by plants as it is the structural component of the protective cell walls. These plant-derived celluloses can be easily found in stalks, woods, corn stovers, cottons, hemps and so on. Additionally, cellulose can also be synthesized by several microorganisms such as *Gluconacetobacter xylinus*. The cellulose produced by these microorganisms is known as microbial cellulose or bacterial cellulose (BC).[5] BC is chemically identical with the cellulose in the cell walls of plants, but in contrast with the plant-derived cellulose which is heterogeneous and difficult to purity, BC is free from lignin, hemicellulose and other biopolymers that exist in the cell walls.[6] Besides its purity, BC also has many distinctive properties such as high crystallinity[5], high mechanical strength[7], high water holding capacity[8] and outstanding biocompatibility[9]. BC has a unique three-dimensional (3D) network structure formed by ultrafine cellulose fibers, which can be used to produce 3D ultra-lightweight aerogels.[10] The excellent biocompatibility of BC makes it ideal for biomedical application such as skin tissue repair. Besides, the commercialization of BC for application in drug delivery systems shows a promising future.[11, 12] In the field of nanomaterials, it has been reported that highly conductive and flexible carbon aerogels (CA) can be produced from lyophilized BC aerogels by pyrolysis in an inert atmosphere such as argon or nitrogen.[13] Despite recent progress in this field, the potential applications of BC still need further investigation.

The characteristics of cellulose provide the material great potential for producing low cost and environmentally friendly flexible electronic devices. For example, it has been reported recently that a portable, recyclable and highly selective cellulose-based sensor device was successfully developed for the colorimetric and optical detection of hydrogen sulfate anions in water.[14] Cellulose-based materials was also used to make microfluidic devices due to its excellent absorptivity and permeability, and these devices can be used as novel diagnostic platforms for chemistry, biochemistry, and environmental studies.[15] Membranes produced from BC were used as flexible substrates for the organic light emitting diodes (OLED), which offered a new way to fabricate flexible organic optoelectronic devices.[16] Among all these applications, it should be noted that the porous, hydrophilic properties of BC and its 3D network structure are particularly suitable for the electrodes in energy storage devices such as batteries and supercapacitors.

Supercapacitors (SCs), also known as electrochemical capacitors or ultra-capacitors, are low-cost and environmentally friendly energy storage devices. SCs generally have the advantages of long cycle life, rapid charging/discharging rate and high power densities. They have the potential to meet the growing demands for power delivering systems in portable electronics, power backup systems, electrical/hybrid vehicles, etc.[17] A variety of electrode materials have been developed to increase the performance of SCs, including various forms of carbon, conducting polymers and transitional metal oxides.[18] Activated carbons (ACs) are the most commonly used carbonaceous materials for the electrodes of SCs due to their low-cost, high chemical and thermal stability, and large specific surface area.[19] The electrodes produced from ACs with a highly porous structure and a large surface area can reversibly adsorb/desorb ions of the electrolyte onto/from the active materials. Electrical charges are electrostatically stored on the electrode/electrolyte interface during the charging process, and the stored energy can be rapidly released when being discharged. This type of SCs are called electrochemical double layer capacitors (EDLCs).[20] SCs can also be achieved based on pseudo-capacitive behavior, i.e. fast and reversible redox reactions on or near the surface of the electrodes for energy storage. Compared with the EDLCs which relies solely on the electrical double layers to store energy, the active materials with pseudo-capacitive behavior usually show higher specific capacitance and energy density owing to the contribution of the interfacial reversible Faradaic reactions. These type of SCs are called pseudo-capacitors.[21] The combination of these two mechanisms increases the specific capacitance and further enhances the overall performance of SCs. Manganese dioxide (MnO_2) is one of the most popular electrode materials for SCs. Just like the carbonaceous materials such as ACs, it is also inexpensive, abundant in nature and environmentally friendly. Its theoretical capacitance can reach as high as 1370 F/ g.[22] Many methods have been proposed to produce electrode materials for SCs. Among them, the electrodeposition technique has proven to be an effect way of producing nanoscale electrode materials with high performance.[23]

Cellulose has been applied as a substrate or scaffold for the electrodes of SCs due to its high mechanical performance, flexibility, and tailorable surface functionalities.[24] Previous researches show that freestanding and flexible paper electrodes can be successfully fabricated based on BC, carbon nanotubes/graphene and polyaniline/polypyrrole composites.[25-28] In these applications, BC was employed as the template and substrate to support the electro-active materials. The composites have unique flexible mechanical properties with good bending stability, and show high electrochemical performance with specific capacitance up to ~500 F/g and energy density up to ~30 Wh/kg. Recently, BC-based gel electrolyte has also been developed to fabricate all-biomaterial derived SCs.[29] Nitrogen-doped electrode materials from pyrolyzed BC are synthesized by hydrothermal reaction between BC and aqueous ammonia solution or by annealing of BC in NH_3 atmosphere.[30, 31]

In this chapter, 3D carbon aerogels with 3D interconnected structure and increased surface area were produced by direct pyrolysis of BC without undergoing any chemical activation. The synthesis process is free from strong activation agents such as KOH or phosphoric acid that are typically used to produce high surface-area ACs. The method is environmentally-friendly and can be potentially used for large-scale industry production. The hierarchical 3D structure has large surface areas (~337m^2/g) and ample mesopores, which can provide channels for ion diffusion during the charge/discharge processes of SCs. MnO_2 and $Ni(OH)_2$ nanoparticles are coated on the surface of the carbon nanofibers via electrodeposition and redox reaction. The MnO_2 and $Ni(OH)_2$ nanoparticles serve as the active materials to promote the electrochemical performance. SCs with this 3D nanostructured electrodes were successfully fabricated and their electrochemical performances were tested. This research provides a novel method for the application of BC in energy storage devices, and can meet the growing demand for low-cost, clean and renewable material sources for advanced energy storage systems.

5.2. Experimental section

5.2.1. Materials

The commercially available food, *nata de coco* made from BC cubes, were purchased from Thai Agri Foods Public Company. The BC cubes were rinsed continuously using tap water for two days to remove the syrup contained inside the cubes, and then immersed in DI water for 15 days with the water changed every 12 h. Upon complete purification, the mass concentration of BC in the purified BC hydrogel was measured to be around 0.5%. Carbon cloth sheet, conductive carbon black (TIMCAL SUPER C45), polyvinylidene fluoride (PVDF) binder and N-methyl-2-pyrrolidone (NMP) were purchased from MTI Corporation. Nickel sulfate ($NiSO_4$), nickel chloride ($NiCl_{2.}$), boric acid (H_3BO_3) and poly (vinyl alcohol) (PVA, Mw =~31,000) were purchased from Sigma-Aldrich. Sulfuric acid (H_2SO_4, 98%) was purchased from BDH Aristar Corporation. PVC laminating sheets (Scotch LS854SS-10) were purchased from Amazon.com. All the chemicals were used without further purification.

5.2.2. Preparation of carbon aerogel from BC

The purified BC cubes were frozen in liquid nitrogen and freeze-dried at -48 °C under 0.05 mbar pressure using a freeze dryer (Freezone Freeze Dry Systems, Labconco). BC aerogels were produced after the freeze drying. The BC aerogels were pyrolyzed using a tube furnace (TF55030A Tube Furnace, Thermo Scientific) in an argon atmosphere to produce carbon aerogels (CAs). The heating rate was set at 1°C/min from room temperature to 350 °C, then the temperature was kept at 350°C for one hour. After that the temperature was increased from 350 °C to 1000°C at 5°C/min, kept at 1000 °C for 100 minutes, and then decreased to room temperature at 5°C/min. After the pyrolysis, the width of the CAs decreased to half of the original width of the BC aerogels, and the volume of the CAs was 15% of the volume of the original BC cubes. The morphology and the internal structure of the samples were characterized using high-resolution field emission scanning electron microscope (FE-SEM, JEOL JSM-7600F) and transmission electron microscopy (TEM, JEOL JEM-2100). Thermogravimetric analysis (TGA) was performed on a Q500 Thermogravimetric Analyzer (TA instruments) from 25 °C to 800 °C at a heating rate of 20 °C/min in a nitrogen flow of 60.0 ml/min. X-ray powder diffraction (XRD) analysis was performed on a Phillips X'Pert MPD Powder X-ray Diffractometer. The X-ray used for the characterization was the K_α radiation (λ=0.1541841 nm) generated from copper at 40 kV and 80 mA. The surface area and pore size distribution of the aerogels were tested by adsorption/desorption isotherms at 77K using a TriStar II 3020 Automatic Analyzer. The BC aerogels and carbon aerogels were degassed at 150 °C and 200°C respectively under vacuum overnight before measurement. Nitrogen was used as the analysis adsorptive gas in all tests.

5.2.3. Electrodeposition of nickel and formation of MnO_2/$Ni(OH)_2$ hybrid

The electrodeposition of nickel on the CAs was carried out at room temperature in a Watts nickel plating bath containing $NiSO_4$ (250g/L), $NiCl_2$ (50 g/L) and H_3BO_3 (30 g/L). The flexible CAs were tightly sandwiched between two plates of stainless steel and completely immersed in the bath. The electrodeposition process lasted for 10 minutes with a constant current density of 10 mA/cm^2. The initial pH value of the electrolyte was around 4.3. When the electrodeposition was finished, the CAs were immersed in DI water overnight and then gently rinsed to remove the remaining Watts solution. The washed CAs were immersed into 50mM potassium permanganate solution for two hours in a dark room, and then rinsed with DI water to remove the remaining potassium permanganate solution. The cleaned CAs were dried in an oven at 75°C overnight for further use.

5.2.4. Electrochemical characterization

All the electrochemical tests were performed using a three-electrodes system on a Reference 600 potentiostat/galvanostat (Gamry instruments). To prepare supercapacitor electrodes for the tests, the MnO_2/$Ni(OH)_2$ hybrid coated CA, conductive carbon black and PVDF were mixed (80:15:5 by weight) and ground thoroughly using a mortar and pestle for ten minutes. NMP was then added to the mixtures to form a slurry. The slurry was then uniformly pasted on a piece of nickel foam, and dried overnight at 75 °C to remove the NMP. The dried nickel foams loaded with electrode materials were pressed under a pressure of 10 MPa to reduce the contact resistance between the active materials and the current collectors. The mass loading of the active materials on the current collectors was around 3 mg. Cyclic voltammetry (CV) tests were performed at selected scan rates (10~50 mV/s). The voltage was swept linearly between 0 and 0.8 V versus a saturated calomel reference electrode (SCE) at room temperature. 1 M Na_2SO_4 aqueous solution was used as the electrolyte for all the tests.

The cyclic charge-discharge (CCD) tests were carried out at selected densities (1 A/g to 5 A/g) at the voltage window of 0 V~0.8 V. The specific capacitance (C_{sp}) was calculated using the following equation:

$$C_{sp} = \frac{I\Delta t}{w\Delta V}$$

where I is the charge/discharge current, Δt is the time for a full discharging process, w is the mass of the active materials on the electrodes, and ΔV is the voltage window of the CCD tests. The energy density (D_e) and power density (D_p) of the electrodes were calculated based on the CCD test results as follows:

$$D_e = \frac{1}{2} C_{sp} (\Delta V)^2$$

$$D_p = \frac{D_e}{\Delta t}$$

To test the cyclic stability of the electrodes, the CCD test are conducted at 5 A/g for 5000 cycles and the capacitance of the electrodes during the process was calculated to compare their performance. The electrochemical impedance spectroscopy (EIS) analysis was performed from 0.01 Hz to 100K Hz with a perturbation of 5 mV vs. the open circuit potential.

5.2.5. Fabrication of solid-state SCs

H_2SO_4/PVA ion gel was used as the electrolyte for the solid-state SCs. To prepare the electrolyte, 6 g PVA was added into 60 ml deionized water under vigorous stirring at 90 °C to form a clear gel, then 6 g H_2SO_4 was added into the PVA gel and the stirring was continued until a homogeneous ion gel was formed. The paste prepared for the fabrication of the electrodes were doctor-bladed on a piece of rectangular carbon cloth. The carbon cloths were immersed into the H_2SO_4/PVA ion gel and then air-dried at room temperature for 4 h. Two electrodes soaked with ion gel electrolyte were sealed in plastic laminating sheets to form a supercapacitor. To demonstrate the application as energy storage devices, three identical SCs were connected in series to form a supercapacitor pack. The pack was charged until the voltage reached 3 volts, and then connected to a LED light.

5.3. Results and discussion

The original BC hydrogels contain nearly 99% of water, indicating excellent hydrophilic properties of BC due to the large amount of hydroxyl groups on the cellulose fibers. It can be seen from Figure 5.1a that the mass of the freeze-dried BC cube (i.e. BC aerogel) with the size of ~1cm^3 is around 20mg. After the pyrolysis at 1000 °C under a constant 200 ccm argon flow, the BC aerogel is converted into a flexible, lightweight and conductive CA. The volume of the CA cube shrank to ~15% of the original BC aerogel cube, and only 10% of the original mass remains due to the removal of O and H atoms during the pyrolysis process. The weight loss and weight loss rate curves (Figures 5.1c) indicate that the major weight loss occurs between 200 °C and 400 °C. The small weight loss below 100 °C is due to the loss of moisture, and the major loss thereafter is caused by the removal of degradation volatiles in the form of CO_2, H_2O, CH_4, furans, acetaldehyde, etc.[32] During the initial stages of the pyrolysis process, intermediary anhydrocellulose is formed because of the intermolecular and intramolecular dehydration of the cellulose before 300 °C. Cellulose depolymerization occurs rapidly during 300~400 °C and volatile compounds are released. A charring process happens as the temperature continues to increase, forming aromatic benzene rings and aromatic polycyclic structure by combination of these benzene rings.[33] The released volatile compounds can also undergo secondary reactions by breaking the chemical bonds within the volatile compounds and recombining into molecules with a lower molecular weight.[34] Previous research showed that a high heating rate results in simultaneous chemical bond breakages , leading to the release of volatile compounds, while a low heating rate favors the conversion of biomass into solid residues and the production of bio-char.[33] In the case of this experiment, due to the low heating rates used (5 °C/min), the network structure of BC aerogels remains intact, resulting in stable, flexible and conductive CAs.

The surface area and pore size distribution of the aerogels were investigated by nitrogen adsorption/desorption tests. As shown in Figure 5.1d, the adsorption/desorption isotherms of the BC aerogel and CA can be characterized as type III isotherms according to the BDDT (Brunauer–Deming–Deming–Teller) classification, which describes adsorption on macroporous adsorbents with week adsorbate-adsorbent interactions.[35] Based on the BET theory, the surface areas for the BC aerogel and CA were calculated to be 146.61 m^2/g and 337.21 m^2/g, respectively. The increase of surface area was caused by the removal of volatile matter during the pyrolysis, which resulted in an increase in the pore volume and surface area.[36] The heating rate used in the experiments was very low, which grants sufficient time for the volatiles to diffuse and escape from the cellulose nanofiber[37] The small hysteresis loop in the region from $P/P_0 = 0.8$ to 1 indicates the existence of a large number of mesopores between within the 3D network.[31] The pore size distributions (Figure. 5.1e) were calculated based on the BJH theory. For both aerogels, the pores between 2 and 3 nm constitute the largest population. The average pore width is around 10 nm for the BC aerogels and 7.6 nm for CAs. The decrease of average pore size explains the shrinkage of the BC aerogels after the pyrolysis treatment. According to the previous research in chapter 2 and 3, although the increase in surface area favors the improvement of the capacitance, the pore size distribution also plays an important role for further optimization of the electrochemical performances.[19] In this research, the interconnected network with ample micropores and mesopores enable fast diffusion of electrolyte ions during the charge/discharge process especially at high current densities, which can facilitate the high-quality performance of the supercapacitors.[38]

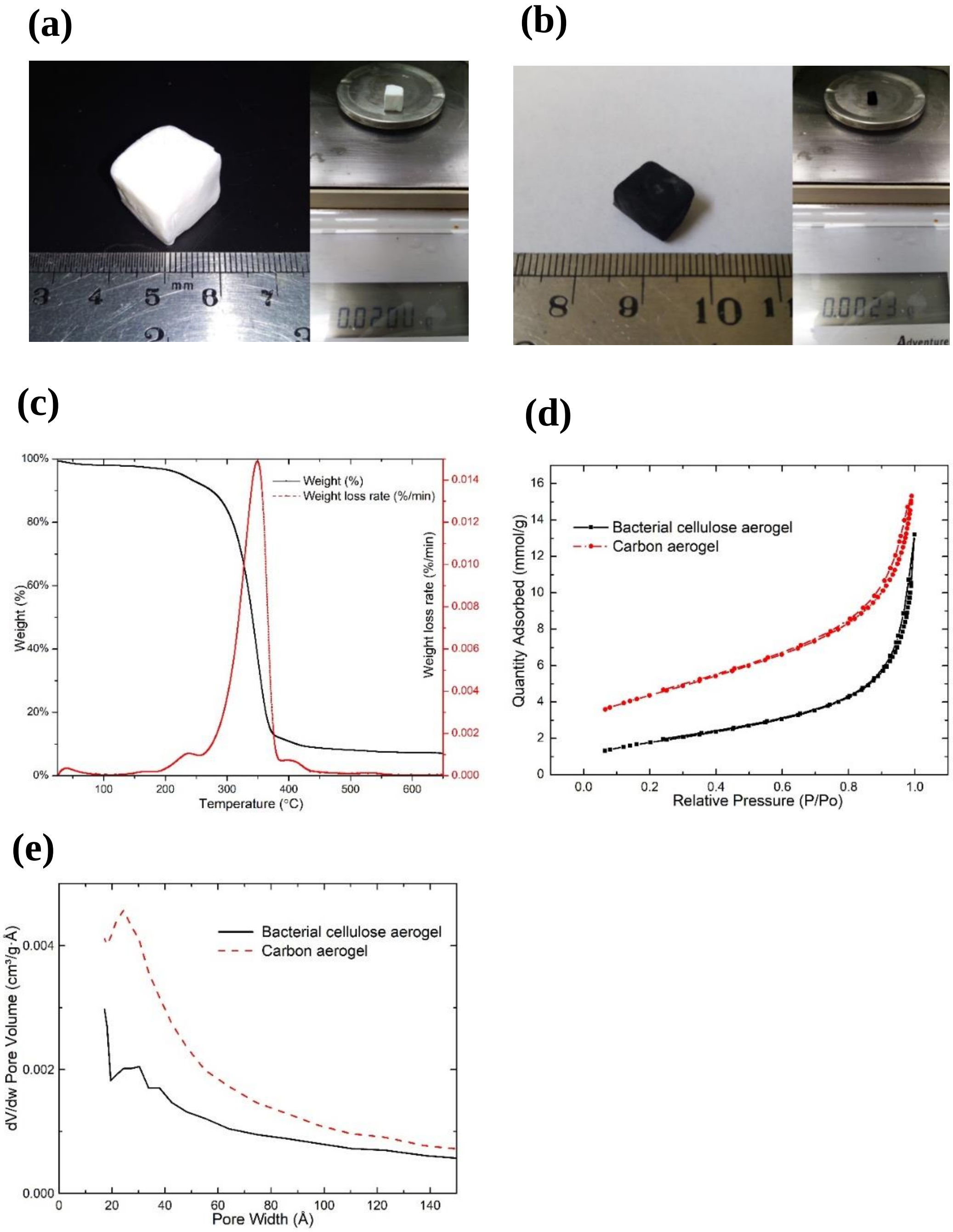

Figure 5.1. (a) Size and weight of a BC aerogel cube after freeze drying. (b) Size and weight of the CA cube after pyrolysis of the BC aerogel cube. (c) TGA results of the BC aerogels. (d) Adsorption/desorption isotherms of the BC aerogels and CAs. (e) Pore size distribution based on the BJH method.

Figure 5.2 shows the proposed scheme of nickel electrodeposition and $MnO_2/Ni(OH)_2$ hybrid formation on the CAs. In the first step nickel nanoparticles are deposited. The size and density of the nickel nanoparticles can be controlled by the current density and the duration of the electrodeposition process. In the second step, $MnO_2/Ni(OH)_2$ hybrid is produced on the nickel nanoparticle surface and a layer of MnO_2 is formed on the carbon nanofiber surface. The BC aerogel works as a scaffold to support the electrochemically active metal compounds. The introduction of MnO_2 and $Ni(OH)_2$ on the carbon 3D network should greatly improve its electrochemical performance. This proposed process is confirmed by the SEM and TEM studies discussed below.

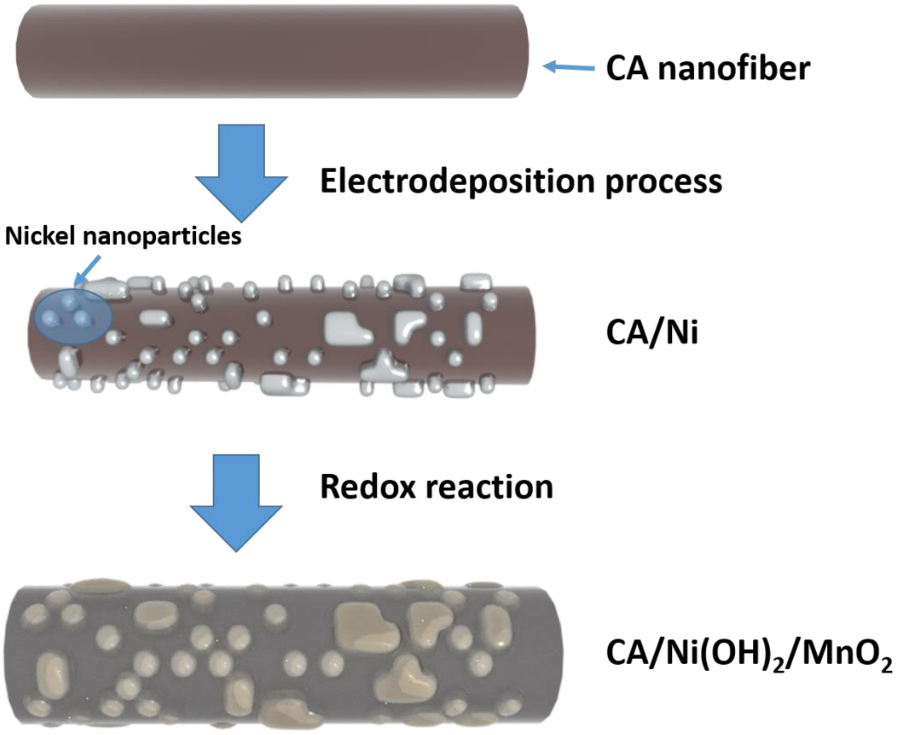

Figure 5.2. Scheme of the synthesis process of the Ni, MnO_2, and $MnO_2/Ni(OH)_2$ hybrid coating on CAs.

The SEM images of a CA at low and high magnifications are shown in Figure 5.3a and 5.3b. The carbonized BC nanofibers (average fiber diameter ~ 30 nm) form an interconnected porous network in the aerogel (Figure. 5.3b). After the two-step synthesis process, the CA retains its original porous network formed by the intertwined carbon nanofibers, but the average width of the nanofibers increases to ~50nm as shown by Figure 5.3d. The surface of the carbon nanofibers also becomes rougher after the process due to the coated materials. To investigate the composition of the aerogels, energy-dispersive X-ray spectroscopy (EDS) was used to determine the atomic percentage of the materials. The EDS results show that the atomic percentage of carbon atoms for the pure CA is 90.56%, indicating its high carbonization degree after the pyrolysis treatment. After the synthesis process, the atomic percentage of carbon atoms decreases to 81.92%, while the percentages of nickel and manganese atoms increase to 12.13% and 4.47%, respectively. The redox reaction happened between nickel and manganese permanganate can be described by the following equations:[39]

$$3Ni + 2MnO_4^- + 4H_2O = 2MnO_2 + 3Ni(OH)_2 + 2OH^-$$

The MnO_2 coating on the surface of the carbon fibers was formed by the reaction between the carbon fiber and the $KMnO_4$ solution, which can be described as follows:[40]

$$4MnO_4^- + 3C + H_2O = 4MnO_2 + CO_3^{2-} + 2HCO_3^-$$

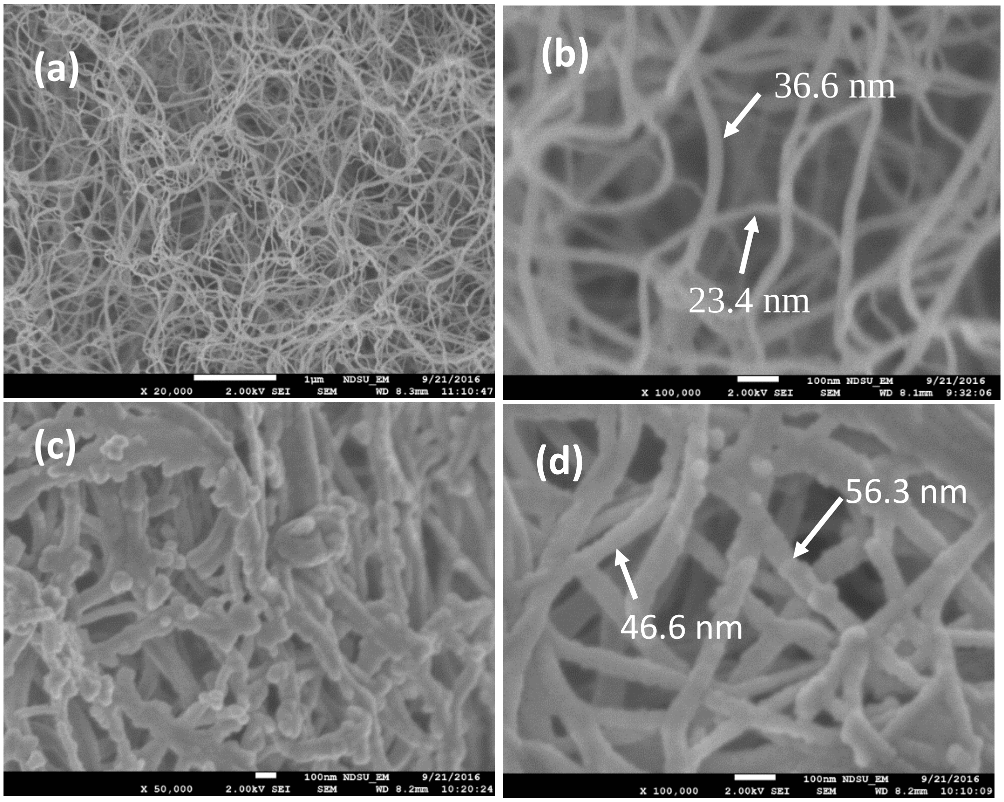

Figure 5.3. (a) and (b) SEM images of CAs at low and high magnifications. (c) and (d) SEM images of the CAs coated with Ni, MnO_2, and $MnO_2/Ni(OH)_2$ hybrid at low and high magnifications.

TEM studies were performed to determine the internal structures of the CAs after the nickel electrodeposition and the hybrid formation. As shown by Figure 5.4(a~c), nickel nanoparticles measuring about 20 nm were evenly deposited along the carbon nanofibers, which exhibit a largely amorphous structure. A crystalline lattice structure can be seen in the nickel nanoparticles, indicating the formation of metal nickel particles (Figure 5.4c). After the formation of MnO_2 and $Ni(OH)_2$, the diameter of the fibers increased significantly (Figure 5.4e). The surface of the nickel nanoparticles was also coated with $MnO_2/Ni(OH)_2$ hybrid formed by redox reaction (Figure 5.4f).

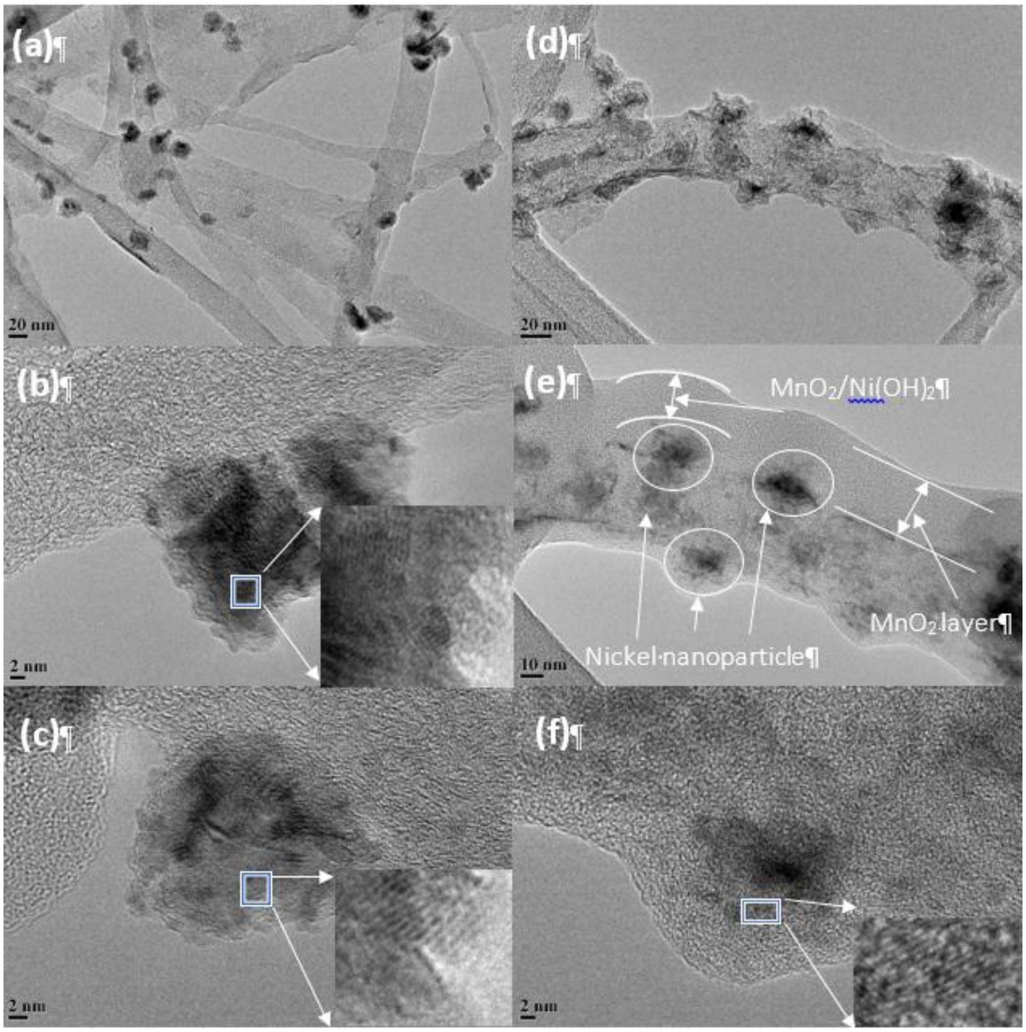

Figure 5.4. (a~c) TEM images of the CAs coated with nickel nanoparticles at low to high magnifications. (e~f) TEM images of the CAs coated with Ni/MnO_2 and MnO_2/$Ni(OH)_2$ hybrid at low to high magnifications.

The XRD patterns of the BC aerogels and CAs are shown in Figure 5.5a. The former shows three major diffraction peaks at 14.6°, 16.8° and 22.6°, which represent the (1, -1, 0), (1, 1, 0) and (2, 0, 0) plane of crystalline cellulose, respectively.[41] The obtained XRD pattern agrees well with that of type I cellulose, which is formed from unidirectionally aligned, parallel D-glucose chains.[42] The crystallinity index (I_c) can be calculated using the equation below:

$$\mathrm{I}_c = \frac{\mathrm{I}_{200} - \mathrm{I}_{am}}{\mathrm{I}_{200}}$$

where I_{200} is the intensity of the (200) peak, and I_{am} is the baseline intensity of amorphous material at 18°.[43] The BC aerogels show a high crystallinity of ~85.9%. By contrast, the XRD pattern of CAs lacks diffraction peaks, indicating their amorphous structure. This is because the carbonaceous materials generated from pyrolysis of biomass are generally hard carbons with irregular and disordered structure that are hard to be graphitized.[44, 45]

After deposition of nickel nanoparticles on the CAs, the spectrum shows two characteristic peaks at 44.5° and 51.8° (Figure 5.5b), which correspond to the (111) and (200) planes of the face-centered cubic structure of nickel.[46] After the coating of MnO_2, new peaks that represent the (301) plane of the MnO_2 and the (101) and (110) planes of the $Ni(OH)_2$ appear on the pattern.[39, 47] This result confirms the formation of the $MnO_2/Ni(OH)_2$ hybrid on the CAs. In this composite material, the porous 3d network structure offers a good tunnel for ion transfer within the carbon aerogel scaffold, while the $MnO_2/Ni(OH)_2$ hybrid functions as the electroactive materials to provide high pseudo-capacitance.

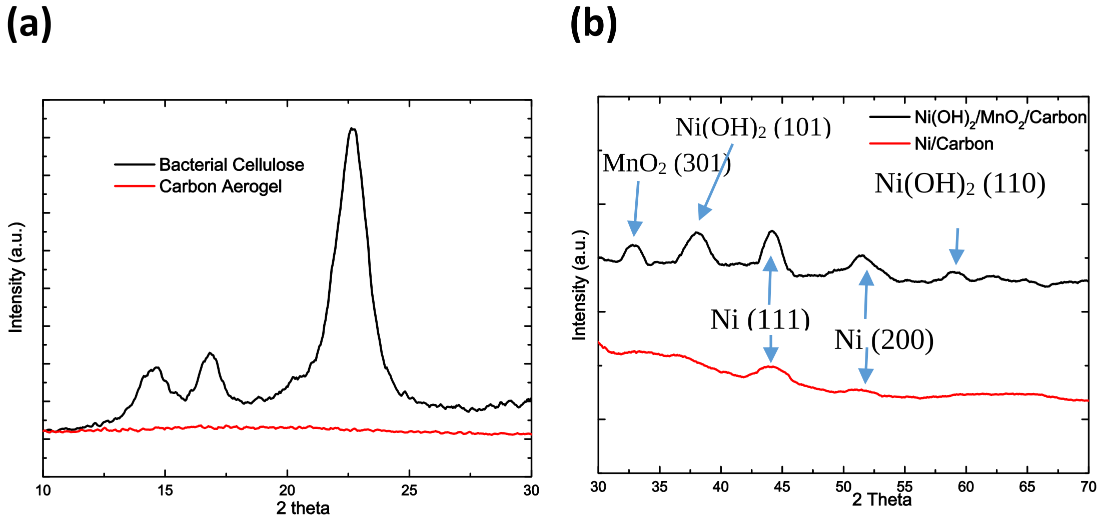

Figure 5.5. XRD pattern of (a) BC and CA. (b) CA after deposition of nickel particles and CA with the formation of $MnO_2/Ni(OH)_2$ hybrid.

The electrochemical performance of the CAs, CAs deposited with Ni nanoparticles, and the CAs coated with Ni, MnO_2, and $MnO_2/Ni(OH)_2$ hybrid was examined using the CV, CCD and EIS tests carried out in 1 M Na_2SO_4 aqueous electrolyte. The CAs and CAs with Ni nanoparticles show negligible capacitance (0.5~1 F/g) because of the lack of active materials with the capacitive behavior (Figure 5.6a). After introducing MnO_2 and $Ni(OH)_2$ to the CA surface, the electrochemical performance is greatly improved. The CV curves in Figure 5.6b show a quasi-rectangular shape, indicating a typical supercapacitive behavior with good rate performance. Although the pseudo-capacitive materials (i.e., MnO_2 and $Ni(OH)_2$) are present in the electrode, the lack of redox peaks on the CV curves demonstrates the fast and reversible redox reactions happened at a constant rate over the entire voltammetric cycles, which is a typical characteristic of MnO_2-based electrodes caused by the combination of various redox peaks between Mn^{3+} and Mn^{4+}.[48]

As for the CCD tests at different current densities (1~5 A/g), the curves exhibit an isosceles triangle shape with constant slopes, which indicate ideal capacitive behaviors and confirm the result from the CV tests (Figure 5.6b). The initial voltage drop at the beginning of discharge process is commonly referred to as the IR drop, which reflects the effect of intrinsic resistance caused by the insulating binder used for the fabrication of the electrodes. The unique 3D hierarchical porous structure of the CAs can greatly promote fast ionic motion and facilitate the access to the interior surfaces of the electrode, which explains the good supercapacitive behavior. The calculated specific capacitance at 1 A/g is 109 F/g. EIS was tested between 0.01 and 100 kHz with a sinusoidal excitation signal of 5 mV to further investigate the electrochemical performance. It can be seen from the Nyquist plot that the curve shows a straight line almost vertical to the real axis in the low frequency region (Figure 5.6d). The steep line with high gradient is the typical characteristic of an ideal capacitor. On the other end, the curve shows a small arc in the high frequency region, which is caused by the charge transfer resistance.[49] The value of the intercept on real axis is equivalent series resistance (ESR), which represents the combined resistance originating from ionic resistance of the electrolyte, the contact resistance between electrode material and current collector, and the intrinsic active material resistance.[50] The ESR in this case is around 7.5 Ω, which corresponds well with the IR drop of the CCD test. The energy density and power density is shown by the Ragone plot to evaluate the electrode's energy storage performance (Figure 5.6e). The plot shows that the BC-based carbon aerogel electrodes can achieve an energy density as high as 9.4 Wh/Kg while the power density can reach 4000 W/Kg. These high values show the application potential of the Ni/MnO_2/$Ni(OH)_2$ coated CAs in energy storage devices.

As a demonstration, three SCs, which used H_2SO_4/PVA gel as the electrolyte and Ni/MnO_2/$Ni(OH)_2$ coated CAs as the electrode material, were connected in series to make a power source. The device was charged to 3 volts and then connected to a LED light. As shown in Figure 5.6f, the device can light the LED for more than 2 minutes. This demonstration shows promising application of using carbon aerogel produced from bacterial cellulose as the scaffold and MnO_2/$Ni(OH)_2$ hybrid as active materials for the electrodes of energy storage devices.

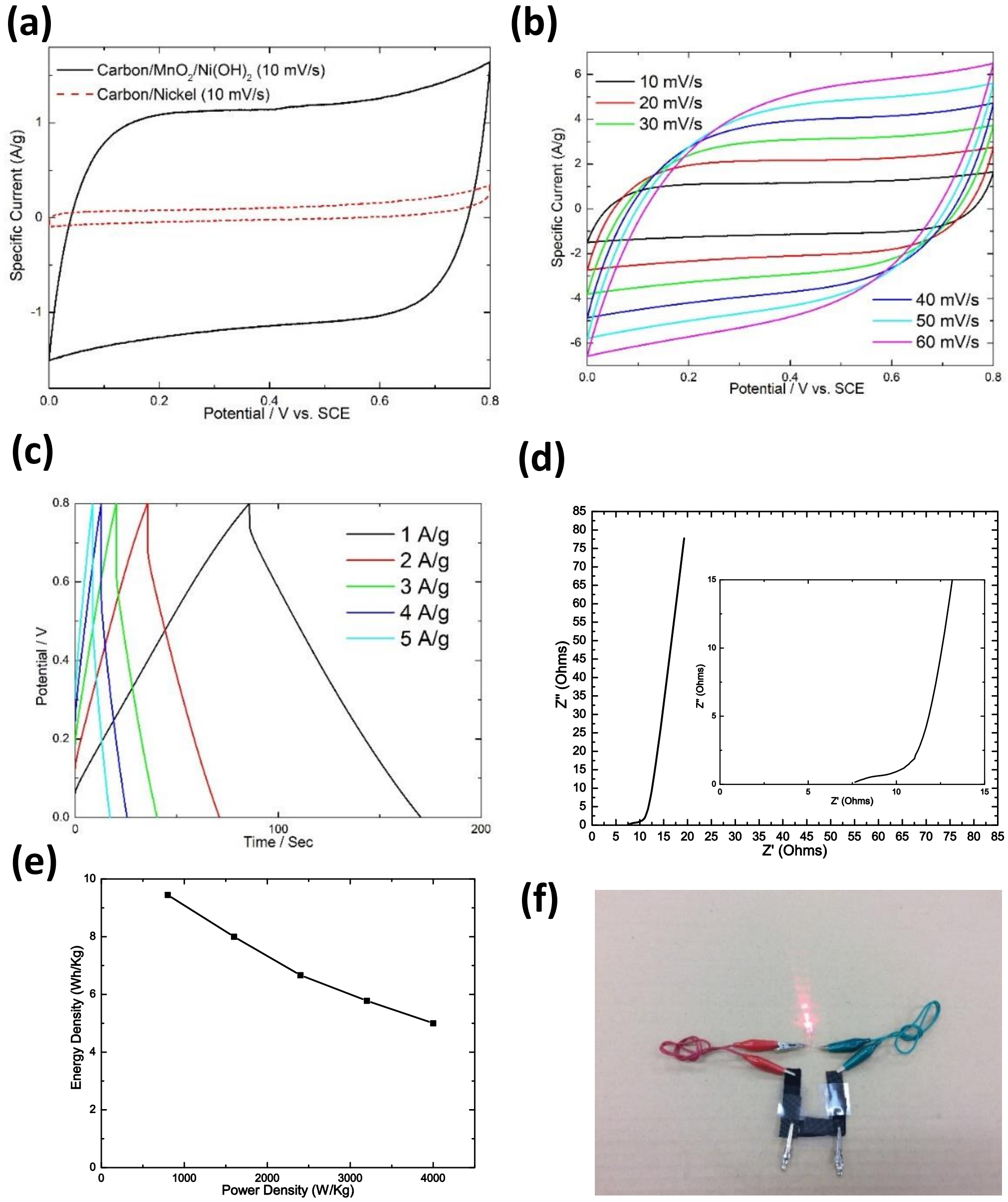

Figure 5.6. (a) Comparison of the CV curves of Ni coated CAs and Ni/MnO_2/$Ni(OH)_2$ coated CAs at 10 mV/s. (b) CV curves at various scan rates for the Ni/MnO_2/$Ni(OH)_2$ coated CAs. (c) Galvanostatic charge/discharge curves at different current densities. (d) Nyquist plot (e) Ragone plot. (f) LED light powered by supercapacitor pack.

5.4. Conclusion

In summary, we reported the preparation of freestanding carbon aerogel produced from bacterial cellulose. The aerogel was coated with nickel by electrodeposition, and then decorated with MnO_2 through a redox reaction. The electrochemical performance was examined by cyclic voltammetry, cyclic charge/discharge and electrochemical impedance spectroscopy. The results show that a high specific capacitance of 109 F/g can be achieved at 1 A/g, and the power density can reach 4000 W/Kg. This research offers a novel application method of bacterial cellulose in the field of power storage devices.

5.5. References

1. Siró, I.; Plackett, D. *Cellulose* **2010,** 17, (3), 459-494.
2. Haigler, C. H., *Biosynthesis and biodegradation of cellulose*. CRC Press: 1990.
3. Klemm, D.; Heublein, B.; Fink, H.-P.; Bohn, A. *Angewandte Chemie International Edition* **2005,** 44, (22), 3358-3393.
4. Hon, D. N.-S. *Cellulose* **1994,** 1, (1), 1-25.
5. Iguchi, M.; Yamanaka, S.; Budhiono, A. *Journal of Materials Science* **2000,** 35, (2), 261-270.
6. Zhu, H.; Luo, W.; Ciesielski, P. N.; Fang, Z.; Zhu, J. Y.; Henriksson, G.; Himmel, M. E.; Hu, L. *Chemical Reviews* **2016,** 116, (16), 9305-9374.
7. Yamanaka, S.; Watanabe, K.; Kitamura, N.; Iguchi, M.; Mitsuhashi, S.; Nishi, Y.; Uryu, M. *Journal of Materials Science* **1989,** 24, (9), 3141-3145.
8. Ul-Islam, M.; Khan, T.; Park, J. K. *Carbohydrate Polymers* **2012,** 88, (2), 596-603.
9. Helenius, G.; Bäckdahl, H.; Bodin, A.; Nannmark, U.; Gatenholm, P.; Risberg, B. *Journal of Biomedical Materials Research Part A* **2006,** 76A, (2), 431-438.
10. Liebner, F.; Haimer, E.; Wendland, M.; Neouze, M.-A.; Schlufter, K.; Miethe, P.; Heinze, T.; Potthast, A.; Rosenau, T. *Macromolecular Bioscience* **2010,** 10, (4), 349-352.

11. Almeida, I. F.; Pereira, T.; Silva, N. H. C. S.; Gomes, F. P.; Silvestre, A. J. D.; Freire, C. S. R.; Sousa Lobo, J. M.; Costa, P. C. *European Journal of Pharmaceutics and Biopharmaceutics* **2014,** 86, (3), 332-336.

12. Fu, L.; Zhang, J.; Yang, G. *Carbohydrate Polymers* **2013,** 92, (2), 1432-1442.

13. Chen, L.-F.; Huang, Z.-H.; Liang, H.-W.; Guan, Q.-F.; Yu, S.-H. *Advanced Materials* **2013,** 25, (34), 4746-4752.

14. Rull-Barrull, J.; d'Halluin, M.; Le Grognec, E.; Felpin, F.-X. *Chemical Communications* **2016,** 52, (12), 2525-2528.

15. Jang, I.; Song, S. *Lab on a Chip* **2015,** 15, (16), 3405-3412.

16. Legnani, C.; Vilani, C.; Calil, V. L.; Barud, H. S.; Quirino, W. G.; Achete, C. A.; Ribeiro, S. J. L.; Cremona, M. *Thin Solid Films* **2008,** 517, (3), 1016-1020.

17. Conway, B. E., *Electrochemical supercapacitors: scientific fundamentals and technological applications*. Springer Science & Business Media: 2013.

18. Simon, P.; Gogotsi, Y. *Nat Mater* **2008,** 7, (11), 845-854.

19. Wang, Y.; Zhou, J.; Jiang, L.; Ulven, C.; Lubineau, G.; Liu, G.; Xiao, J. *J Polym Environ* **2015,** 23, (4), 595-605.

20. Zhang, L. L.; Zhao, X. S. *Chemical Society Reviews* **2009,** 38, (9), 2520-2531.

21. Conway, B. E.; Birss, V.; Wojtowicz, J. *Journal of Power Sources* **1997,** 66, (1), 1-14.

22. Yu, N.; Yin, H.; Zhang, W.; Liu, Y.; Tang, Z.; Zhu, M.-Q. *Advanced Energy Materials* **2016,** 6, (2), n/a-n/a.

23. Wang, Y.; Jiang, L.; Wang, Y. *Electrochimica Acta* **2016,** 210, 190-198.

24. Pushparaj, V. L.; Shaijumon, M. M.; Kumar, A.; Murugesan, S.; Ci, L.; Vajtai, R.; Linhardt, R. J.; Nalamasu, O.; Ajayan, P. M. *Proceedings of the National Academy of Sciences* **2007,** 104, (34), 13574-13577.

25. Xu, J.; Zhu, L.; Bai, Z.; Liang, G.; Liu, L.; Fang, D.; Xu, W. *Organic Electronics* **2013,** 14, (12), 3331-3338.

26. Li, S.; Huang, D.; Zhang, B.; Xu, X.; Wang, M.; Yang, G.; Shen, Y. *Advanced Energy Materials* **2014,** 4, (10), n/a-n/a.

27. Liu, Y.; Zhou, J.; Tang, J.; Tang, W. *Chemistry of Materials* **2015,** 27, (20), 7034-7041.

28. Wang, F.; Kim, H.-J.; Park, S.; Kee, C.-D.; Kim, S.-J.; Oh, I.-K. *Composites Science and Technology* **2016,** 128, 33-40.

29. Wang, X.; Kong, D.; Zhang, Y.; Wang, B.; Li, X.; Qiu, T.; Song, Q.; Ning, J.; Song, Y.; Zhi, L. *Nanoscale* **2016,** 8, (17), 9146-9150.

30. Chen, P.; Xiao, T.-Y.; Qian, Y.-H.; Li, S.-S.; Yu, S.-H. *Advanced Materials* **2013,** 25, (23), 3192-3196.

31. Chen, L.-F.; Huang, Z.-H.; Liang, H.-W.; Yao, W.-T.; Yu, Z.-Y.; Yu, S.-H. *Energy & Environmental Science* **2013,** 6, (11), 3331-3338.

32. Wang, S.; Guo, X.; Liang, T.; Zhou, Y.; Luo, Z. *Bioresource Technology* **2012,** 104, 722-728.

33. Collard, F.-X.; Blin, J. *Renewable and Sustainable Energy Reviews* **2014,** 38, 594-608.

34. Neves, D.; Thunman, H.; Matos, A.; Tarelho, L.; Gómez-Barea, A. *Progress in Energy and Combustion Science* **2011,** 37, (5), 611-630.

35. Gregg, S.; Jacobs, J. *Transactions of the Faraday Society* **1948,** 44, 574-588.

36. Sun, Y.; Gao, B.; Yao, Y.; Fang, J.; Zhang, M.; Zhou, Y.; Chen, H.; Yang, L. *Chemical Engineering Journal* **2014,** 240, 574-578.

37. Angın, D. *Bioresource Technology* **2013,** 128, 593-597.

38. Fan, Z.; Yan, J.; Wei, T.; Zhi, L.; Ning, G.; Li, T.; Wei, F. *Advanced Functional Materials* **2011,** 21, (12), 2366-2375.

39. Ren, Z.; Li, J.; Ren, Y.; Wang, S.; Qiu, Y.; Yu, J. *Scientific reports* **2016,** 6.

40. Jin, X.; Zhou, W.; Zhang, S.; Chen, G. Z. *Small* **2007,** 3, (9), 1513-1517.

41. Kang, Y. J.; Chun, S.-J.; Lee, S.-S.; Kim, B.-Y.; Kim, J. H.; Chung, H.; Lee, S.-Y.; Kim, W. *ACS Nano* **2012,** 6, (7), 6400-6406.

42. Ishikawa, A.; Okano, T.; Sugiyama, J. *Polymer* **1997,** 38, (2), 463-468.

43. Segal, L.; Creely, J.; Martin, A.; Conrad, C. *Textile Research Journal* **1959,** 29, (10), 786-794.

44. Zhai, Y.; Dou, Y.; Zhao, D.; Fulvio, P. F.; Mayes, R. T.; Dai, S. *Advanced Materials* **2011,** 23, (42), 4828-4850.

45. Ni, J.; Huang, Y.; Gao, L. *Journal of Power Sources* **2013,** 223, 306-311.

46. Wu, S.-H.; Chen, D.-H. *Journal of Colloid and Interface Science* **2003,** 259, (2), 282-286.

47. Patil, U. M.; Gurav, K. V.; Fulari, V. J.; Lokhande, C. D.; Joo, O. S. *Journal of Power Sources* **2009,** 188, (1), 338-342.

48. Zhi, J.; Reiser, O.; Huang, F. *ACS Applied Materials & Interfaces* **2016,** 8, (13), 8452-8459.

49. Xu, X.; Liu, Y.; Wang, M.; Zhu, C.; Lu, T.; Zhao, R.; Pan, L. *Electrochimica Acta* **2016,** 193, 88-95.

50. Lei, W.; Han, L.; Xuan, C.; Lin, R.; Liu, H.; Xin, H. L.; Wang, D. *Electrochimica Acta* **2016,** 210, 130-137.

6. SUMMARY AND FUTURE WORK

6.1. Summary

In this dissertation, the preparation of carbon-based nanomaterials from agricultural residues and agricultural by-products is explored. Many advanced applications are investigated, especially in the field of electrode materials for energy storage devices. The development of porous activate carbons were investigated in detail, and their applications as electrode materials of supercapacitors were demonstrated. Besides the traditional carbonization and chemical activation at high temperature (~1000℃), the hydrothermal carbonization of biomass to produce carbonaceous materials at relatively low temperature (~200℃) was also covered in this dissertation. This dissertation proves that the microwave irradiation can be an effective way to increase the crystallinity of porous activated carbons, thus reduce the electrical resistance of the electrodes. In addition to the traditional raw materials such as cellulose produced from wood industry, novel material sources such as bacterial cellulose were used to prepare nanocomposites that can be used for high-performance electrodes of supercapacitors as well. Overall, this dissertation contributes to the sustainable development of the agricultural industry in North Dakota.

In the first research of this dissertation discussed in chapter 2, a one-step facile method to produce 3D porous ACs from DDGS using by microwave-assisted chemical activation was developed. The surface area of the obtained ACs varied from several hundreds to the maximum of nearly 1036 m^2/g, depending on the acid ratio and the activation temperature. Pore size analysis based on nitrogen adsorption/desorption tests found that the ACs contained large fraction of micropores. The MB adsorption tests showed that the adsorption capacity of the ACs was proportional to their surface areas, with the highest being 477 mg/g for the 1036 m^2/g surface area.

The EDLCs based on the DDGS-based ACs exhibited excellent electrochemical performance and stability. The specific capacitances ranging from 120 to 210 F/g were achieved and the electrode showed minimal degradation after 1000 charge/discharge cycles. The specific capacitance can be further improved up to nearly 300 F/g by forming AC/MnO_2 composite with pseudocapacitance behavior. The research pointed out that the adsorption and electrochemical test results indicated that the adsorption capacity was determined by the total surface area of the ACs, while the capacitance was critically controlled by both the surface area and the pore size distribution. This study demonstrated the potentials of DDGS in environmental remediation and energy storage applications.

Based on the results of the first research, a facile GO-assisted HTC and microwave irradiation process was developed in chapter 3 to convert DDGS into supercapacitor-ready ACs. Instead of the direct chemical activation method used in the first research in chapter 2, a novel HTC method was used to carbonize the biomass, and biochar was formed after the HTC treatment. The results show that GO plays an important role in increasing the electrochemical properties of the produced AC. The addition of GO changed the shape of the hydrochar particles from spheres to flakes by serving as a carbonization template. Additionally, GO absorbed microwave irradiation to create high temperature for carbonization and graphitization. The final microwave irradiation was proved to be a highly effective method to rapidly increase the degree of carbonization and graphitization of the hydrochar. This study shows that direct carbonization of wet DDGS (or other biomass) using HTC followed by microwave irradiation represents a highly energy-efficient method to produce high value carbon materials. However, despite the low-cost and facile carbonization brought by the hydrothermal treatment, it should be noted that when using the HTC method, the solution inside the autoclave is in subcritical state with high pressure and high temperature. The experiment has the potential of dangerous explosion and should be carried out in safe place with protection.

In addition to the research on DDGS as the raw material for the preparation of carbon-based nanomaterials, a novel material, bacterial cellulose, was also investigated for the production of freestanding carbon aerogel. The aerogel was coated with nickel by electrodeposition, and then decorated with MnO_2 through a redox reaction. As a foundation of this research, the electrodeposition technique was explored in chapter 4 by using natural carbon nanoparticles generated from combustion as nucleus for the formation of 3D interconnected network. Both PANI and MnO_2 were chosen as the active materials for the electrodes of SCs. The CNPs/PANI electrodes showed a high specific capacitance of 140 F/g at the current density of 1 A/g, but the value decreased markedly at high scan rates and high current densities. On the other hand, although the capacitance of CNPs/MnO_2 electrodes were lower than that of CNPs/PANI, its deterioration with increasing scan rate and current density was much more limited. Both electrodes can find suitable applications in flexible supercapacitors according to their distinctive advantages and disadvantages.

Finally, by using the freestanding carbon aerogel produced from bacterial cellulose as the scaffold, nickel nanoparticles were deposited on the carbon aerogel using the electrodeposition technique introduced in chapter 4, and then the CA was decorated with MnO_2 through a redox reaction. The electrochemical performance was fully examined by cyclic voltammetry, cyclic charge/discharge and electrochemical impedance spectroscopy in chapter 5. The results show that a high specific capacitance of 109 F/g can be achieved at 1 A/g, and the power density can reach 4000 W/Kg. This research offers a novel application method of bacterial cellulose in the field of power storage devices. The comparison of the electrode materials is shown in Table 6.1.

Table 6.1. Comparison of the electrode materials developed in this dissertation

Raw materials	**Type of Supercapacitor**	**Preparation method**	**Capacitance at 1A/g (F/g)**
DDGS	EDLCs	Carbonization/Activation	195
DDGS/MnO_2	Pseudocapacitor	Carbonization/Activation, Redox reaction	286
DDGS/GO	EDLCs	HTC, Activation, Microwave irradiation	102
CNPs/MnO_2	Pseudocapacitor	Electrodeposition	99
CNPs/PANI	Pseudocapacitor	Electrodeposition	140
BC/$Ni(OH)_2$/MnO_2	Pseudocapacitor	Electrodeposition, Redox reaction	109

6.2. Future work

From the discussion of the four projects in chapter 2~5, it can be concluded that agricultural residues can be used as low-cost and renewable sources for advanced carbon-based materials. In this dissertation, the pyrolysis of biomass is investigated in detail by thermal decomposition of biomass in absence of oxygen. After pyrolysis, solid biochar was produced and porous carbon can be produced by further activation. A novel HTC method was also investigated for carbonization of biomass at relatively low temperature. Bacterial cellulose can also be used as another raw material to produce carbon aerogels with 3D interconnected network, but the cost for the production of bacterial cellulose is still relatively high. In the further work, the hydrolysis of biomass to produce bacterial cellulose can be a possible way to fully utilize agricultural residuals. By hydrolysis of agricultural residuals, nutrients necessary for the growth of bacterial cellulose can be provided at lower cost. The enzymatic hydrolysis of biomass will be the future work in order to achieve better use of agricultural residues such as DDGS. Besides, microwave irradiation has been proven to be an effective way for the carbonization of biomass in this dissertation.

Microwave irradiation can be used to efficiently carbonize biomass and produce porous activated carbons. Compared with traditional thermal carbonization, it has many advantages such as fast heating rate and high efficiency. This dissertation points out that graphene oxide can absorb microwave irradiation to create high temperature for carbonization and graphitization of biomass, which favors the increase of the electrochemical performance of the electrodes. Future work on the treatment of biomass by microwave irradiation can be a method of great potential for efficient utilization of agricultural residuals.

APPENDIX. LIST OF PUBLICATIONS

1. Wang, Y.; Zhou, J.; Jiang, L.; Ulven, C.; Lubineau, G.; Liu, G.; Xiao, J., Development of Low-Cost DDGS-Based Activated Carbons and Their Applications in Environmental Remediation and High-Performance Electrodes for Supercapacitors. J Polym Environ 2015, 23 (4), 595-605.

2. Wang, Y.; Jiang, L.; Wang, Y., Development of Candle Soot Based Carbon Nanoparticles (CNPs)/Polyaniline Electrode and Its Comparative Study with CNPs/MnO2 in Supercapacitors. Electrochimica Acta 2016, 210, 190-198.

3. Wang, Y.; Jiang, L., Roles of Graphene Oxide in Hydrothermal Carbonization and Microwave Irradiation of Distiller's Dried Grains with Solubles To Produce Supercapacitor Electrodes. ACS Sustainable Chemistry & Engineering 2017, 5 (6), 5588-5597.

4. Wang, Y.; Jiang, L., Freestanding Carbon Aerogel Produced from Bacterial Cellulose and its Application as Scaffold of MnO_2/$Ni(OH)_2$ hybrid for High-performance Supercapacitor Electrodes. Under review.

5. Wang, Y.; Jiang, L., Direct Microwave Carbonization of Bacterial Cellulose Aerogels and Their Application for Electrodes of Supercapacitors. In preparation.